Image-Guided Targeting and Control of Implantable Electrodes

By

Louis Beryl Kratchman

Dissertation

Submitted to the Faculty of the

Graduate School of Vanderbilt University

partial fulfillment of the requirements

for the degree of

DOCTOR OF PHILOSOPHY

in

Mechanical Engineering

May, 2015

Nashville, Tennessee

Approved:

Robert J. Webster, III

Nabil Simaan

Pietro Valdastri

J. Michael Fitzpatrick

Robert F. Labadie

To my wife Clare, Max, and Zack

ACKNOWLEDGMENTS

I thank my adviser, Bob Webster, for his encouragement over the years, his openness to new ideas, and for widening my perspective about our work. He has challenged me to make the maximum impact, in research and beyond.

I am indebted to Robert Labadie and Michael Fitzpatrick for welcoming me into the CAOS Lab, guiding my research, serving on my thesis committee, and for their enthusiasm and humor. The creativity and teamwork I've experienced in the CAOS Lab has left a deep impression on me. I could not have completed the work in this thesis without the contributions from past and present CAOS Lab members Ramya Balachandran, Grégoire Blachon, Maria Ashby, Lueder Kahrs, Wendy Lipscomb, and Kate Von Wahlde. Thank you all for sharing your talents and energy.

Outside of the lab, I've relied on the steadfast support of my wife, and the love and counsel of my parents.

My sincere thanks to committee members Nabil Simaan and Pietro Valdastri for their time, comments, and attention to this manuscript.

To all the graduate students, postdocs, and undergraduates in the MED Lab whom I have worked with, thank you for making my time at Vanderbilt pleasurable. I would especially like to thank undergraduates Mish Rahman, Justin Saunders, and Yifan Zhu for their help and commitment to various projects.

I would also like to thank Brent Gillespie and Johann Borenstein at the University of Michigan, who helped interest me in research.

I owe thanks to several others who made special contributions to this dissertation. Tom Withrow was instrumental in bringing Chapter 2 to fruition. John Fitzpatrick at FHC Corporation graciously provided the data discussed in the Appendix to Chapter 3. My chapter 4 co-author Daniel Schuster was a great partner in experiments. Neil Dillon helped us set up experimental equipment for Chapter 5, and Hunter Gilbert and Richard Hendrick shared valuable insights on the theory of elastic rods.

ABSTRACT

Implantable electrodes are used to diagnose and treat a growing list of conditions, including deafness, chronic pain, and neurodegenerative disorders. This dissertation introduces robotic methods to make electrode implantation less invasive, safer, and easier for clinicians to perform. We focus on implantation through a narrow hole under image guidance, and contribute methods to both guide instruments along a straight insertion path and to steer electrodes that are inserted through such a hole.

We present the first bone-attached robot to accurately guide instruments to the cochlea. This system removes the need to fabricate a stereotactic guide in the operating room and reduces dependence on a surgeon's skill. Results from a phantom targeting experiment show this system to be sufficiently accurate for cochlear implantation surgery. Manually adjusted stereotactic frames are used to implant deep brain stimulation (DBS) electrodes, but encumber the patient and are prone to operator errors. Smaller targeting devices are available for DBS surgery, but require offsite manufacturing or expensive image guidance systems. We introduce robotically adjusted, disposable microstereotactic frames that are rapidly adjusted, locked, and then transferred to a patient in a single visit. A phantom validation experiment shows that the targeting error of a robotically adjusted frame was below the clinically accepted threshold.

Sensitive tissues can be damaged by the force of electrode implantation. Robotic insertion devices have the potential to detect and react to excessive insertion forces, but the relationship between forces and trauma is poorly understood. Presently, we rely on surgeons to judge when forces are too large, but the ability of surgeons to sense small forces when

implanting electrodes has not been studied. We introduce a method to measure intraocochlear puncture forces and report the first force measurements obtained from fresh cadaveric specimens. To put these forces into a clinical perspective, we present a protocol to measure tactile thresholds in a model of CI surgery, and present the first experimental characterization of surgeons' tactile force thresholds.

An electrode can be actively steered to reduce trauma and avoid obstacles. We present the first method to guide a magnet-tipped electrode along arbitrary three-dimensional trajectories using a compact, robot-manipulated magnet located external to the patient. We model rod deflections by combining Kirchhoff rod theory with permanent magnet models, and compute trajectories using a resolved-rate approach. Experiments demonstrate accurate execution of three-dimensional tip trajectories in an open-loop configuration and obstacle avoidance.

This dissertation provides a complementary set of methods for improving electrode implantation. These methods could benefit both patients and clinicians who perform minimally invasive procedures.

CONTENTS

LIST OF FIGURES

LIST OF TABLES

CHAPTER 1

INTRODUCTION

Cochlear implants have been described as the most successful neural prostheses [1]. Without these devices, over 300,000 recipients worldwide would be unable to hear. In the United States, approximately 1.5 million people are considered eligible for the surgery [2], but have not received the treatment for a variety of reasons. Can cochlear implants be made more accessible to those suffering from severe hearing loss? Can the success of cochlear implants be replicated or surpassed by emerging treatments that also use implantable electrodes, such as deep brain stimulation and other neuromodulation therapies? The answers to these questions will depend in part on the tools and techniques available for electrode implantation. This thesis proposes methods to improve the safety, invasiveness, and clinical practicability of electrode implantation. For background to the next two chapters, which introduce new stereotactic devices for electrode implantation, the remainder of this chapter reviews stereotactic targeting devices which preceded our work.

1.1 Stereotactic Frames

Stereotactic surgery uses an apparatus to guide an instrument to a target within the head or other area of the body where anatomical structures have a rigid spatial arrangement, such as the spine. The instrument is guided using a three-dimensional representation of the patient's anatomy, which may be a surgical atlas or a medical image. The traditional instrument for stereotactic surgery is the stereotactic frame, though several other devices are used clinically and will be discussed in this chapter.

The stereotactic frame was introduced by Horsley and Clarke in 1908 [3]. Previous devices were constructed to identify particular regions of the brain or the cortex with respect to landmarks

on the skull, but Horsley and Clarke built the first device able to probe the entire three-dimensional volume of an animal brain [4], and to relate coordinates to a brain atlas. They built several models, none of which were used on humans. The first human stereotactic neurosurgery was performed by Ernest Spiegel and Henry Wycis in 1947, who identified brain landmarks in x-ray images to guide a probe, sparking worldwide interest in stereotactic surgery and development of new stereotactic frames [5].

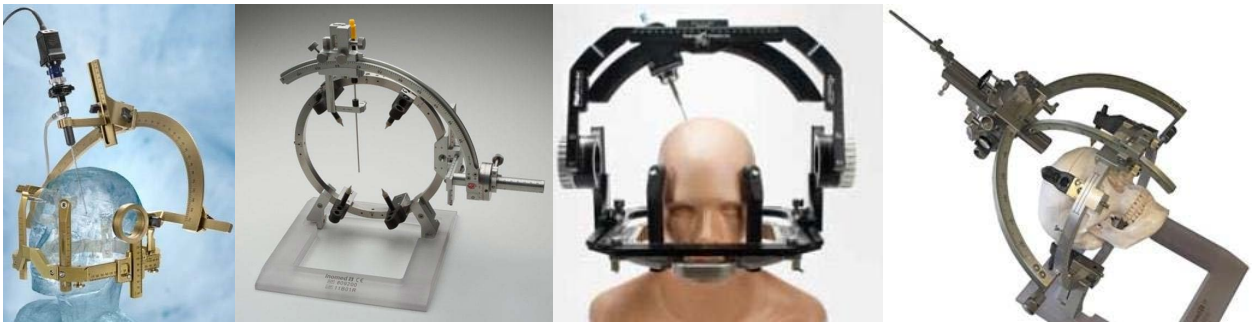

(a) (b) (c) (d)

Figure 1.1: Stereotactic frames in current use include the (a) Leksell frame, shown with attached endoscope[1] (b) Zamorano-Dujovny[2] frame (c) Cosman-Roberts-Wells frame [3] (d) and Riechert-Mundinger frame[4].

Several stereotactic frames in current clinical use are shown in Figure 1.1. Prior to surgery, a base ring is attached to a patient by tightening four or more sharpened pins into the scalp. The base ring establishes a coordinate system in rigid relation to patient anatomy. A localizer device that encloses the patient's head is attached to the base ring for acquisition of pre-operative images. Localizers are available for computed tomography (CT), magnetic resonance imaging (MRI), and angiographic imaging. The localizer contains fiducial markers that enable registration of surgical targets to the stereotactic coordinate system. Fiducial localization and selection of target and entry points is usually performed with stereotactic planning software. To perform the surgery, the localizer is replaced by a mechanical apparatus that is

[1]Image: Elekta AB, www.elekta.com, accessed March 3, 2015.
[2]Image: inomed Medizintechnik GmbH, www.inomed.com, accessed March 3, 2015.
[3]Image: Integra LifeSciences, www.integralife.com, accessed March 3, 2015.
[4]Image: inomed Medizintechnik GmbH, www.inomed.com, accessed March 3, 2015.

manually adjusted to guide an instrument such as an electrode advancer, endoscope, or cannula to the target. Coordinate settings are calculated with the aid of the planning software and transferred to several adjustable components with engraved markings on the frame. Frames such as the Cosman-Roberts-Wells (CRW) and Riechert-Mundinger (RM) have a separate base that can position a phantom target to check the accuracy of an adjusted frame before it is used in surgery.

Stereotactic frames are the conventional apparatus for stereotactic neurosurgeries, and are indicated for a wide range of procedures, including functional neurosurgical procedures, such as electrode placement for deep brain stimulation surgery or treatment of intractable pain, and non-functional procedures such as biopsy ablation, cyst drainage, and hematoma evacuation [6, 7]. Clinicians are experienced at using stereotactic frames, and a large body of published studies documents the clinical use of these devices [5]. Current frames can reach targets throughout the brain volume and can be repositioned during surgery. The mechanical designs of these devices have been refined over several decades, resulting in durable instruments that perform reliably after many surgeries.

However, traditional stereotactic frames have several drawbacks which have motivated development of the alternative approaches to be discussed shortly. The heavy, cage-like structure of these devices causes anxiety in many patients who are required to remain conscious during certain neurosurgical procedures, and may suffer from movement disorders that further increase discomfort. For clinicians, assembly of a frame from its sterilization tray components is a tedious, time-consuming process, as is the process of securing the frame to the patient using fixation pins. During surgery, frames may obstruct access to the patient. Accurate frame adjustment requires repeated transfer of coordinates from planning software to adjustable scales at several locations on a frame. Flickinger et al. [8] examined 200 clinical cases of stereotactic frame adjustment for radiosurgery and found coordinate errors in 12 percent of the cases. The authors found that two additional observers were required to check coordinates in order to

reduce the error rate to an acceptable level.

1.1.1 Frameless Stereotactic Systems

Frameless stereotactic systems allow surgeons to visualize the location of a tool with respect to patient anatomy in real time. Current systems use optical or electromagnetic tracking systems to sense the relative locations of the patient and tools. Navigation software is used to display preoperative images, planning data, and digital atlas data along with the tracked tools on a monitor or surgical microsope.

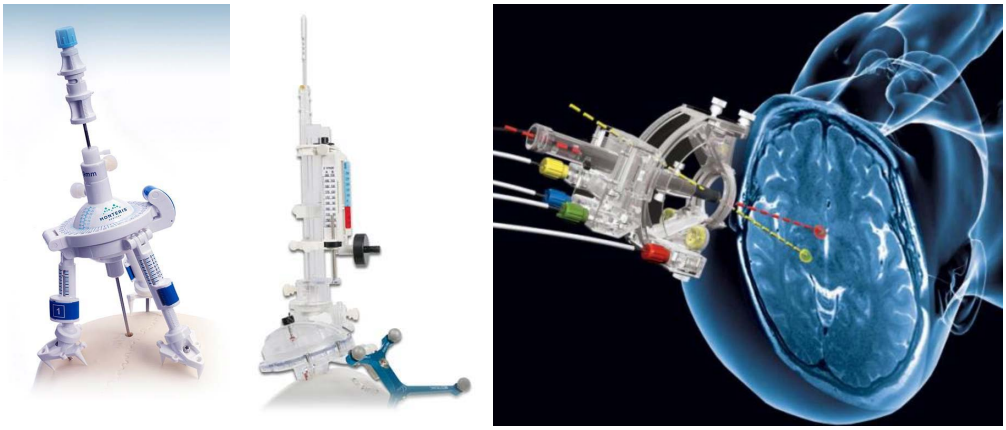

(a) (b) (c)

Figure 1.2: Bone-attached, stereotactic tool guides that are aimed at a neurosurgical target using a separate image guidance system or MRI scanner include (a) the AxiiiS Miniframe[1], (b) the NexFrame[2], and (c) the ClearPoint system[3], which uses real-time MRI imaging to adjust the attached trageting device.

Frameless stereotactic systems that are based on optical tracking use an infrared, stereoscopic camera system to find the positions of either passive (retro-reflective) or active (light-emitting) markers. Currently used systems include NavSuite (Stryker Corporation, Kalamazoo, MI, USA), VectorVision (BrainLab AG, Feldkirchen, Germany), and StealthStation (Medtronic, Inc., Fridley, MN, USA). To determine the orientation of an object, three or more fiducial markers are attached to a rigid object,

[1]Image: Monteris Medical, www.monteris.com, accessed March 3, 2015.
[2]Image: Medtronic plc, www.medtronic.com, accessed March 3, 2015.
[3]Image: MRI Interventions, www.mriinterventions.com, accessed March 3, 2015.

such as a patient's head or a rigid tracking frame attached to a tool, and the orientation of the object is determined from the relative positions of a set of markers. Optical tracking systems require a line of site to be maintained between the tracker camera and the tracked object.

Electromagnetic tracking systems, such as the Cygnus Stereotactic System (Compass International, Inc., Rochester, MN, USA), StealthStation AxiEM (Medtronic Inc.), and InstaTrak (GE Healthcare), use a field generator project a magnetic field through the operative region. Induced currents in a small coil embedded in an instrument are measured to determine the instrument's location. The coil can be embedded near the tip of the instrument because a line of sight is not required to track the coil. Metallic objects in the operating suite can distort the field, so precautions are required to maintain accuracy.

Several types of instrument guides are used for applications where a freehand approach to guiding a tracked instrument does not provide sufficient accuracy or stability. These devices are positioned using an image guidance system and then locked, and include articulated positioning arms, burrhole-mounted devices, and bone-attached devices [9]. Bone-attached devices are anchored at several points around the entry hole, and include The NexFrame system (Medtronic, Inc.), Axiiis Stereotactic Miniframe (Monteris Medical Corp., Plymouth, MN, USA), and the ClearPoint system (MRI Interventions, Irvine, CA, USA), which are shown in Figure 1.2. The ClearPoint system processes MRI images in real-time, and guides a surgeon to adjust control knobs on the frame to align the device with a planned trajectory.

Frameless systems have been increasingly used for procedures such as brain biopsy and brain tumor removal [10]. However, these systems rely on expensive image guidance systems and surgeon hand-eye coordination for accurate adjustment.

1.1.2 Robotic Stereotactic Surgery

In 1985 Kwoh et al. used an industrial robot to biopsy a brain tumor, the first published report of a robot used in human surgery and a precursor to later robotic stereotactic systems [11, 12]. The base ring from a stereotactic frame was attached to a patient's scalp, and a CT scan was used to localize the tumor with respect to a localizer frame attached to the base ring. The system was eventually retired after twelve successful surgeries [13]. A number robotic systems for stereotactic and general neurosurgical tasks were constructed following Kwoh et al. [13, 14]. Three FDA-approved, commercial systems in current clinical use are shown in Figure 1.3. These include the Neuromate (Renishaw plc, Wotton-under-Edge, United Kingdom), Rosa (MedTech S.A.S, Castelnau Le Lez, France), and Renaissance (Mazor Robotics Ltd., Caesarea, Israel) systems.

(a) (b) (c)

Figure 1.3: Clinically-approved stereotactic robots include the (a) The NeuroMate[1] (b) Rosa[2] (c) Renaissance systems[3].

As with other stereotactic devices, a stereotactic robot must be registered to pre-operative images for accurate targeting. A patient's head may be immobilized by rigid pins and rigidly connected

[1]Image: Renishaw plc, www.renishaw.com, accessed March 3, 2015.
[2]Image: Medtech SAS, www.medtech.fr, accessed March 3, 2015.
[3]Image: Mazor Robotics, www.mazorrobotics.com, accessed March 3, 2015.

to the robot base, or an image guidance system may be used in a frameless approach. Both the Neuromate and Rosa systems can be used with a frameless approach. The miniature parallel robot of the Mazor Renaissance system [15] is attached directly to bone, which eliminates relative motion between the robot base and the patient without immobilizing the robot or the patient's body. The primary surgical application of the system is pedicle screw placement in the spine, but may also be used in neurosurgery, and has recently been approved by the Food and Drug Administration (FDA) for deep-brain stimulation surgery [14].

Robotic stereotactic systems may be advantageous for procedures that require frequent repositioning of tools, such as neuroendoscopy and stereoelectroencephalography (SEEG). Though robots are not susceptible to the cognitive errors that human clinicians may be susceptible to when adjusting a stereotactic device, there is always a risk of mechanical or electrical malfunction with such devices.

1.1.3 Custom-manufactured stereotactic frames

The STarFix microTargeting Platform (FHC Inc., Bowdoin, ME, USA) is an FDA-approved system for implantation of electrodes for deep brain stimulation, and requires no manual adjustments [16]. Rather, each STarFix is custom-manufactured using patient-specific data to be pre-aimed at a target. Prior to surgery, three or four titanium anchors are implanted on a patient's scalp followed by CT and MR image acquisition. The patient then leaves the surgical site with the anchors in place. Planning software is used to register the CT scan to the MR scan, localize the anchors in the CT image, and select a target in the MR image. The planning data is transmitted to a special site where the STarFix is manufactured using a three-dimensional printing process, and then is delivered to the surgical site after approximately three days. During surgery, the STarFix is bolted to the pre-implanted anchors, and supports an electrode driver. The STarFix is a compact, light weight fixture that eliminates the need for manual frame adjustment, but the time delay required for manufacturing the device is an inconvenience

for patients.

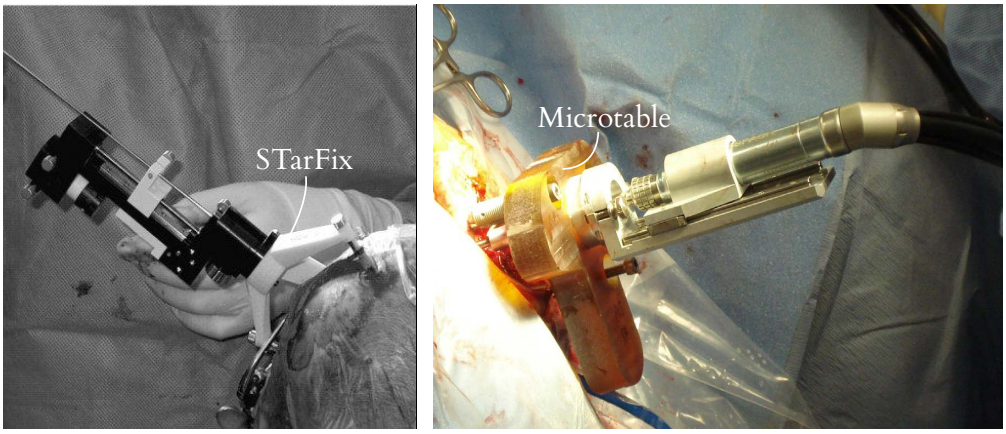

(a) (b)

Figure 1.4: Custom-manufactured stereotactic devices. (a) The STarFix platform[1] is manufactured using three dimensional laser sintering technology at a special facility and used for electrode implantation during deep-brain stimulation surgery. (b) The Microtable is manufactured at the surgical site using a computer numerical control (CNC) milling machine, and is used to a guide a drill and other instruments for cochlear implantation surgery.

Labadie et al. developed a customized, miniature stereotactic frame that can be manufactured at the operating site in less than five minutes using a portable Computer Numerical Control (CNC) milling machine. This frame, termed a Microtable, serves as a drill and instrument guide for minimally-invasive cochlear implantation surgery. The Microtable is currently under undergoing clinical trials. We will discuss the Microtable in Chapter 2.

Custom-manufactured frames eliminate the tedious process of manually adjusting a traditional stereotactic frame or of adjusting a frameless system with the aid of an expensive image guidance system. They are small, and do not obstruct the operative field or restrict patient movement. They do not require a large investment in a stereotactic robot or image guidance systems. However, the current paradigms for preparing customized frames are additive manufacturing (three dimensional printing) and subtractive manufacturing (milling), which impose time delays and other surgical workflow inconviences

[1] Image: FHC Corporation, www.fh-co.com, accessed March 3, 2015.

for clinicians.

The stereotactic systems reviewed in this chapter provide sufficient accuracies for their intended applications [9, 17–22], but new applications, such as minimally-invasive cochlear implantation, require submillimetric accuracy which has not been demonstrated for most of these systems. With growth of neurostimulation therapies that require electrode implantation, improvements to the comfort, cost, and convenience (for both patients and surgeons) of surgery would help widen the the availbility of these treatments.

1.1.4 Contributions

This thesis presents contributions to several aspects of minimally invasive electrode implantation. In the next two chapters, we describe robotic paradigms for adjusting stereotactic devices that offer several improvements over the stereotactic systems reviewed above. In Chapter 2, we present the first bone-attached robot to accurately guide instruments to the cochlea through a minimally invasive drill hole. This approach removes the need to fabricate a stereotactic guide in the operating room and reduces dependence on a surgeon's skill. The manuscript of this chapter was published as a journal article in the *IEEE Transactions on Biomedical Engineering* [23]. In Chapter 3, we introduce robotically adjusted, disposable microstereotactic frames for deep brain stimulation surgery. These frames offer more comfort than traditional stereotactic frames and have the potential to be prepared faster, at lower expense, and with better targeting flexibility than comparable systems. We are the first to describe adjustment of a passive stereotactic device by a robot, and our concept may be extended to new stereotactic applications. This chapter was presented at SPIE Medical Imaging conference in February, 2012 [24].

An electrode must be placed in contact with tissue to properly transmit signals, but there is a risk of damaging the delicate tissues when advancing the electrode. Robotic insertion devices have the potential to detect and avoid excessive insertion forces, but the relationship between forces and trauma is

poorly understood. Presently surgeons alone decide when forces are too large, but the ability of surgeons to sense small forces when implanting electrodes has not been studied. In Chapter 4, we contribute the first measurements of intracochlear puncture forces, obtained from fresh cadaveric specimens. To establish a broad context for interpreting insertion forces, we present a protocol to measure tactile thresholds in a model of CI surgery, and present the first experimental characterization of surgeons' tactile force thresholds. Our tactile threshold measurement technique is generalizable to many other surgical tasks where tactile sensitivity is important. The work in this chapter on intracochlear forces has been accepted for publication in *Otology & Neurotology*.

It is often desirable to steer the tip of an electrode or other rod-like device. In Chapter 5, we present the first method to guide a magnet-tipped electrode along arbitrary three-dimensional trajectories using a compact, robot-manipulated magnet, located external to the patient. We model rod deflections by combining Kirchhoff rod theory with permanent magnet models, and compute trajectories using a resolved-rate approach. Experiments demonstrate accurate execution of three-dimensional tip trajectories in an open-loop configuration. Our technique is immediately applicable to any surgical application where thin, steerable rods would be useful. The manuscript of this chapter been submitted as a journal article to *IEEE Transactions on Robotics*.

CHAPTER 2

DESIGN OF A BONE-ATTACHED PARALLEL ROBOT FOR PERCUTANEOUS COCHLEAR IMPLANTATION

Access to the cochlea requires drilling in close proximity to bone-embedded nerves, blood vessels, and other structures, the violation of which can result in complications for the patient. It has recently been shown that microstereotactic frames can enable an image-guided percutaneous approach, removing reliance on human experience and hand-eye coordination, and reducing trauma. However, constructing current microstereotactic frames disrupts the clinical workflow, requiring multiday intrasurgical manufacturing delays, or an on-call machine shop in or near the hospital. In this chapter, we describe a new kind of microsterotactic frame that obviates these delay and infrastructure issues by being repositionable. Inspired by the prior success of bone-attached parallel robots in knee and spinal procedures, we present an automated image-guided microstereotactic frame. Experiments demonstrate a mean drill bit accuracy at the cochlea of $0.20 \pm 0.07\,\mathrm{mm}$ in phantom testing with trajectories taken from a human clinical dataset. We also describe a cadaver experiment evaluating the entire image-guided surgery pipeline, where we achieved an accuracy of $0.38\,\mathrm{mm}$ at the cochlea. The manuscript of this chapter was published in the *IEEE Transactions on Biomedical Engineering* [23].

2.1 Introduction

Cochlear implants are electronic devices that can restore hearing to individuals who have severe or total hearing loss. In a cochlear implant system, shown in Figure 2.1, an external microphone and sound/speech processing unit transmit signals through the skin to a subcutaneous receiver, which applies electrical impulses to an electrode array implanted inside the cochlea. This array stimulates intracochlear

nerves, resulting in sound perception.

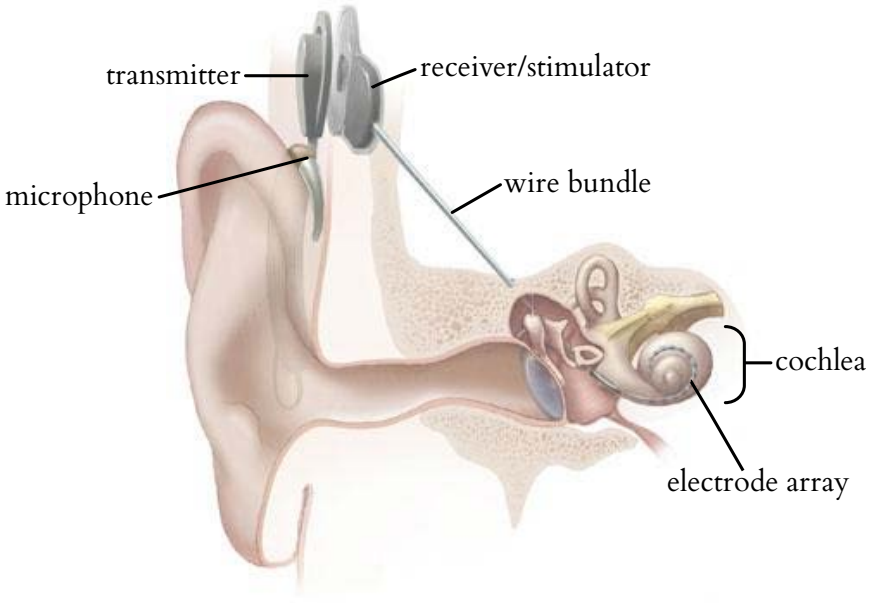

Figure 2.1: A cochlear implant system[1]. Sound is detected with an external microphone and transmitted electromagnetically through the skin to a receiver/stimulator unit implanted under the skin, which delivers electrical impulses to an electrode array implanted within the cochlea.

The current surgical procedure for cochlear implantation (CI) requires a mastoidectomy, in which an open cavity approximately 35 mm deep is created in the temporal bone behind the ear using a hand-held surgical drill. During the procedure several sensitive structures embedded in the bone must be identified and preserved, while the surgical drill passes within a few tenths of a millimeter of them. These include the facial nerve, damage to which results in ipsilateral facial paralysis, and the chorda tympani, damage to which results in ipsilateral loss of taste in the tongue. These two nerves are separated by approximately 2 mm at the facial recess, through which the drill and electrode array must pass. To prevent injury, the surgeon must relate a three-dimensional mental map of critical subsurface features to anatomical landmarks exposed during drilling. To accomplish this he/she must rely on hand-eye coordination and memory to avoid accidentally damaging these nerves or encroaching on the ear

[0]Image: National Institutes of Health, Department of Health and Human Services.

canal, which can lead to chronic infection. To potentially enhance patient safety and reduce trauma, it is desirable to automate this procedure, removing reliance on human hand-eye coordination, spatial reasoning, and memory. Percutaneous Cochlear Implantation (PCI) is a new surgical procedure designed to achieve this using image guidance, but the procedure relies on the availability of a microstereotactic frame custom-made for each patient to guide the drill along a linear trajectory from the lateral skull to the cochlea [25], [26].

Microstereotactic frames such as the STarFix (FHC, Inc., Bowdoin, ME) offer the prospect of submillimetric accuracy. They are rigid fixtures that are specifically manufactured for each patient and each clinical target, which are anchored directly to the bone using bone screws. The STarFix has achieved accuracies of 0.42 ± 0.15 mm deep in the brain [22]. However, the drawback of using the STarFix is a disruption of clinical workflow. The procedure for obtaining a STarFix is to implant anchors into the skull of the patent, scan the patent (e.g. using Computed Tomography (CT)), send the image data to the manufacturer, and wait 2-4 days while the device is manufactured and transported to the hospital. Only then can the surgery take place.

To address this time delay, an alternate type of microstereotactic frame, known as a Microtable, has been developed by Labadie, et. al. at Vanderbilt University [27]. This frame can be manufactured in less than five minutes using a standard computer numeric control (CNC) machine, followed by autoclave sterilization. However, it also requires a machine shop and machinist close to the operating room and on call at all times when a PCI surgery may occur.

PCI begins with placement of three self-tapping metal anchors with spherical heads into the temporal bone. A computed tomography (CT) scan of the temporal bone region, including the anchors, is then acquired. Custom planning software is used to automatically segment the structures of the inner ear [28, 29], determine an optimal trajectory to the cochlea [30], and localize the centers of the spherical

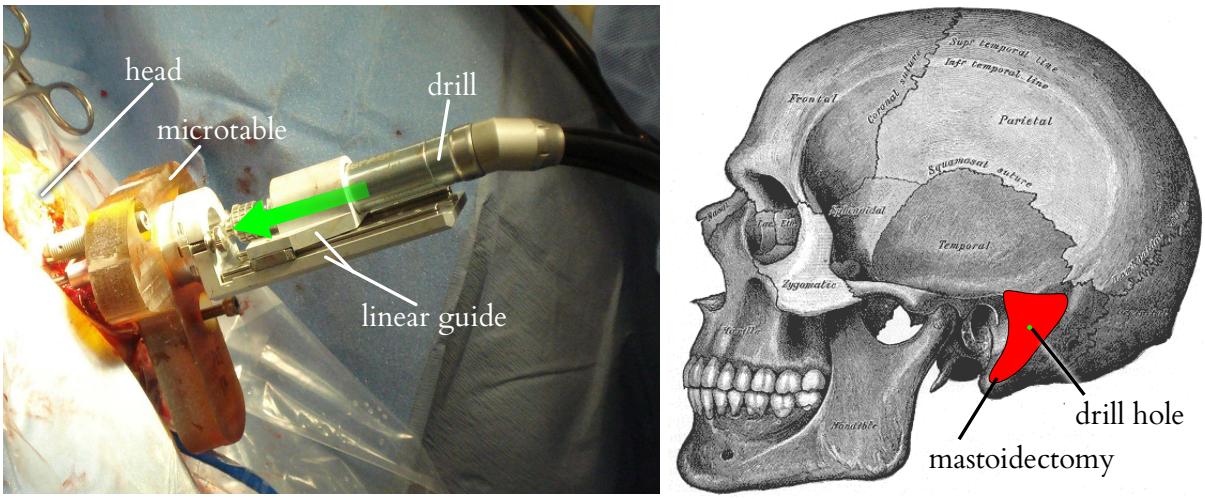

(a) (b)

Figure 2.2: (a) The Microtable, mounted on a patient during the clinical validation of PCI, which is a minimally invasive technique for CI. Though a skin incision was required for the clinical validation protocol pictured, in clinical practice the drill is intended to pass through a small puncture in the skin, with no incision required. (b) Comparison of the region of bone removed during a standard mastoidectomy with the small drill hole required to access the cochlea using the minimally-invasive approach.

heads in image space. Next, a customized Microtable is automatically designed by a custom software program, using the locations of the spheres and desired target as inputs.

The Microtable itself consists of a flat slab of polyetherimide supported by three legs that attach to the bone-implanted anchors. The Microtable is manufactured using a CNC milling machine, and then is sterilized and attached to the bone anchors as shown in Fig. 2.2. A mechanical coupling allows for secure attachment of a drill [27] and then a robotic [31] or manually powered [32] electrode insertion tool. A targeting accuracy of 0.37 ± 0.18 mm [27] has been demonstrated with the microtable. PCI has also been validated on human cadaver temporal bone specimens [33]. Though PCI has not yet been used for full cochlear implant surgery in a live patient, it is currently being clinically evaluated in human cases [25], and trajectories from these human cases comprise the clinical dataset we use in this chapter. We hypothesize that PCI will reduce invasiveness, enhance patient safety, and have the added advantage of reducing operating time from a current average of 170 min [34] to a duration consistently below

60 min.

While experimental results for PCI are promising and it may be feasible to install miniature machine shops in some hospitals, it would be ideal to remove the need for the machine shop and a machinist altogether. This is the purpose of the Automated Image-guided Microseterotactic (AIM) Frame that is the subject of this chapter. The AIM Frame is a bone-attached miniature parallel robot. It was inspired by prior examples of bone-attached robots in medicine, particularly the pioneering work of Shoham et al. [15], who introduced a bone-attached parallel robot for orthopedic and spinal procedures. The device is now marketed as the Mazor Renaissance robot [35]. While neurosurgery has been performed with this robot [36,37], sufficient submillimetric accuracy and precision for PCI surgery has not yet been demonstrated. Subsequent to Shoham et al.'s work, bone-attached parallel robots have been developed for knee arthroplasty by Plaskos et al. [38], Song et al. [39], and Wolf et al. [40]. Parallel robots have been favored for bone-attached surgery due to their stiffness, high payload-to-weight ratio, and potential for high positioning accuracy.

2.2 Surgical workflow

Our current AIM Frame prototype, shown in Fig. 2.3, consists of a robot that attaches to a rigid mounting platform which we call a Pre-Positioning Frame (PPF). The PPF attaches directly to the skull with bone anchoring screws. Electronic control circuitry is housed in an separate enclosure that is connected to the robot with detachable cables.

The surgical workflow for PCI with an AIM Frame is summarized in Fig. 2.4. First, the PPF is attached to the skull using bone screws. Next, a CT scan is acquired that enables identification of both patient anatomy and the three metal spheres on the top of the PPF. Software previously developed for PCI path planning (discussed in Sec. 2.1) is then used to segment relevant anatomy, localize the centers of the spheres, and plan a safe trajectory to the cochlea relative to the sphere locations. The AIM Frame

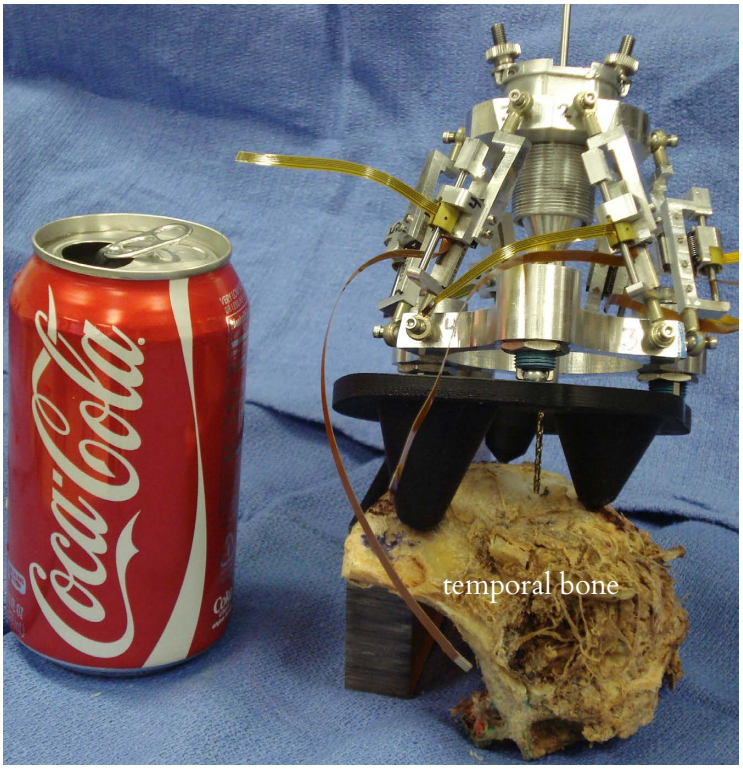

(a)

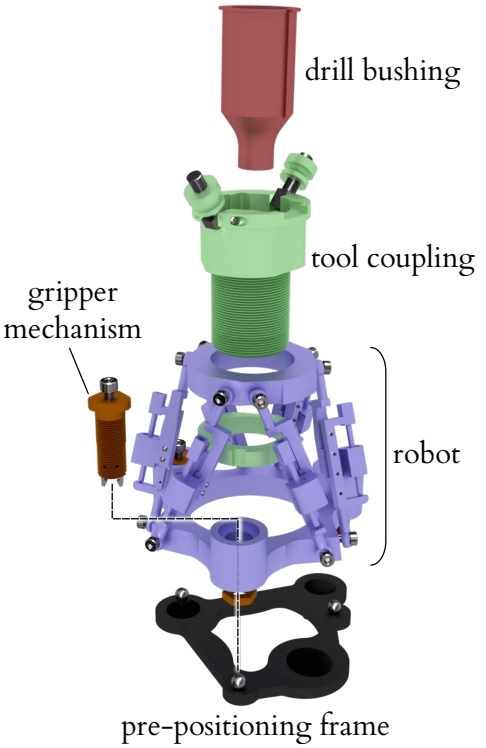

(b)

Figure 2.3: (a) The AIM Frame prototype attached to a human cadaver temporal bone. (b) The AIM Frame system includes a pre-positioning frame (PPF), which is attached to the skull with self-tapping screws. The robot, a 6–6 Gough-Stewart platform, is attached to spherical fiducials on the PPF using three gripper mechanisms. The robot end-effector platform supports a tool coupling for attachment of a drill press and other implantation tools. A drill bushing prevents drill bit deflection.

(which is not yet attached to the PPF) is then configured using its actuators so that a tool attached to its top platform will be aligned with the desired trajectory, to the PPF. The robot's actuators are then locked and the robot disconnected from its power and control electronics. The robot is then attached securely to the spheres on top of the PPF, as shown in Fig. 2.3. The assembled system functions as a customized, rigid microstereotactic frame, and a surgical drill and implant insertion tool are attached to it to perform the surgery.

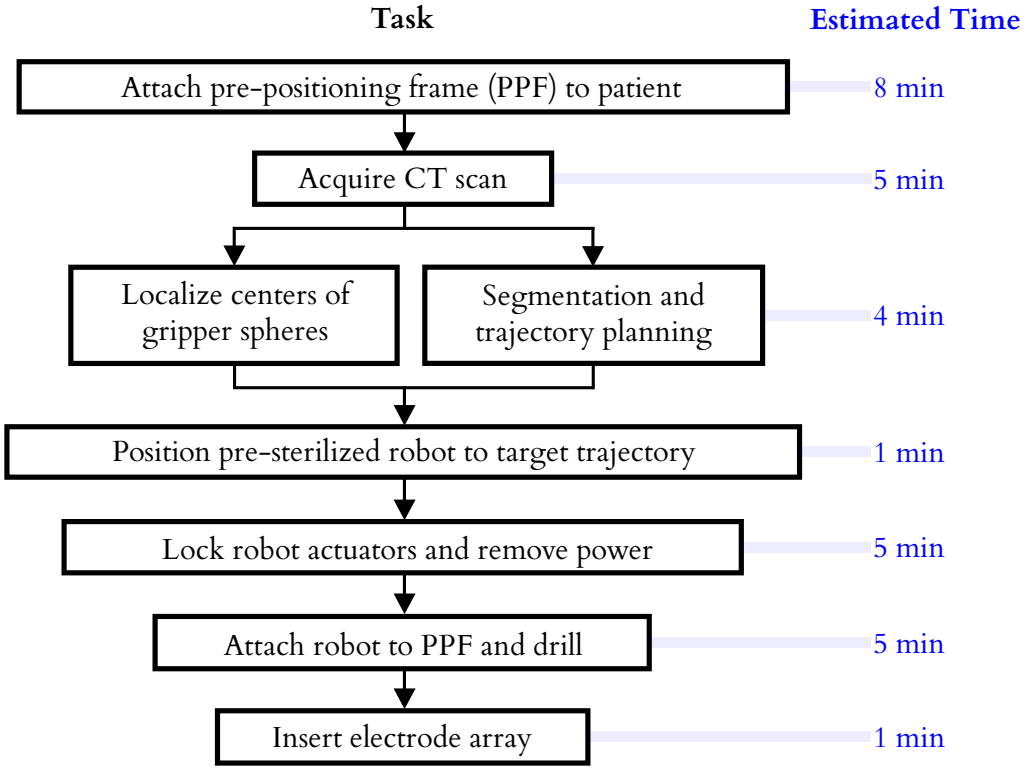

Figure 2.4: The surgical workflow for PCI using the AIM Frame.

2.3 AIM Frame Robot Design

2.3.1 Clinical Dataset Processing: Obtaining Drill Trajectories

To design the AIM Frame, i.e. choose robot dimensions and PPF geometry, we first obtained a clinical dataset consisting of ten patient CT scans from prior PCI clinical validation studies [25], described in Sec. 2.1. The clinical data consisted of CT scans of 10 patients which were collected after the spherical bone anchors had been attached. Each patient CT scan was processed using an atlas-based approach to automatically segment the structures of the ear and identify a safe trajectory for PCI [28–30]. An example computer rendering of the results of this segmentation and the planned trajectory is shown in Fig. 2.5.

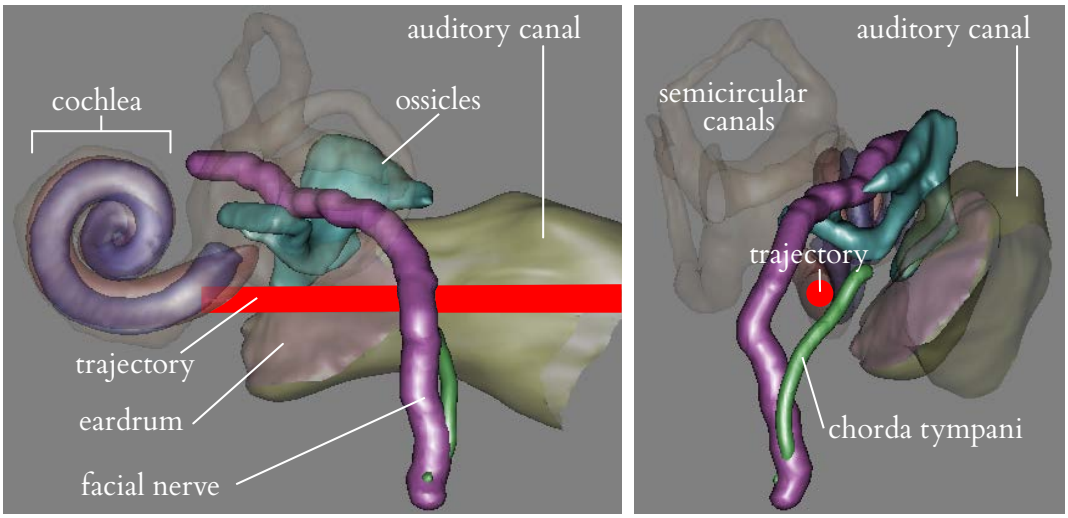

Figure 2.5: Patient CT scans are processed by custom software that automatically segments critical structures and calculates an optimally safe trajectory to the cochlea. The output of the segmentation is shown here with a lateral view of the trajectory (a) and with the viewing plane orthogonal to the trajectory (b).

All the ten trajectories were transformed to a common coordinate system defined by the atlas, in order to define the necessary workspace of the AIM Frame. This transformation was achieved by means of two rigid registrations, both accomplished using the standard mutual information method [41]. The first roughly aligned the head in the patient CT scan with the head in the atlas. The ear region was then cropped in the two CT scans and a second rigid registration was performed to refine the alignment of this cropped region of interest. The result of this process was a collection of clinical trajectories in the same coordinate frame, which can be used to determine the PPF design and the AIM Frame workspace (See Fig. 2.6).

2.3.2 The Pre-Positioning Frame

The geometry of the PPF is selected to align the nominal robot trajectory (i.e., the trajectory when all AIM Frame legs are equal lengths and located at the middle of their travel ranges), with the average trajectory in the clinical dataset. The prototype PPF used in the initial experiments described in this

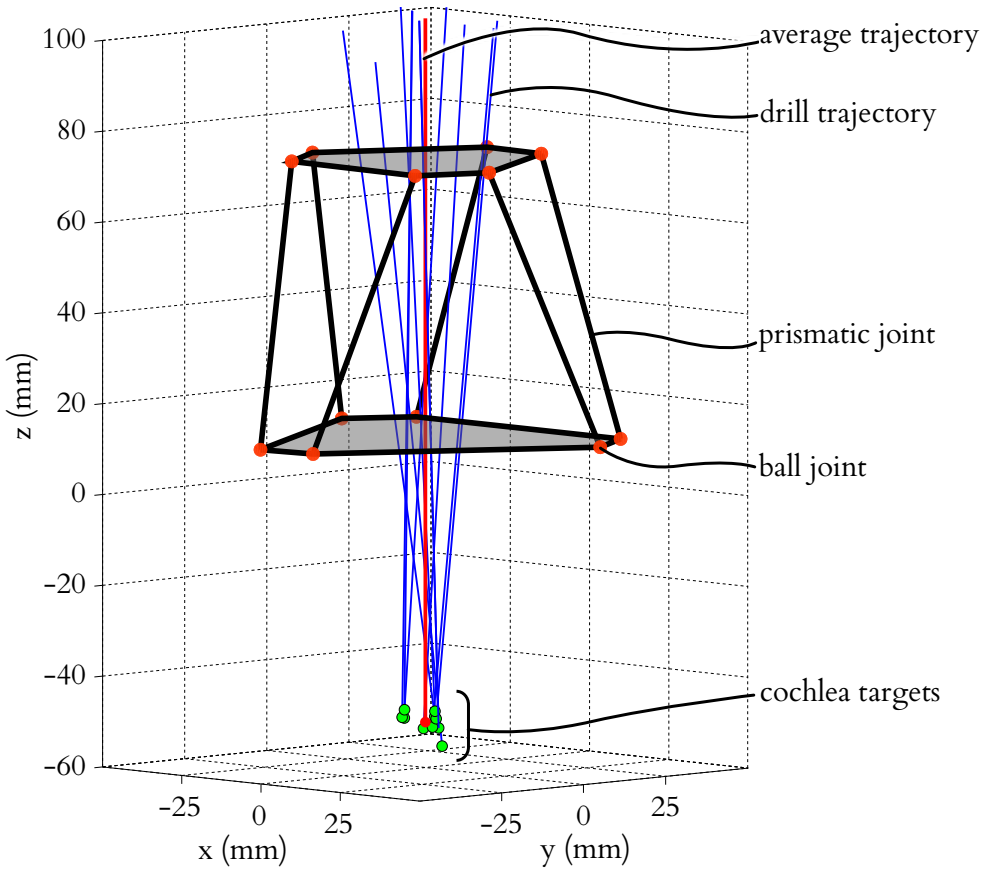

Figure 2.6: A schematic diagram of the AIM Frame with ten PCI trajectories from prior microtable clinical trials. The robot is oriented by a pre-positioning frame (not shown), so that that its nominal trajectory is centrally located with respect to the clinical trajectories..

chapter is shown in Fig. 2.7. It was fabricated from acrylonitrile butadiene styrene (ABS), though in a future clinical version we intend to replace this material with a sterilizable, radiolucent material such as polyethermide or polyether ether ketone (PEEK). The robot can be attached to the spheres on top of the PPF using the gripping mechanism described in [27]. The same spheres also serve as fiducial markers for performing a point-based rigid registration of the CT image space to the robot's coordinate frame.

2.3.3 Actuators and Encoders

The robot is actuated by six Squiggle SQL 3.4 linear piezoelectric motors (New Scale Technologies; Victor, NY) [42]. These motors were chosen for their high power-to-weight ratio, small size, and high

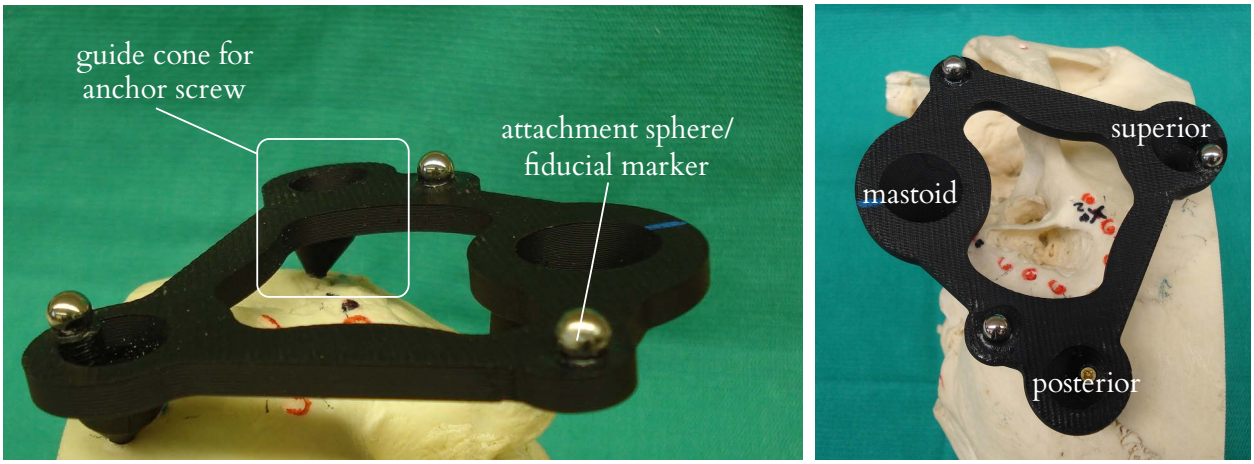

(a) (b)

Figure 2.7: An oblique (a) and top (b) view of a pre-positioning frame (PPF) attached to the left ear region of a skull,showing the mastoid, superior, and posterior bone screw locations. The PPF is used to orient the attached robot for efficient utilization of its workspace, and for secure attachment of the robot to the patient.

resolution. Each motor weighs 1.2 g and can generate bidirectional motion with 2 N maximum output force. The stator package is approximately 3.4 mm $\times$ 3.4 mm $\times$ 10 mm. The motors can extend and retract at 4 mm/s while exerting 1 N. We estimate that the required positioning time for PCI trajectories will be under 5 s.

Each motor is enclosed in an aluminum fixture forming a prismatic joint which may be extended and retracted by the motor, as shown in Fig. 2.8. The fixture also houses a TRACKER Position Sensor (New Scale Technologies; Victor, NY) to measure leg displacement. The TRACKER is a Hall Effect-based linear encoder with a minimum resolution of 0.5 µm. An absolute reference position can be found with each encoder, which we used to determine a reference pose for the robot. We custom manufactured magnets for each TRACKER sensor to measure displacements up to 13.3 mm.

The suitability of these motors for direct exposure to repeated sterilization is not known, though we have subjected one motor to a standard autoclave sterilization cycle (270.0°F, 4 min sterilization time, 1 hr, 13 min total cycle time), and another to ethylene oxide gas sterilization (130°F, total cycle time

of 14 hr, 59 min). Qualitatively, we did not observe any degradation of performance for either motor following sterilization.

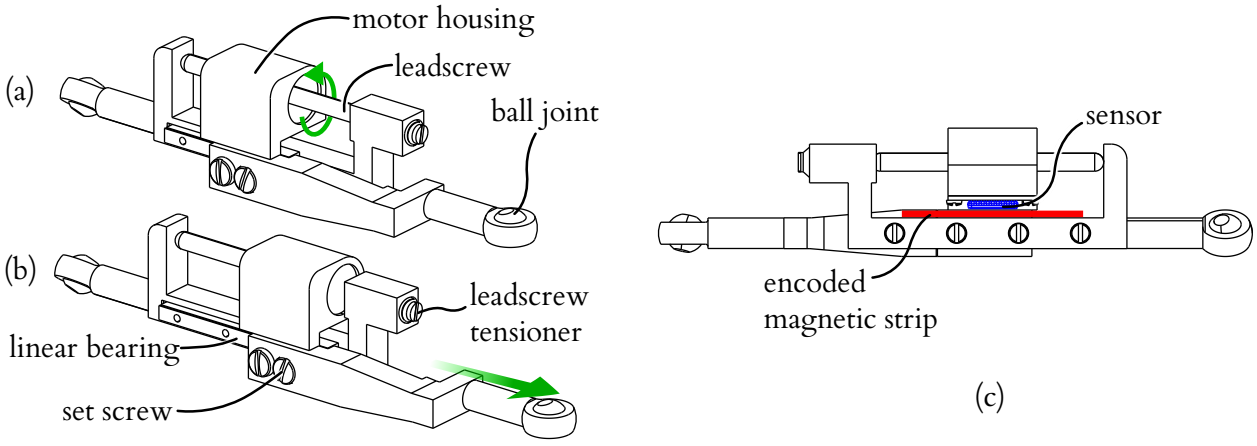

Figure 2.8: Each leg joint is powered by a piezoelectric motor, which rotates a leadscrew. Rotation of the leadscrew (a) causes the motor to advance along the leadscrew and translate the the ball joint connected to the motor housing with respect to the ball joint at the opposite end of the leg, as shown in (b).

2.3.4 Robot Structure

We chose the Gough-Stewart 6–6 parallel robot architecture for the AIM Frame, primarily for ease of implementation, since it is a standard type of parallel robot. Our prototype consists of two aluminum platforms connected by six actuated prismatic joints as shown in Fig. 2.3. The ends of each prismatic joint are passive ball joints, arranged in a plane to form the vertices of a hexagon on each platform. The total material cost for the AIM Frame prototype (not including the control PC) was approximately $4,500.

The design parameters for the robot structure are shown in Table 2.1. The arrangement of joint attachment points on a parallel robot may be chosen, in general, to optimize various kinematic performance metrics. Our objective was to enlarge the robot's workspace to include the range of patient trajectories while maintaining a compact robot volume. Selection of parameters to meet this objective could be obtained by numerical optimization, but it was necessary to consider several possible part

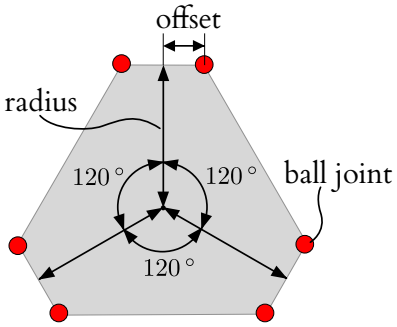

Table 2.1: Robot design parameters

Parameter	**Value** (mm)
Top platform radius	27.6
Top platform offset	8.4
Bottom platform radius	42.2
Bottom platform offset	8.4

interferences. For example, the legs may collide with each other, with the platforms, and with the drill bit and bushing. Further constraints include the limited angular motion of the ball joints and the leg joint encoder limits. It is possible to encode such constraints for numerical optimization (see, for example, [43, Ch. 7] and [44]), but we designed the robot by manually manipulating parameters of the robot CAD model to eliminate occurence of such interferences when positioned to each trajectory in our clinical dataset, which were partitioned into subgroups for use with three PPFs.

We endeavoured to enlarge the workspace as far as possible beyond the extent of the clinical dataset, but there is a trade-off between the workspace of the robot and the number of different PPFs needed to adapt the AIM Frame to general patient population. It would be ideal to have just one PPF, but it would also be ideal to have a very small and lightweight robot – both make the system easier to use for the clinical team. However, for a given robot design and desired workspace, these two goals may not be simultaneously achievable. If multiple PPFs are included in the system, we believe that a small number, perhaps 3-5, will be possible to include without significant detriment to ease of use. All would be presterilized and available in the operating room. They could be color coded, and the correct one selected by registering the attachment points of a PPF to a CT scan of a patient's temporal bone. Using the planning software described above, a patient trajectory could be projected into the image of the registered PPF prior to surgery to determine if the robot is adjustable to the trajectory using that PPF.

We require more clinical data before we can conclusively characterize the spread of necessary

clinical trajectories and determine the optimal size of robot vs. number of PPFs. For our prototype, the number of necessary PPFs was three. Narrower legs with longer travel limits could be used in a future version of the robot, which may make it possible to use a single PPF.

2.3.5 Control System

Custom-written control software programmed in MATLAB (Mathworks; Natick, MA, USA) calculates a target pose for the robot's top platform using trajectory data obtained using the planning software described in Sec. 2.1. The control software then plans a path from the robot's home pose to the target pose, and corresponding trajectories for each leg are calculated using an inverse kinematic model [45]. The user enters the leg trajectory data into New Scale Pathway software (New Scale Technologies; Victor, NY) which drives the motors. Each motor is powered by a MC-1100 motor controller (New Scale Technologies; Victor, NY). The motor controllers are contained in an electronics enclosure and connected via USB cables to a personal computer. The robot may be detached from the control electronics for sterilization (it is not necessary to sterilize the electronics enclosure, since it is sufficiently remote from the patient and can be covered in a sterile plastic bag in the operating room).

2.3.6 Attachment of surgical tools

The top platform of the robot includes a mechanical coupling that enables rapid tool changes with accurate mating. During PCI surgery two tools will be attached: a drill press [26], and a cochlear implant insertion tool [32]. Thumbscrews allow the drill press and insertion tool to be firmly coupled to the mating fixture on the top plate of the AIM frame. Attached to the bottom of this plate is a bushing that supports the drill bit up to the skull entry point, preventing drill bit wander during drilling. The AIM Frame with surgical drill attached is shown in Fig. 2.9.

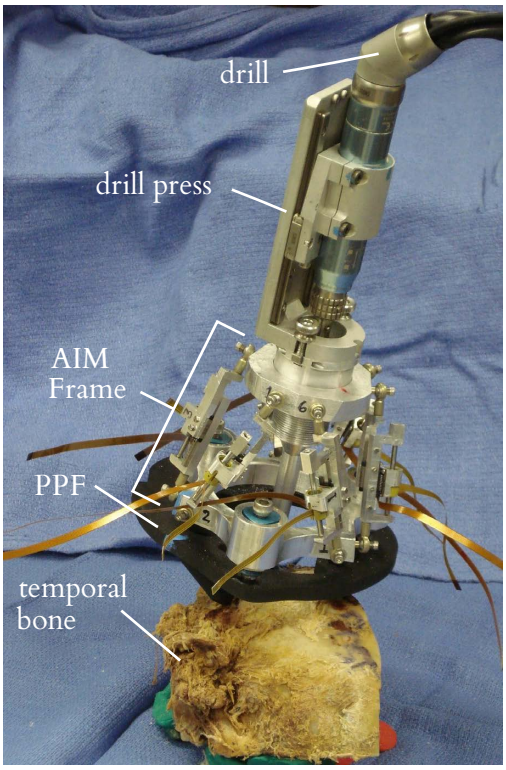

Figure 2.9: The AIM Frame with attached drill press.

2.4 Experimental Results

2.4.1 Free-Space Targeting Experiment

To evaluate the targeting accuracy of the AIM Frame robot, we used the virtual target method introduced by Balachandran et al. [22], in which targets are represented as points in space relative to a coordinate frame defined by fiducial markers embedded on a phantom. The ten trajectories obtained from the clinical dataset were used as targets, as partitioned for use with the three PPF's as described in Section 2.3.4.

The phantom, shown in Fig. 2.10, was milled from an acrylic block with overall dimensions of 6 in $\times$ 6 in $\times$ 1.5 in. Three 0.25 in diameter steel spheres were embedded on the phantom to represent the PPF spheres and 19 steel spheres of 3 mm diameter were embedded on the phantom to act as fiducial markers. The locations of the centers of all the steel spheres were measured using a FARO GagePlus

Measurement System (FARO Technologies Inc., Lake Mary, FL, USA). The ten target trajectories were then defined relative to a coordinate frame established by the locations of the fiducial markers in the FARO space.

The AIM Frame was attached to the phantom, and a measurement probe consisting of a rod with spherical steel ends was affixed to the top platform, as shown in Fig. 2.10(b). This probe was used to represent the drill axis, and the bottom sphere was located 76 mm along the drill trajectory, as measured from the center of the top platform. Using the locations of the spheres, as measured by the FARO, the drill axis can be defined, and the final position of the drill bit at the cochlea (at the planned depth) in CT space can be extrapolated.

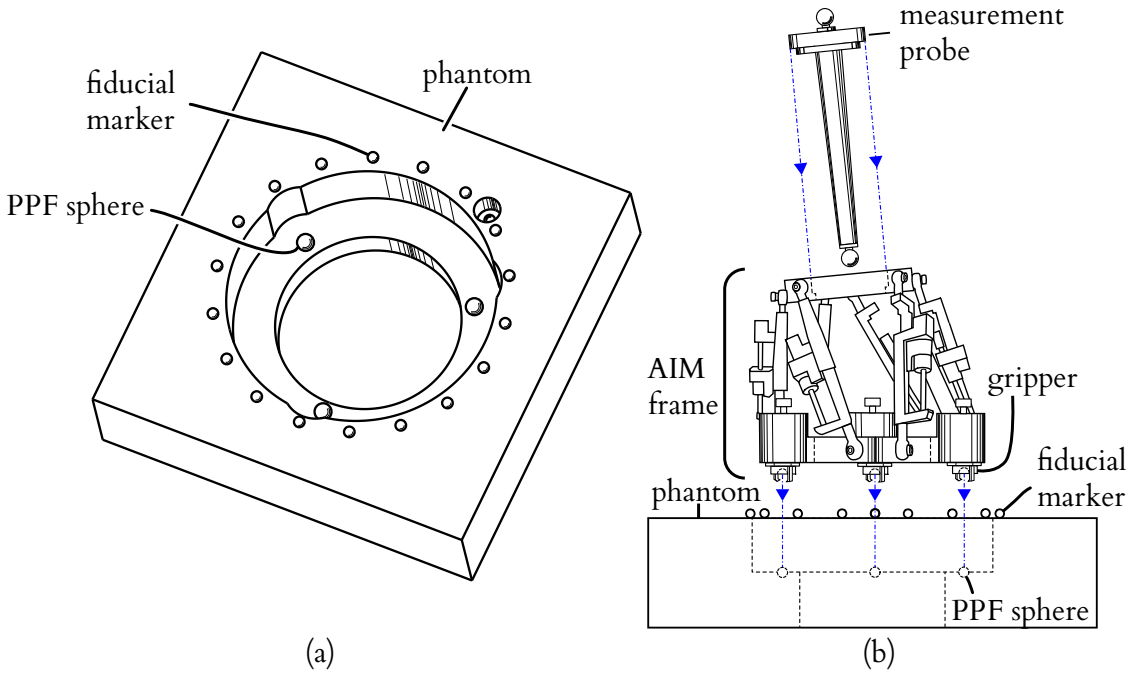

Figure 2.10: (a) Phantom used for free space targeting trials in a CT scanner. The phantom was milled from a block of acrylic. Targets were projected into the coordinate space established by the three PPF spheres on the phantom that represented the top surface of the PPF. A ring of 19 additional fiducial spheres were localized in CT images and were used to register targets from the clinical dataset to the phantom's coordinate space. (b) The AIM Frame was attached to the phantom, and the drill was replaced with a measurement probe aligned with the drill bit axis. Two spheres on the measurement probe were localized in CT images to find the drill bit axis.

Each trial began with the robot in a neutral pose. The robot was then positioned to a target trajectory, and then returned to the same neutral pose in preparation for the subsequent trial. A CT scan of the phantom with attached robot was acquired at each target and neutral pose using an xCAT ENT CT scanner (Xoran Technologies, Ann Arbor, Michigan, USA), which provides scans with an isotropic voxel volume of 0.4 mm^3. Each target position was repeated three times, to obtain a total of 30 scans.

To measure the accuracy of the robot, the fiducial spheres on the phantom and the spheres on the probe were first localized in each CT scan. Fiducial locations in the CT space and FARO space were then registered using a rigid, point-based registration method [46]. The extrapolated drill tip location in the CT space was then transformed to the FARO space, and the targeting error was computed as the distance between this transformed point and the desired target defined in the FARO space.

The targeting error, also known as target registration error (TRE), was measured for each trial as described above, and the mean targeting error due to the AIM Frame robot was found to be 0.20 mm, with a standard deviation of 0.07 mm. Results for all targeting experiments are shown in Figure 2.11.

2.4.2 Cadaver Drilling Experiment

To validate the performance of the entire AIM Frame system, we performed a drilling experiment on a cadaveric temporal bone specimen. First, a PPF was fabricated for the specimen and then attached to the bone. The lengths of the PPF legs, measured perpendicularly to the plane described by the centroids of the fiducial spheres, were 31.6 mm (mastoid), 40.9 mm (superior), and 18.8 mm (posterior). Using the xCAT scanner, the bone with the PPF attached was then scanned. The scan was then segmented, the fiducials located, and the drill trajectory selected by the segmentation/planning software described in Sec. 2.1. The AIM Frame legs were then adjusted to the corresponding lengths, the legs locked using set screws, and the AIM Frame detached from the control circuitry, the surgical drill attached to the AIM Frame, and AIM Frame and mounted to the PPF. Fig. 2.9 shows the AIM Frame with the drill press

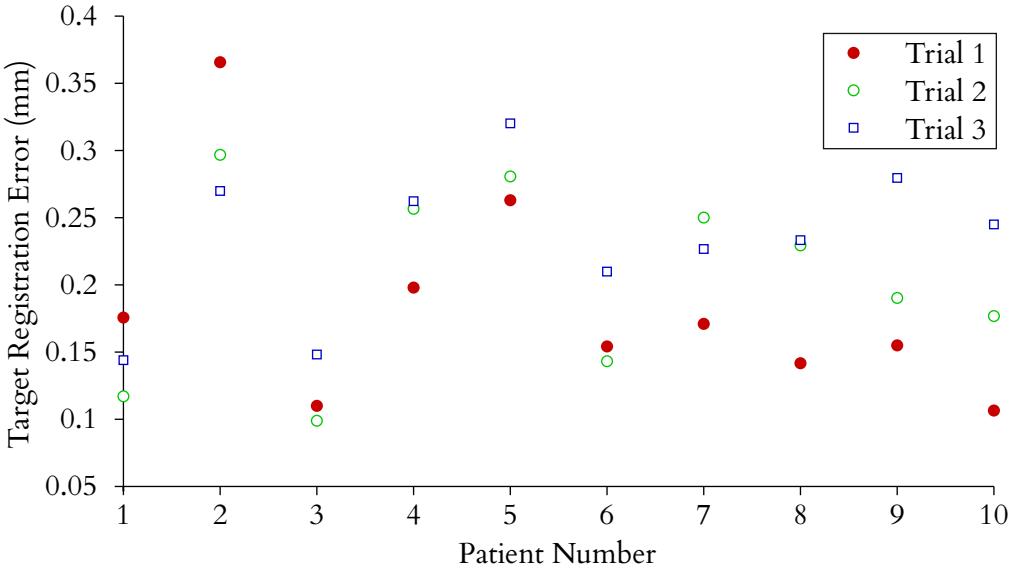

Figure 2.11: Results from free-space targeting trials using the CT phantom. In each trial, the robot was aimed for drilling to cochlear targets planned for each of the ten patients in the clinical dataset. The trial was repeated three times, for a total of thirty individual measurements.

attached to the bone.

The trajectory length of 148 mm determined by the control/planning software was then used to set a mechanical stop on the drill press. A 5/64 inch (1.98 mm) diameter twist drill bit with a 118° point angle was locked into a surgical drill (Anspach Corporation, Palm Beach Gardens, FL, USA). Drilling was performed at approximately 30,000 rpm, and was completed in 1 min, 26 s. A final CT scan was acquired of the bone with the PPF still attached and with the drill bit in the drilled hole to evaluate the drilling performed. In this post-drill CT, the spheres on the PPF were automatically localized and the drill tip was manually identified. The sphere locations were used to register the pre-drill CT to this post-drill CT via point registration [46]. The planned trajectory in the pre-drill CT was transformed to the post-drill CT using this registration. The targeting error, which is the distance between the planned cochlear target and the drill tip, was determined to be 0.38 mm.

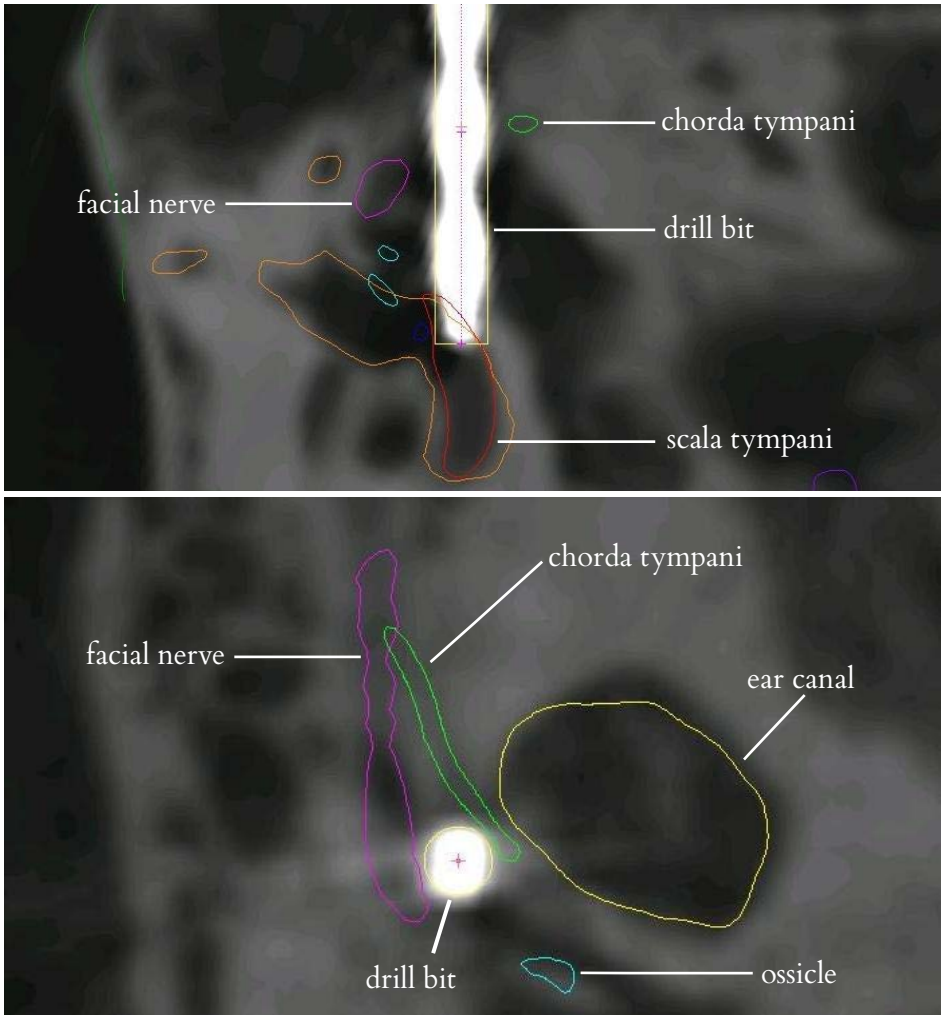

Figure 2.12: Two views of the post-drill CT scan with segmented anatomy and the drill bit that was guided by the AIM Frame.

2.5 Conclusion and Future Work

In this chapter, we investigated robot-assisted, minimally invasive cochlear implant surgery. Recently, this surgery has been performed on cadavers using a serial robot that is fixed to the operating room table [47], however this approach requires an external tracking system and fixation of the patient's head to the table. The bone-attached parallel robot approach described in this chapter does not require head fixation or optical tracking, nor does it require attachment to the operating room table with a rigid and

obtrusive frame.

The system we have presented has comparable accuracy to a microstereotactic, but retains the adjustability of a traditional stereotactic frames. The device simplifies the workflow of microstereotactic surgery (and specifically PCI surgery), by eliminating the need for a machine shop in the hospital or alternatively a delay between bone-implanted fiducial placement and surgery to have the fixture fabricated off site. We believe this elimination of delay and infrastructure will be a key advancement for widespread deployment of the PCI technique in the future.

However, some additional work is needed before the AIM Frame can be deployed clinically. We are currently accruing additional clinical trajectories as human microtable cases are conducted, and we intend to use these to evaluate the necessary workspace of the AIM Frame together with the optimal number of PPFs. We will statistically evaluate these trajectories to modify the AIM Frame design to account for patient-to-patient variability in both trajectory orientations and anchor positions. After concluding this analysis, we intend to perform a clinical evaluation of the AIM Frame, using methods similar to those presently being used in PCI clinical trials.

We believe that the AIM Frame concept will be advantageous for other intracranial procedures requiring high positional accuracy. Examples include petrous apex drainage, mastoidectomy, and deep brain simulation. Some of these (e.g. petrous apex drainage) will be similar to PCI in that they will involve access to a specific point in image space via a straight-line drill trajectory, and in these an AIM Frame would work in a conceptually similar way to what we have described in this chapter for PCI. However, some future procedures (e.g. mastoidectomy and deep brain stimulation) may require that the AIM Frame be actively moved during surgery to machine bone or realign a surgical tool based on intraoperative feedback. These examples indicate the potential of the AIM Frame concept to assist with diverse future clinical tasks in intracranial surgery. Thus we view the initial feasibility study for PCI

presented in this chapter to be a first step toward a family of highly accurate, yet adjustable, AIM Frame guidance fixtures for a variety of intracranial image guided surgical procedures.

CHAPTER 3

ROBOTICALLY-ADJUSTABLE MICROSTEREOTACTIC FRAMES FOR IMAGE-GUIDED NEUROSURGERY

Stereotactic frames are a standard tool for neurosurgical targeting, but are uncomfortable for patients and obstruct the surgical field. Microstereotactic frames are more comfortable for patients, provide better access to the surgical site, and have grown in popularity as an alternative to traditional stereotactic devices. However, clinically available microstereotactic frames require either lengthy manufacturing delays or expensive image guidance systems. We introduce a robotically-adjusted, disposable microstereotactic frame for deep brain stimulation surgery that eliminates the drawbacks of existing microstereotactic frames. Our frame can be automatically adjusted in the operating room using a preoperative plan in less than five minutes. A validation study on phantoms shows that our approach provides a target positioning error of 0.14 mm, which exceeds the required accuracy for deep brain stimulation surgery. This chapter was presented at the 2013 SPIE Medical Imaging conference [24].

3.1 Introduction

Deep-brain stimulation (DBS) is an FDA-approved treatment for individuals suffering from certain movement disorders that cannot be effectively treated with medications and for treatment of some affective disorders. Preoperative imaging (MRI or CT) is used to identify a disease-specific target structure in the brain, e.g., the subthalamic nucleus or globus pallidus interna, and plan an electrode insertion trajectory. Then, electrodes are surgically implanted. Leads pass from the electrodes out through the skull under the scalp to a generator under the skin that electrically stimulates the target structures to alleviate symptoms. Accuracy of 2 mm or better is required when placing the electrodes to

achieve effective treatment and to avoid undesirable side effects [48].

The standard guide for implanting electrodes during DBS surgery is the stereotactic frame, a rigid device surrounding the head and anchored to the skull by sharpened pins penetrating the scalp and impinging on the skull, as shown in Figure 3.1(a). These devices are heavy and uncomfortable for patients, a particular disadvantage for DBS surgery in which patients must remain awake during the procedure to communicate with the surgeon during a two-hour interaction as electrode positions and voltages are optimized while the effects on symptoms and side-effects are monitored. Stereotactic frames are aimed by manual adjustment of several vernier scales, which may be affected by human error. Flickinger et al. [8] found stereotactic frame adjustment errors in 12 percent of 200 clinical cases, and recommended that two separate observers verify the coordinate settings.

To address the drawbacks of stereotactic frames, two miniature, bone-attached guidance platforms are now available for clinical use. These "microstereotactic" frames are light and neither surround the head nor require vernier adjustment. The first is the StarFix microTargeting Platform (FHC Inc., Bowdoin, ME), shown in Figure 3.1(b), a rigid, lightweight, single-use fixture that is custom-made by means of 3D printing technology [16] and has experienced exponential growth in clinical use over the past decade. It is fabricated off-site causing a two day delay between pre-operative imaging and electrode placement. The second is the NexFrame (Medtronic Inc., Fridely, MN), also a lightweight guidance device that attaches to the skull [49]. The NexFrame imposes no manufacturing delay, but it requires an expensive real-time optical tracking system.

An alternative called the Microtable, which combines the advantages of both StarFix and NexFrame, has been developed at Vanderbilt University for cochlear implantation surgery. Cochlear implantation surgery requires accuracy of better than 0.5 mm, which traditional stereotactic frames cannot deliver [49,50]. This fixture also uses bone-attached markers as a reference for targeting a surgical

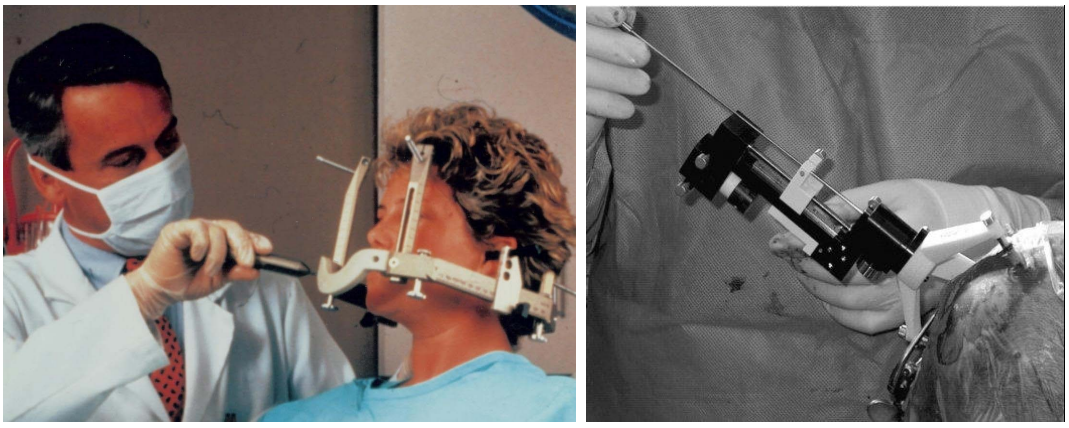

(a) (b)

Figure 3.1: (a) Traditional stereotactic frames are heavy and uncomfortable for patients. These frames require manual adjustment, which may lead to targeting errors (image source: Nuclear Regulatory Commission) (b) Microstereotactic frames, such as the STarFix microTargeting Platform, are custom-manufactured at a special facility, which creates a delay between imaging and surgery.

target in a preoperative CT scan [27]. Like the StarFix, the Microtable is custom-made, but it can be fabricated in under four minutes on a portable computer numerical control (CNC) milling machine.

Other approaches to making customized fixtures have been proposed. For example, Rajon et al. [51] developed custom-manufactured biopsy guides for stereotactic neurosurgery. However, each guide requires three hours to manufacture using a large four-axis milling machine, and it is less accurate than the Microtable. Kobler et al. proposed a passive Gough-Stewart structure as a drill guide for cochlear implantation surgery which requires manual adjustment of six micrometers that are attached to the patient's head [52]. Thiran et al. introduced an adjustable microstereotactic frame for brain biopsies and DBS surgery, but this device relies on an external, manually-adjustable stage to aim the device [53].

Robots can perform positioning tasks with accuracy, speed, and precision, and may thus be beneficial for reducing the time delays and adjustment errors associated with manually-adjusted stereotactic devices. Bone-attached parallel robots have been proposed for neurosurgical procedures by Joskowicz et al. [36], and we have developed a bone-attached robot as a microstereotactic frame for

cochlear implantation surgery [23]. Robotic frames promise rapid and accurate frame preparation, but the costs of precision miniature components may be an obstacle to clinical deployment of such devices.

In this chapter, we introduce a microstereotactic frame that is adjusted by a robot, immobilized, and then attached to a patient for DBS surgery. This approach enables passive frames to be prepared accurately within minutes without manual adjustments, image guidance systems, or lengthy manufacturing delays.

3.2 Microstereotactic Frame Design

Our proposed microstereotactic frame, which we call the "Freeze Frame", is shown in Figure 3.2. The Freeze Frame supports a microTargeting Drive System (FHC Inc.) that advances an electrode into the brain during DBS surgery. The Freeze Frame comprises a circular plate with four legs that are adjusted by a robot to align the frame to the correct trajectory and simultaneously to configure the legs for attachment to four spherical fiducials implanted on a patient's scalp. DBS electrodes may be implanted in either hemisphere of the brain. The Freeze Frame is configurable for either left or right hemisphere implantations.

We designed the Freeze Frame using a set of ten CT scans from patients who underwent left-hemisphere DBS surgery using the STarFix platform at the Vanderbilt University Medical Center. We analyzed these CT scans to characterize the range of trajectories and fiducial configurations that result from variation in both patient anatomy and clinician implantation technique.

The CT scans were processed using WayPoint Planner software (FHC Inc.), which returns coordinates of the titanium bone anchors (FHC Inc.) that serve as both mounting points and planning fiducials for the STarFix platform, a vector along the threaded central hole in each anchor, a target point at the subthalamic nucleus, and an entry point. Additionally, a vector along the anterior commissure-posterior commissure line was manually identified in each patient CT.

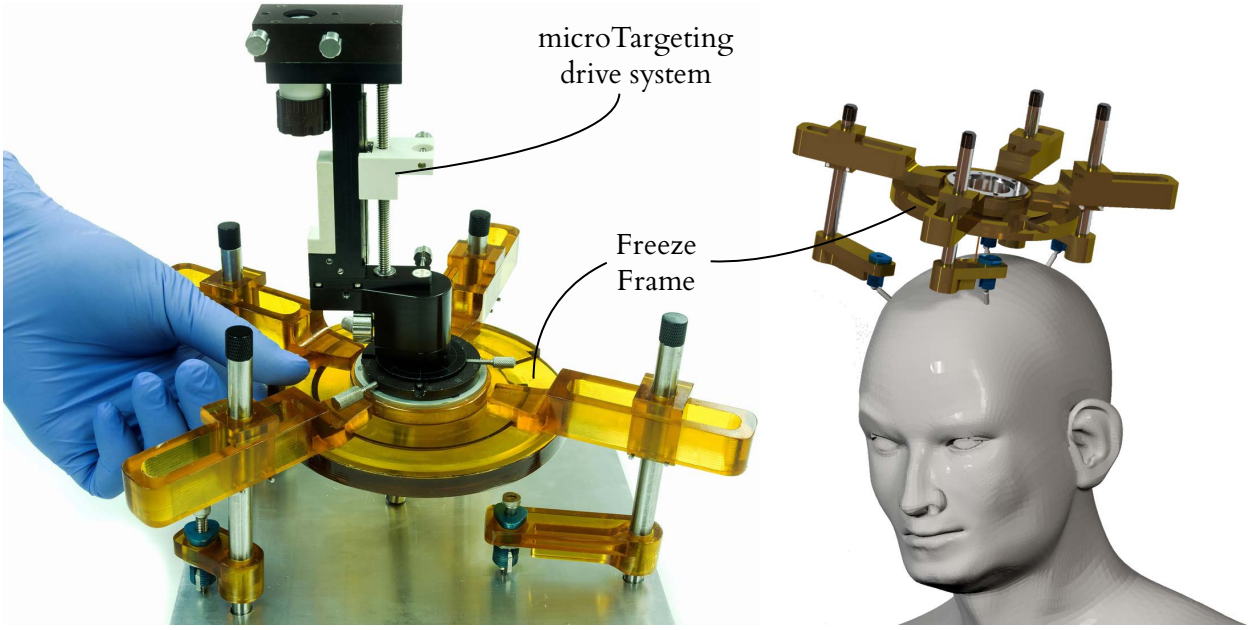

Figure 3.2: (a) The Freeze Frame supports a microTargeting Drive System (FHC, Inc.) that advances an electrode into the brain during DBS surgery. (b) The frame attaches to four fiducial markers that are implanted on the scalp.

Like the STarFix system, our system specifies each trajectory by a target point, an entry point 120 mm above the target point, and the anterior commissure-posterior commissure line. The entry point represents the desired position for the microTargeting Drive System.

To examine the spatial disposition of the bone anchors with respect to each trajectory, we constructed an orthonormal coordinate frame in each CT scan with an origin at the entry point and one coordinate axis aligned with the trajectory vector, as shown in Figure 3.3(a). The cross product of the anterior commissure-posterior commissure vector with the trajectory vector defines the direction of one additional orthogonal axis which is crossed with the trajectory axis to complete to specify the remaining orthogonal axis. We then rigidly registered the coordinate frames and transformed all the spherical fiducial points points to a single coordinate frame located at the entry point origin.

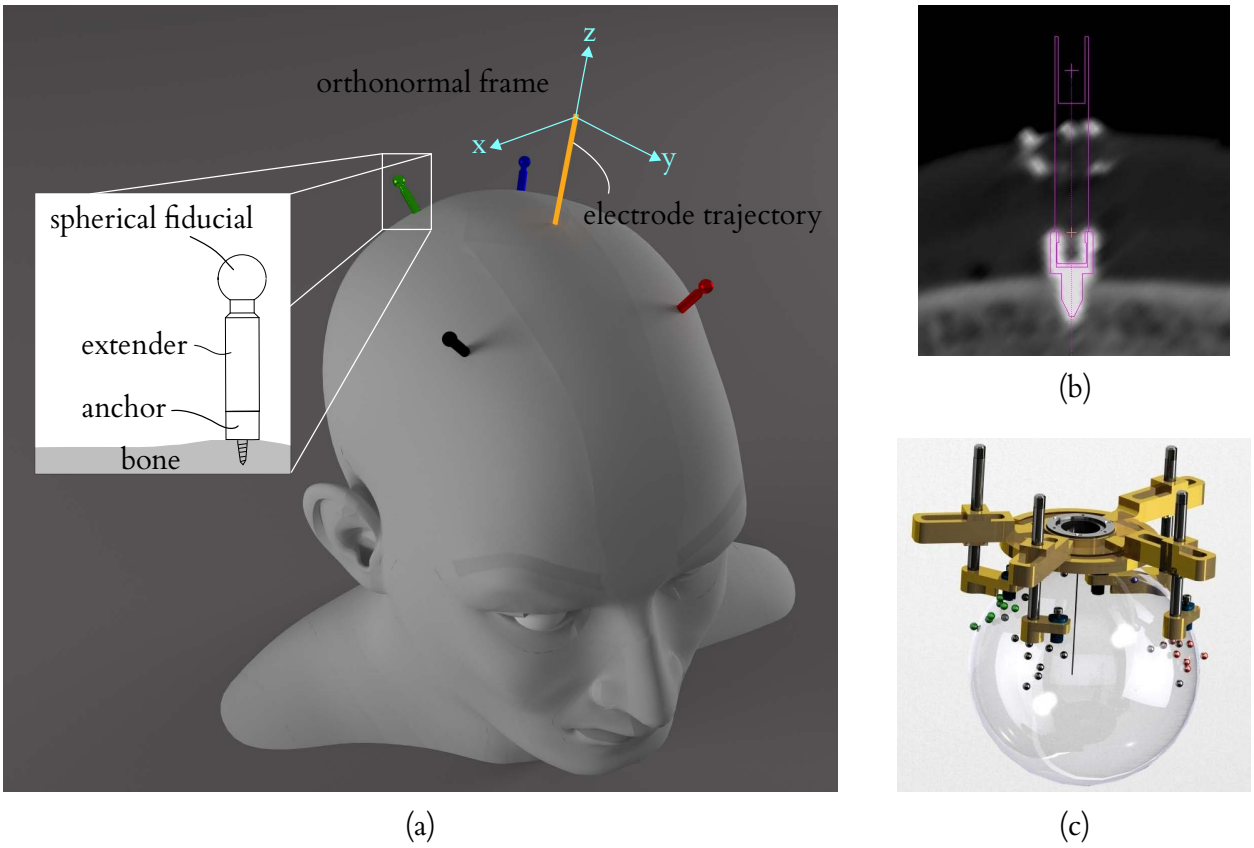

Figure 3.3: (a) Each patient in our dataset was implanted with four bone anchors for mounting a STarFix Platform. We propose to add extenders with spherical fiducials for attachment of the Freeze Frame. (b) The STarFix planning software automatically localizes the anchors. We determined where spherical fiducials would have been located if they were attached to the anchors, instead of a STarFix Platform. (c) When the spherical fiducials are transformed to a single coordinate frame, their positions are approximated by a spherical surface. The space of transformed fiducial spheres were used to specify the dimensions of the Freeze Frame.

The Freeze Frame is designed for mounting to spherical fiducials that were previously developed for the Microtable [27]. Each spherical fiducial has a threaded extender rod that screws into a STarFix anchor. To determine where these spherical fiducials would have been located if extender rods were attached to the anchors on each patient in our dataset, we projected a vector along the central axis of each anchor, and identified points at the distance from the extender base to center of each sphere. In the single coordinate frame, all sphere locations lie within 1 cm of a spherical surface found by the least-squares method, with a radius of 94.5 mm, as shown in Figure 3.3(c). In the Appendix to this

chapter, we examine a larger clinical dataset from 1052 DBS surgeries, and find that the fiducials are also approximated by a sphere for this separate dataset.

The single coordinate frame is convenient for design because all trajectories are transformed to a single line, with patient variation completely represented by four clusters of fiducial points, as shown in Figure 3.3(c). By designing a frame in this space with sufficient adjustability to reach all fiducials, the problem of adjusting to each trajectory in the set is solved implicitly without the need to separately consider trajectory variation.

Four legs provide redundant mechanical support for the circular disc and allow it to be located with six degrees of freedom. Five degrees of freedom are required to specify the position and orientation of the trajectory vector, and a sixth degree of freedom is necessary to constrain the angle of an electrode about its own axis. To achieve this targeting flexibility, each leg mechanism is adjustable for attachment to a spherical fiducial occupying the three dimensional space beneath the circular disc.

The leg mechanisms are illustrated in Figure 3.4. The legs are seated in a circular track on the top surface of the circular disc which allows them to rotate about the circumference of the disc. A slot in each leg supports a block that translates in the radial direction. The sliding block has a cylindrical hole that serves as a bearing for a shaft that translates in a direction transverse to the plane of the circular disc and rotates about its own axis. Each shaft is bonded to a foot that supports a gripper mechanism with a hemispherical cup that mates with a spherical fiducial. The gripper mechanisms were previously developed for the Microtable [27], and have been validated in cochlear implantation surgery.

The length of each foot provides an offset distance from the shaft axis to the gripper attachment point, allowing the leg to reach beneath the circular disc. Longer feet are used for the two anterior fiducial locations. The angle of each foot about the axis of the shaft to which it is attached is fixed during the adjustment process by a peg that fits into a hole on the bottom of each foot. The foot angles are

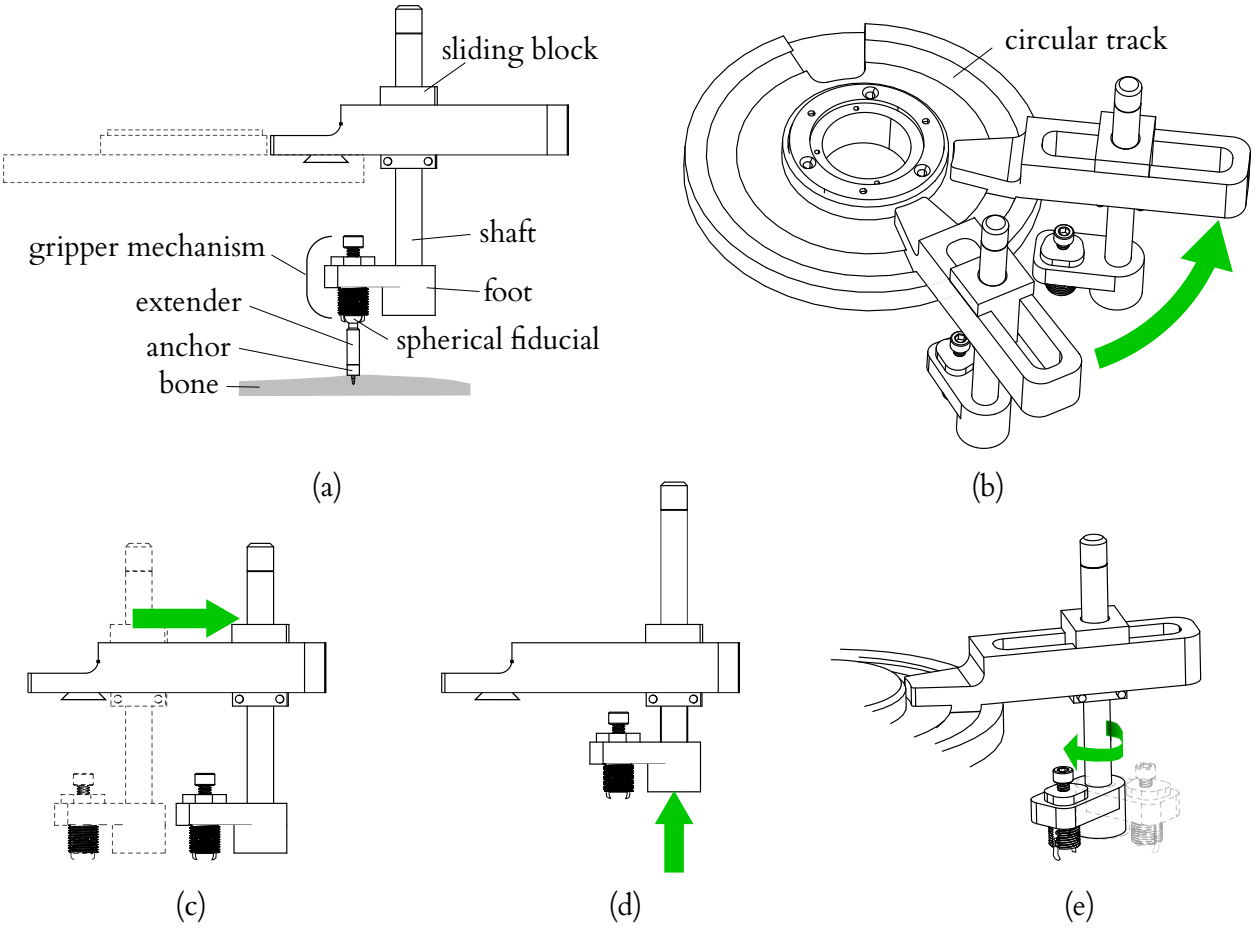

Figure 3.4: (a) Each leg of the Freeze Frame supports a gripper mechanism that fastens to a spherical fiducial on the scalp. (b) A circular track allows each leg to rotate about the circumference of the circular disc. (c) a sliding block translates radially in a slot and serves as a bearing for a shaft. The shaft allows adjustment of the foot height (d) and angle (e).

chosen to align each leg's range of motion with the expected fiducial positions and to space the legs evenly about the circumference of the circular disc.

The design of our frame is conservative in the sense that its configuration space is larger than would be required to reach the ten trajectories in our clinical dataset. As more patient data become available, we can modify the slot and feet lengths to expand the range of our frame if necessary.

We designed the legs and circular disc to provide manual access to the microTargeting Drive System and its mounting hardware. No configuration of the legs obstructs access to the thumbscrews or

adjustment dials of the Drive System. The thin circular disc also provides a gap underneath the Freeze Frame for finger access to the incision site. The spaces between the legs provide several inches of lateral access to this gap.

The Freeze Frame prototype is constructed from Ultem 1000, a biocompatible and autoclavable thermoplastic (Sabic Innovative Plastics, Pittsfield, MA, USA). The vertical shafts are made of stainless steel. The coupling ring and gripper mechanisms are anodized aluminum. The total mass of the frame with the microTargeting Drive System attached is 0.83 kg.

3.3 Microstereotactic Frame Adjustment and Locking

To position the Freeze Frame, we sought a simple, compact, and reliable mechanism. Though all legs could be simultaneously positioned with independent robot mechanisms, such an arrangement is unnecessarily complex for our task. Instead, we use a three degree-of-freedom Cartesian robot to adjust each leg independently. Adjusting the legs separately imposes no significant time delay since only a few seconds are required for each leg. Since the adjustment robot requires only three motors, we believe it can be made as compact as a microwave oven.

Prior to adjustment, the Freeze Frame is mounted to two cylindrical pegs that fix the position and orientation of the circular disc during adjustment. A mounting peg mates with the mechanical coupling at the center of the Freeze Frame, fitting into the space occupied by base of the microTargeting Drive and fixing the origin and orientation of the trajectory. A second angular alignment peg fits into a notch on the circular disc to constrain the angle of the Freeze Frame about the trajectory.

At the beginning of the adjustment process, each leg gripper is unattached. Next, the leg that will be positioned to the shortest depth beneath the circular disc is fastened to an attachment post. The attachment post has a spherical top of the same diameter as the spherical fiducials implanted on the patient, and fits into the hemispherical cup at the bottom of a gripper mechanism. The gripping

mechanism is closed around the sphere, so that the cup is fixed on the sphere. The robot then translates the attachment post such that the vector from the trajectory origin on the circular plate to the attachment post matches the required vector computed in planning software. As this post is translated, the pieces that connect the cup to the circular disk slide relative to each other, allowing the cup to remain fixed while the attachment post translates. After this leg is permanently locked in the correct configuration by the introduction of a low-viscosity, fast-curing cyanoacrylate adhesive, which rapidly enters the spaces between the joints by capillary action and forms a very strong bond. The gripping mechanism is then released, and this procedure is continued for each additional leg in order of increasing height.

At present we require that the gripper mechanisms be manually fastened and released during the adjustment process, and that the adhesive be manually dispensed into each leg. These manual operations require less skill than needed for adjusting traditional stereotactic frames. However, we propose two additional features to fully automate these two operations in future designs, which are illustrated in Figure 3.5.

First, to automate the fastening and release of the gripper mechanisms, we will provide a motor-actuated clamp to press the attachment post into the hemispherical cup of a gripper mechanism. When the Freeze Frame is placed into the robot adjustment chamber, the upper end of each leg shaft will be inserted into an assigned hole on a plate that is rigidly connected to the mounting peg and angular alignment peg. A notch on each leg shaft and a corresponding feature in each hole will ensure that the shafts can be inserted at a specified angle in the correct hole, which will constrain the gripper mechanisms to known locations within the chamber. The robot can then be programmed to guide the attachment post to the hemispherical cup of each of the each gripper mechanism and then activate the clamping mechanism to initiate leg adjustment.

Second, to apply adhesive to the joints, the Freeze Frame will be delivered with a cyanoacrylate

dispensing unit attached to the top of each leg. Each dispensing unit will contain an ampoule of 2-octyl cyanoacrylate. The compound, 2-octyl cyanoacrylate is used clinically as a tissue adhesive (e.g., Dermabond) and also bonds mechanical parts with very high strength. After a leg has been adjusted to the required configuration, a solenoid in the dispensing unit will rupture the cyanoacrylate ampoule with a sharp pin. Cyanocrylate will flow through a filter to contain the ampoule debris, and then through multiple nozzles that are aimed at gaps between each leg's joints. Before the Freeze Frame is attached to a patient, the dispensing units will be removed from break-away mountings and discarded.

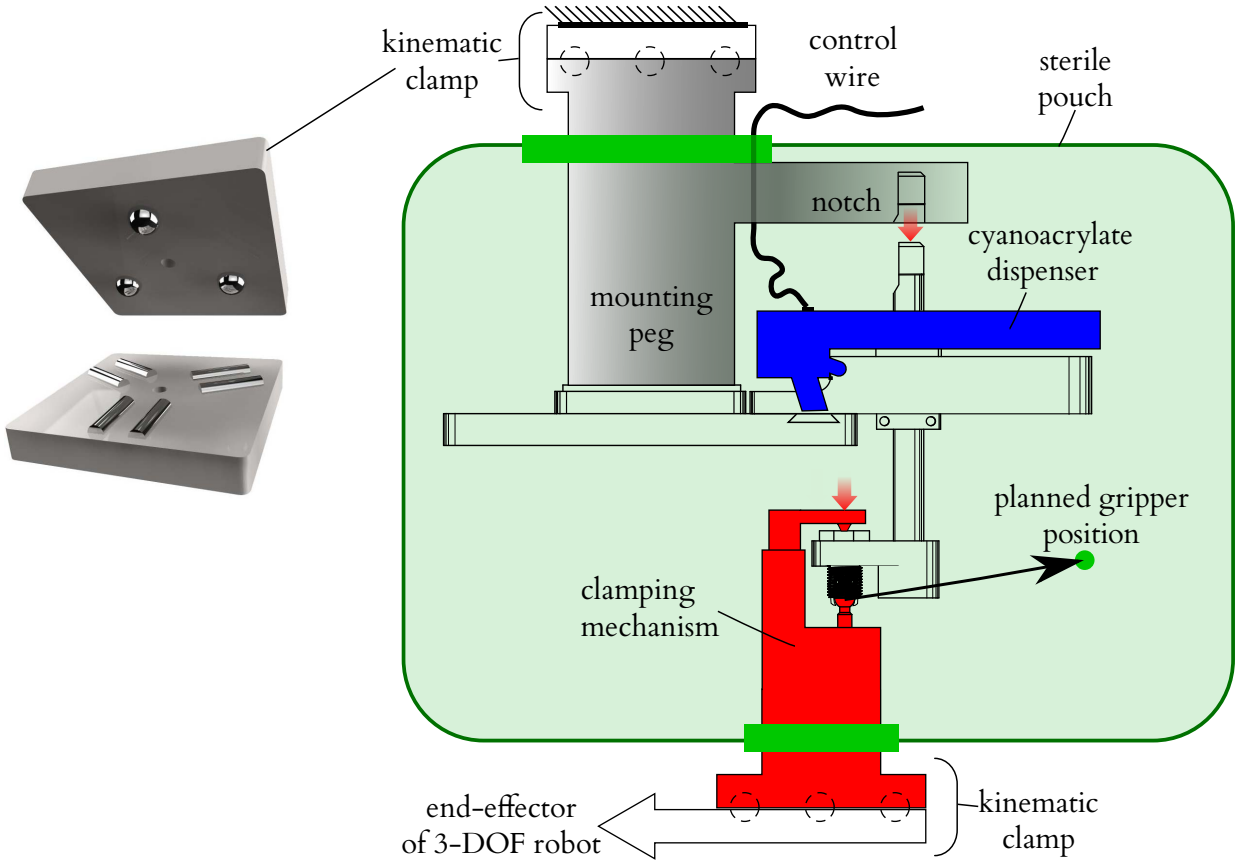

Figure 3.5: Schematic diagram of mechanisms proposed for fully automating the Freeze Frame adjustment process and avoiding post-adjustment sterilization.

The Freeze Frame can be sterilized after adjustment, during which it contacts a non-sterile robot. However, to expedite preparation of the frame, we propose delivering the Freeze Frame in a

sterile pouch with features that allow the frame to be adjusted by a non-sterile robot without opening the pouch until adjustment is complete. The pouch will contain the clamping mechanism and a mounting peg that mates with the ring on the Freeze Frame that supports the microTargeting drive system, shown in Figure 3.7(c). The clamping mechanism will be mounted on a metal arm that crosses the boundary of the pouch through a sealed polymer plate embedded in the flexible pouch material, where the non-sterile end of the arm will attach to the robot end effector. Similarly, the cylindrical pegs will be mounted on a second arm that will also cross a sealed polymer plate in the pouch to attach to a stationary point on the frame of the adjustment robot. To ensure that the circular disc and mounting post are at known positions within the robot workspace, the mating surfaces between the two arms and the robot will be kinematic couplings, which can provide positioning repeatability of less than one micrometer [54, 55].The two halves of a kinematic clamp can be held together by an electromagnetic clamp during adjustment. Electrical control wires for the clamping mechanism and the cyanoacrylate dispensing units will be routed through the sealed polymer plates.

3.4 Proposed Clinical Workflow

Our proposed workflow for DBS surgery will begin with a preoperative CT scan. A surgeon will manually select a target point and entry point in three orthogonal views. Prior to surgery, a pre-sterilized Freeze Frame will be attached to the robot in its sterile pouch.

Surgery will begin with implantation of titanium screw anchors at four locations on the top of the patient's skull. We will use FDA-approved anchors manufactured by FHC for the StarFix platform, and we will add custom extender rods with spherical tips that serve as fiducials [27]. The spherical fiducials will be localized in an intraoperative CT scan and used to register the preoperatively-planned trajectory to the intraoperative CT using the mutual information method.

Next, the registered targeting data will be transmitted to the robot, which will automatically

adjust and lock the Freeze Frame in the required configuration for guiding electrodes to the chosen target. The frame will then be removed from its fabrication chamber and securely attached to the spherical fiducials on the patient, where it will serve as a rigid guidance platform for the duration of surgery. After surgery, the frame will be discarded.

3.5 Methods

Our experimental dataset consists of fiducial and trajectory data from ten DBS surgeries performed at the Vanderbilt University Medical Center with the StarFix platform. The data was obtained using the WayPoint Planner Software as described in Section 3.2 above. The goal of our experiments was to measure the targeting accuracy of the Freeze Frame after adjustment for each of the ten patients in data set.

To adjust the Freeze Frame, we used an Exact Jr. 3-axis CNC milling machine (Broussard Enterprises, Inc., Santa Fe Springs, California, USA) with a Fagor 8040 M CNC controller (Fagor automation, Elk Grove Village, IL), i.e., a three degree of freedom Cartesian robot, to automatically adjust each leg. This CNC milling machine is considerably larger and more powerful than required to adjust our frame, but it can be accurately positioned to ± 0.005 mm. We attached a mounting peg and angular alignment peg to the head of the milling machine to fix the location of the Freeze Frame during adjustment, shown in Figure 3.6(b).

We embedded four attachment posts in an aluminum plate that was clamped to the mill vise, shown in Figure 3.6(a). Though our final design will require only one attachment post, we assigned a separate post to each leg to avoid a milling machine range of motion limitation introduced by the hardware that we attached to the CNC machine for these experiments.

Prior to all adjustment experiments, the locations of the cylindrical pegs and the spherical attachment posts were measured using a Faro GagePlus coordinate measuring machine (Faro Technolo-

gies Inc., Lake Mary, Florida, USA). To align the measurement coordinate frame axes with the milling machine translation axes, the Faro device was attached to a pedestal on the bed of the milling machine. The position of a conical divot mounted to the mill head was measured with the Faro after consecutive displacements along the three coordinate axes of the milling machine, allowing the Faro's measurement frame to be registered to the milling machine's axes of motion.

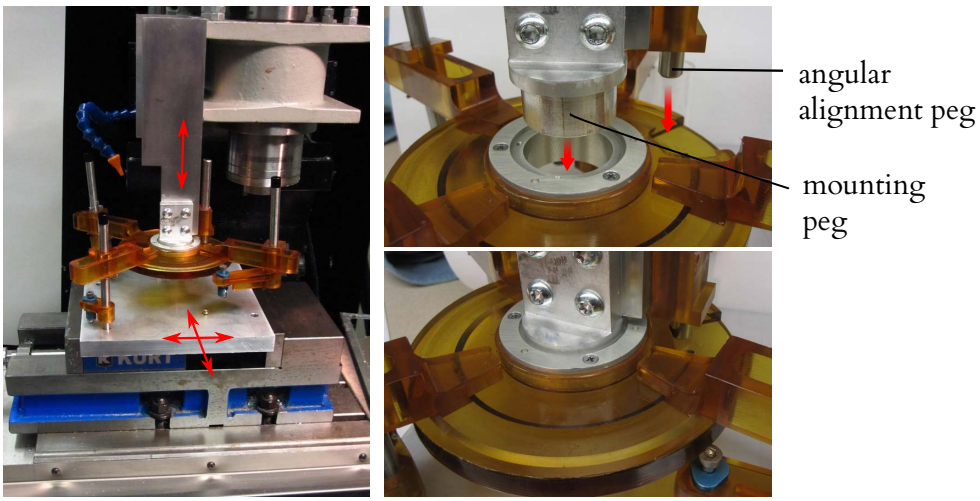

Figure 3.6: (a) The CNC milling machine used to adjust the Freeze Frame during experiments. The red arrows show the three degrees of freedom of this machine. Attachment posts are embedded in the plate below the Freeze Frame. (b) A cylindrical mounting peg mates with a coupling ring in the circular disc, and a second peg fits into a notch on the disc to constrain the angle of the Freeze Frame during adjustment.

To program the CNC milling machine, we wrote a custom Matlab program (Mathworks, Natick, MA) to automatically generate for each patient G-code (a programming language for CNC machinery) from the fiducial, target, and entry points obtained from patient CT scans, and from the peg and attachment post positions recorded with the Faro device. Beginning from a home position, the program computes the milling machine translations required to position an attachment post at the planned distance from the trajectory origin defined by the large mounting peg. For each patient, our program allows us to choose a trajectory length of 110 mm, 120 mm, or 130 mm to provide the shortest

distance to the target while maintaining adequate access space beneath the circular disc for the surgeon's fingers during the subsequent adjustment process. We selected from these three trajectory lengths because the same set of fixed lengths are used with the STarFix platform.

To lock the joints of the Freeze Frame, we applied an ethylene-vinyl acetate-based adhesive ("hot-melt" adhesive) as a substitute for a cyanoacrylate adhesive. Cyanoacrylate adhesives are ideal for permanent immobilization of the frame but are very difficult to fully remove. Removal of the adhesive will not be required in practice, because the frame will be discarded after each use, but for our experiments we reused one frame repeatedly. Though the ethylene-vinyl acetate adhesive provided considerably less strength and stiffness than a cyanoacrylate adhesive would have, the bonds were sufficient to hold the adjusted position of the frame for measurement.

After each frame adjustment, we removed the frame from the robot, fixed it into a vise, and employed the Faro to measure the centers of the hemispherical cups of the four gripper mechanisms and then rigidly registered these points to the corresponding planned positions. To find the trajectory vector of the adjusted Freeze Frame, we measured the interior cylindrical hole of the coupling ring and a reference surface on the ring using the Faro device. Measurements taken with the Faro are illustrated in Figure 3.7. The electrode insertion trajectory is aligned with the axis of the cylindrical hole with an origin at a fixed offset distance from the intersection of the cylindrical hole axis and the reference surface. Therefore, from the hole and the surface, we could determine the target point in the Faro's measurement space by extrapolation. The angle of the trajectory about its own axis is indicated by a reference divot on the coupling ring, which was also measured with the Faro device.

A rigid transformation was determined that placed the centers of the hemispherical cups as measured in Faro space onto the centers of the fiducial spheres as measured in CT space with least-squares error [56]. For each patient, we transformed the target position in the Faro measurement coordinate

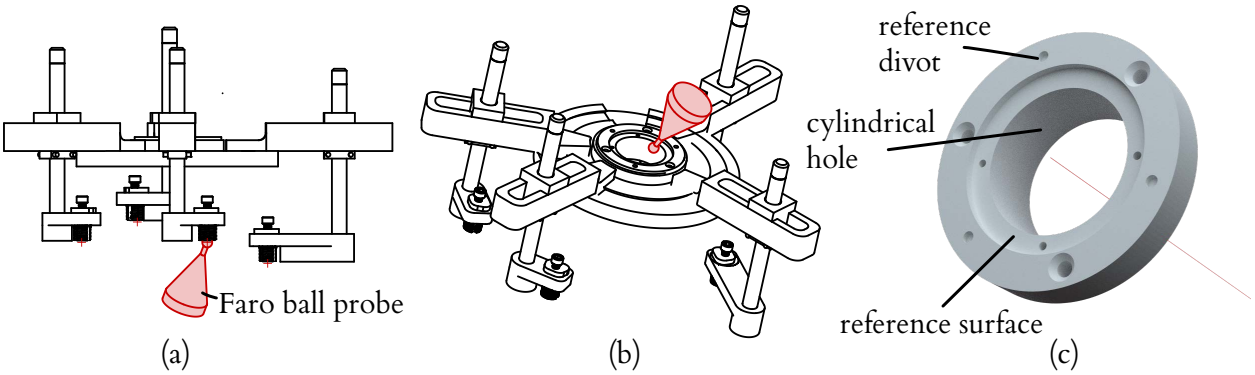

Figure 3.7: After the Freeze Frame was adjusted to a patient trajectory, a Faro portable coordinate measuring machine was used to measure features on the frame. (a) The four hemispherical cups of the fiducial gripper mechanisms were measured with a ball probe that was attached to the Faro. This probe was also used to measure features on the electrode driver coupling (b),(c). These features were used to find the position and orientation of the electrode trajectory.

frame to the corresponding space of planned points, and subtracted the planned target from the measured target to obtain the fabrication error at the target, e_t. The root mean square of e_t is calculated from the mean $\overline{e_t}$ and standard deviation σ_t of e_t:

$$RMS(e_t) = \sqrt{\overline{e_t}^2 + \sigma_t^2} \tag{3.1}$$

The target registration error (TRE) of the Freeze Frame depends on e_t and the fiducial localization error in image space. We estimate the root mean square value of fiducial localization error in image space, $\langle FLE_{image} \rangle$, to be 0.11 mm. This estimate was obtained from CT scans of a phantom embedded with the same spherical fiducials used with the Freeze Frame [57]. For the i^{th} patient, we calculated the expected TRE due to image localization error, $\langle TRE_{FLE}(i) \rangle$ from both the particular configuration of fiducials implanted on that patient and our estimate for $\langle FLE_{image} \rangle$ [58]. The mean squared value of

$\langle TRE_{FLE} \rangle$ for our dataset is given by the following:

$$\overline{\langle TRE_{FLE}^2 \rangle} = \frac{1}{10} \sum_{i=1}^{10} \langle TRE_{FLE}^2(i) \rangle \tag{3.2}$$

By adding Equations 3.1 and 3.2 in quadrature, we calculate the expected value of the root mean square TRE of the Freeze Frame using Equation 3.3:

$$\langle RMS(TRE) \rangle = \sqrt{RMS^2(e_t) + \overline{\langle TRE_{FLE}^2 \rangle}} \tag{3.3}$$

We obtained the fabrication error in the angle of the trajectory about its own axis (henceforth called the "angular fabrication error"), e_a, by transforming the measured position of the angular reference divot to the space of planned points and comparing it to the planned position of the divot. The mean and standard deviation of e_a are calculated using the directional versions of these statistics [59]. The accuracy of this angle determines the accuracy of adjustments made during the surgical procedure to the position of the electrode in response to changes in patient symptoms and side effects during stimulation. In particular, when adjustments are made in a direction perpendicular to the trajectory, an error in the angle will cause the actual adjustment to be different from the desired adjustment. Because of the limitations of the electrode driver, the maximum distance of adjustment perpendicular to the trajectory is 5 mm. The maximum error in electrode placement resulting from an adjustment of length r, when the angular error is $\Delta\theta$, is equal to $2r \sin(\Delta\theta/2)$ radians. As pointed out above, the maximum error in electrode placement is 2 mm. Inverting our expression for the maximum error for a given $\Delta\theta$, we find that the maximum acceptable angular registration error, e_a, is equal to $2 \sin^{-1}(2 \text{ mm}/(2 \times 5 \text{ mm}))$, which equals 0.4 radians or 23 degrees (we are omitting the contribution of the angular error resulting from fiducial localization error, because the error is approximately equal to FLE_{image} divided by the

mean distance between fiducials : 0.11 mm/123.6 mm = 0.0009 radians, which is about 0.05 degrees and is thus negligible.). We will consider e_a values that are at least one order of magnitude below 23 degrees to be acceptable.

3.6 Results

The results of the ten trials are summarized in Table 3.1. For all trials, the estimated target registration error were an order of magnitude lower than the maximum 2 mm error considered acceptable for DBS stimulation surgery. The angular fabrication error had a maximum absolute value of 0.08 degrees (1.42×10^{-3} radians), which is also much smaller than the maximum of 23 degrees that we consider to be acceptable.

Table 3.1: The estimated target registration error and angular fabrication error for all ten trials were within safe limits for DBS surgery. Maximum values are indicated by bold text. The patient numbers indicate to the order in which the trials were performed.

	Trajectory Length (mm)	Target Fabrication Error (mm)	Angular Fabrication Error (deg)	Estimated Target Registration Error (mm)
Patient 1	120	0.06	0.055	0.13
Patient 2	120	0.08	-0.034	0.13
Patient 3	120	0.15	0.009	0.18
Patient 4	110	0.12	**0.081**	0.16
Patient 5	120	0.09	-0.041	0.14
Patient 6	120	0.22	0.044	0.24
Patient 7	120	0.14	-0.034	0.17
Patient 8	110	0.14	-0.023	0.17
Patient 9	130	0.11	-0.018	0.15
Patient 10	130	**0.24**	-0.033	**0.26**
Root Mean Square		0.14	0.042	0.18
Mean		0.13	0.001	0.17
Standard Deviation		0.06	0.042	0.04

3.7 Conclusions

We have described a rapidly-adjustable microstereotactic frame for guiding intracranial targeting and a validation that provides sufficient targeting accuracy for DBS surgery. We have also introduced a method for analyzing clinical data to specify the design of this frame, and have demonstrated a method for adjusting a frame with six degrees of freedom using only a three degree of freedom robot.

Previously, we developed a model to predict the effects of external forces and torques on target registration error [57] and plan to apply this model to the Freeze Frame in our future work. We expect to find that that the small external forces and torques during surgery will contribute an insignificant amount to the target registration error.

In this study, we considered only DBS surgery, but we also plan to explore the suitability of the Freeze Frame for other stereotactic procedures, including biopsies, pallidotomies, thalamatomies, shunt placement, and otologic procedures.

CHAPTER 4

MEASUREMENT AND PERCEPTION OF TRAUMATIC FORCES IN COCHLEAR IMPLANTATION SURGERY

Tissue trauma is known to occur frequently in cochlear implantation (CI) surgery, but the relationship between force, trauma, and surgeon's perceptual capabilities is poorly understood. In this chapter, we consider translocation of cochlear implant electrodes from the scala tympani (ST) to the scala vestibuli (SV), which occurs frequently and may lead to suboptimal audiologic outcomes. Fresh (postmortem < 120 h), nonfixed, never-frozen human temporal bones were prepared by surgically isolating the cochleae and exposing the osseous spiral laminae, basilar membranes, and Reissner's membrane. Each isolated cochlea was mounted to a force sensor using a poseable mounting platform and punctured with a probe while concurrently recording forces and video. The mean force at rupture was 88 mN, and ranged from 42 mN to 122 mN.

The perceptibility of rupture or other forces during CI surgery has not been studied. We introduce a psychophysical testing procedure to estimate the threshold of perceptible force in CI surgery. Semmes-Weinstein Monfilaments (SWM) are a standard clinical tool for quantifying tactile sensation. We adapt these tools as a model of a grasped CI forceps, and use a two-alternative forced choice, staircase procedure to measure force perception of ten otolaryngological surgeons (six residents, four attending). We measure a mean threshold of 21 mN, which suggests that rupture forces are perceptible under some circumstances. The contents of sections 4–4.4 of this chapter were accepted for publication in *Otology & Neurotology*.

4.1 Introduction

Cochlear implantation (CI) is the standard of care for severe to profound sensorineural hearing loss. Rapid progress in technology, from its inception in 1957 to U.S. Food and Drug Administration approval in 1984 to current multichannel devices with modern processing techniques, has led to a dramatic increase in the number of patients who have benefitted from this technology [60]. Despite overwhelming success, CI is not without complications. Estimates of complication rates in the literature range from 4 percent to 40 percent [61]. One major subset of complications involves problems associated with CI electrode insertion. In unusual cases, insertion of the electrode is not feasible because of anatomic considerations. In most other instances, electrode insertion is not perceived to be difficult but damage to intracochlear structures inadvertently occurs, potentially resulting in suboptimal hearing outcomes for patients.

The surgical technique for CI is typically via a standard mastoidectomy with facial recess approach to the middle ear. This is followed by entering the cochlea, either via the round window or a separate cochleostomy, and inserting an electrode array. The goal is to insert the array into the scala tympani (ST) without damage to intracochlear structures. One major challenge is poor visualization. The surgeon is able to visualize the cochleostomy itself, but intracochlear structures, such as the osseous spiral lamina (OSL), Reissner's membrane (RM), and the basilar membrane (BM), are only partially visible via the cochleostomy, with the vast majority of the structure hidden by bone. The surgeon thus performs the critical step of the procedure blind to intracochlear anatomy and guided mainly by tactile feedback.

Translocation of the CI electrode array from the ST to the scala vestibuli (SV) with resultant intracochlear damage represents one cause of suboptimal hearing outcomes in patients undergoing CI. Multiple groups have documented poorer hearing outcomes should the electrode array cross from the

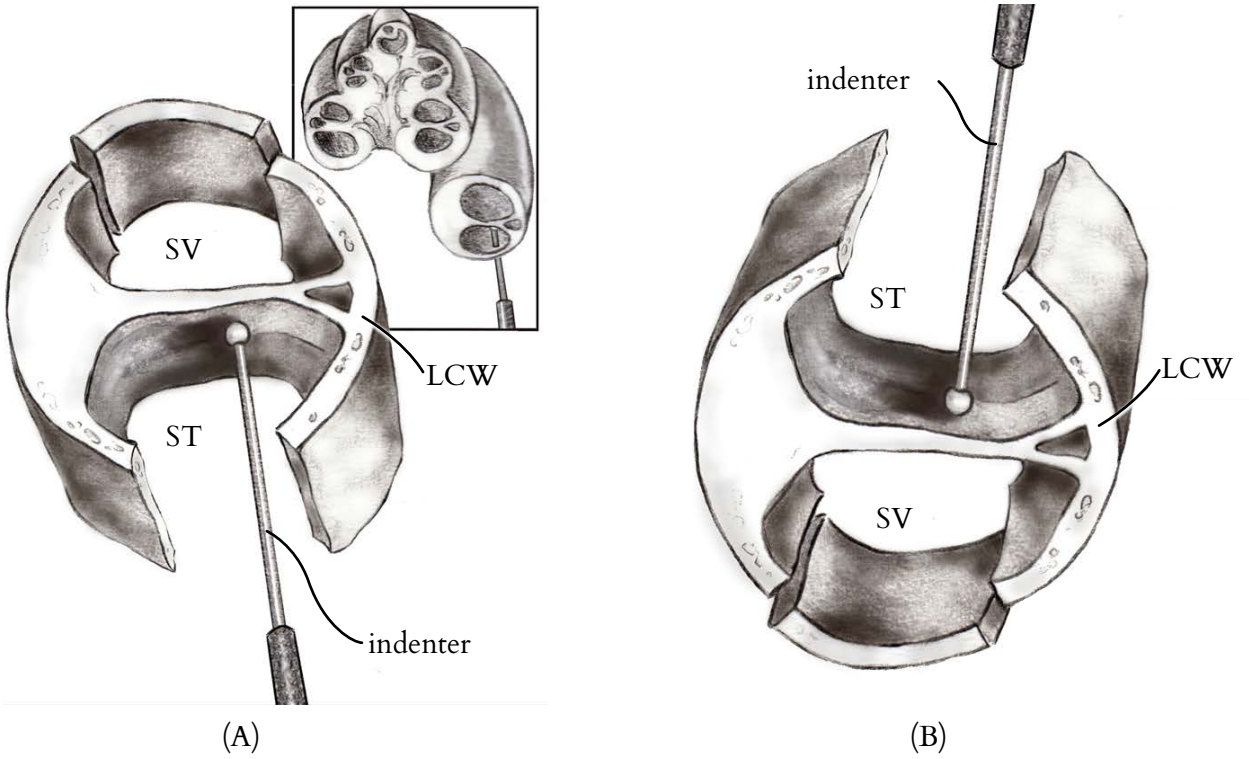

Figure 4.1: Cochlear schematic. (A) Cross-section of a right cochlea, with an indenter probe entering the scala tympani (ST) approximately 90 degrees along the basal turn. The schematic in the foreground shows the interscalar partition (black arrow) exposed from below (bone underlying ST has been drilled away) and above (removal of bone overlying the scala vestibuli [SV] is shown). LCW indicates lateral cochlear wall. (B) Orientation of cochlear specimen used during experimentation, which is upside down (flipped 180 degrees) from anatomic orientation, such that ST is above SV.

ST to the SV [62–65]. Although data exist comparing histopathologic changes of the cochlea with varying insertion depths of CI electrodes [66], there are limited data estimating the amount of force required for such translocation. The most relevant prior experimental results were reported by Ishii et al. [67], who used a blunt needle to puncture the round window (RW), BM, and RM, each of which was explanted from a single adult cochlea. The authors reported a BM rupture force of approximately 30 mN. The single RM tested had a rupture force of 4.2 mN. We propose to treat the OSL, BM, and RM as one entity because most clinical translocations completely traverse from the ST to the SV, often involving damage to all three structures. In doing so, we preserve the anatomic attachments of this group

of structures, which we refer to collectively as the interscalar partition, to both the lateral and medial cochlear walls, which we hypothesize provide significant structural support. In addition, we sought to develop a technique that could be used on multiple temporal bones to assess interspecimen variability.

In most circumstances, electrode insertion is not perceived by the surgeon to be difficult. However, the relative ease with which most electrode arrays are inserted does not guarantee that this portion of the procedure is carried out without undesired intracochlear trauma. In particular, damage to the cochlea can occur even in the absence of perceived difficulty with electrode insertion by the surgeon. This potentially results in suboptimal hearing outcomes for patients. In Section 4.5, we shift the focus of this chapter from the cochlea to the surgeon, and investigate the threshold of force perceptibility.

4.2 Materials and Methods

Twelve human temporal bones (six left, six right) were acquired from a tissue-harvesting service (Science Care, Phoenix, AZ, USA). The temporal bones were harvested immediately postmortem, stored in saline, and shipped cooled, but not frozen. All experimentation was carried out with bones no greater than 120 hours postmortem. Specimens were first prepared by isolating the cochlea without violating any intracochlear structures. This was achieved using the following dissection technique:

1. Perform a canal wall down mastoidectomy, including removal of the incus and malleus and sacrifice of the chorda tympani nerve.
2. Perform a labyrinthectomy.
3. Isolate the superior aspect of the cochlea by removing the horizontal (tympanic) segment of the facial nerve and all bone superior to it with a 4 mm cutting drill bit.
4. Isolate the anterior aspect of the cochlea by drilling into the carotid artery and removing all bone anterior to it.

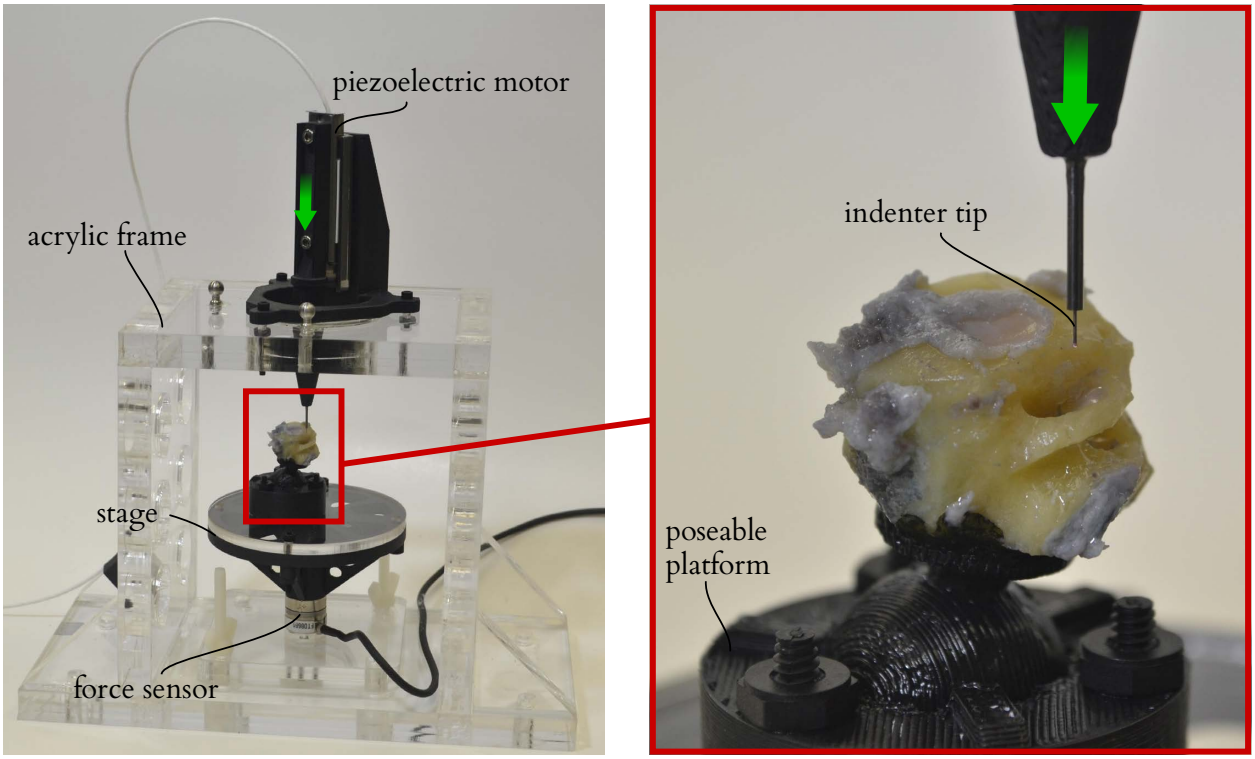

Figure 4.2: Experimental apparatus. (A) A sturdy acrylic frame supports a force sensor and piezolectric motor. The piezoelectric motor advances in the direction of the arrow to contact the specimen, which rests on a stage attached to the force sensor. (B) An enlarged view of the indenter, which is tipped with a 300 µm-diameter ruby sphere. The poseable mounting platform allows the specimen to be oriented such that the scala tympani is positioned just below the probe, with the basilar membrane, osseous spiral lamina, and Reissner's membrane approximately perpendicular to the insertion axis.

5. Isolate the cochlea from bone posterior to it by drilling away the pyramidal eminence, sinus tympani, and vertical (mastoid) segment of the facial nerve.

6. Using hypotympanic air cells as an inferior landmark, cut away all remaining temporal bone with a diamond band saw (Gryphon Corp, Sylmar, CA, USA), leaving an isolated cochlear specimen.

After the cochlea was isolated, a combination of microdissection instruments and 1 mm diamond drill bit were used to manually expose the interscalar partition in the area approximately 90 degrees along the basal turn of the cochlea. Care was taken to leave labyrinthine bone in place between the round

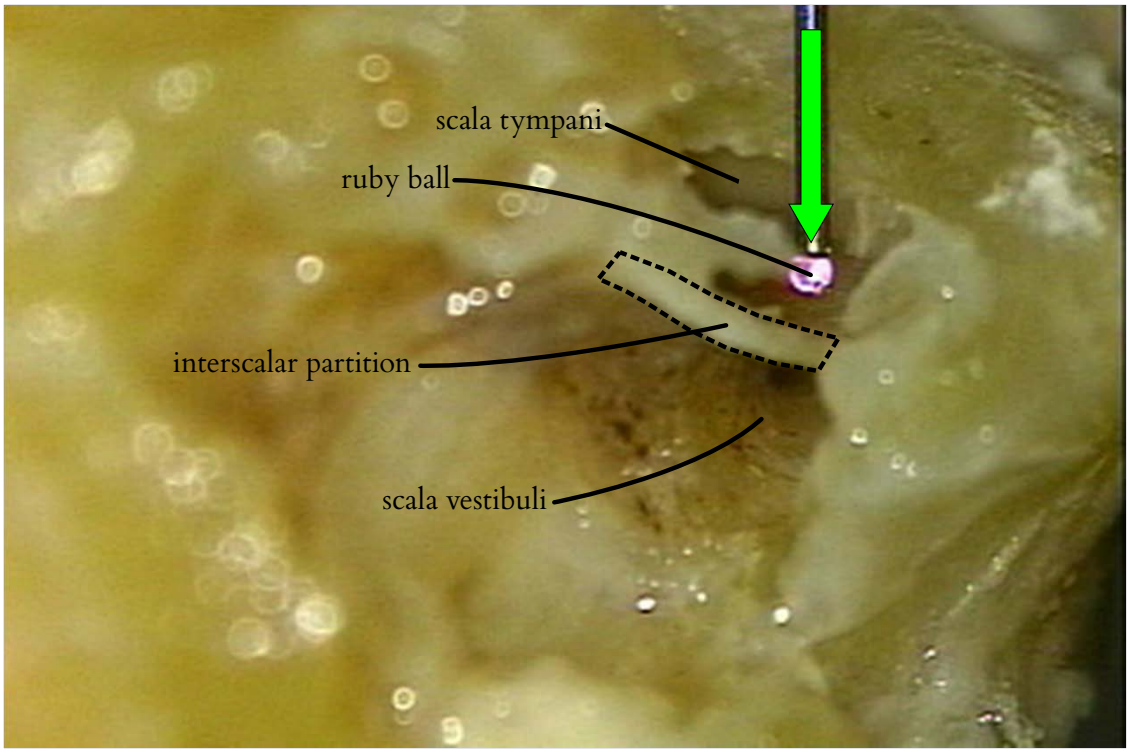

Figure 4.3: Orientation of experimental setup. Left cochlear specimen showing orientation of indenter to the interscalar partition before rupture. Bone between round and oval windows in this specimen has been removed to demonstrate the anatomy (pilot experiments, not included in data collection or analysis). The interscalar partition can be seen dividing the cochlear chambers into scala tympani above and scala vestibuli below. The indenter moves in the direction of the green arrow.

and oval windows as a supporting structure. In addition, bone was left in place at the lateral cochlear wall. Bone overlying the ST and the SV was removed under microscopy using a 1 mm diamond burr to expose the interscalar partition from above and below, as illustrated in Figure 4.1.

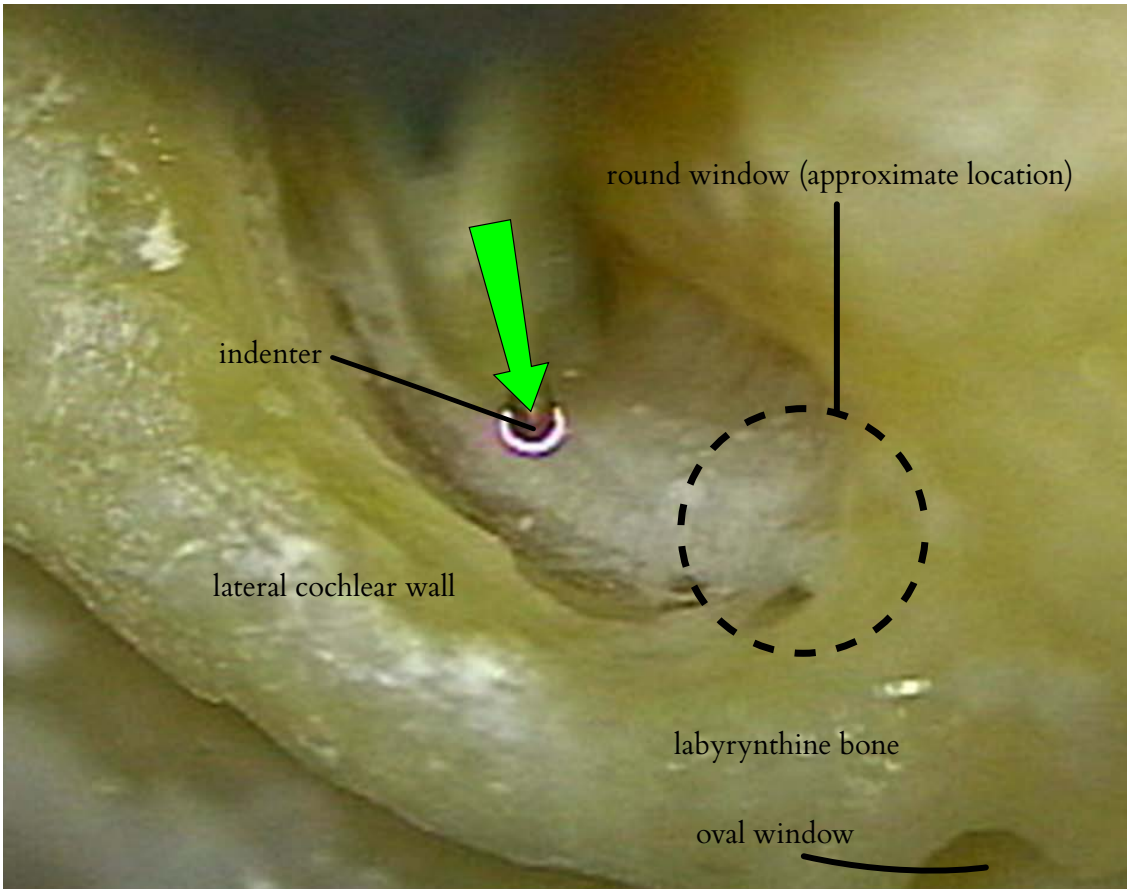

Figure 4.4: Right fresh human cochlear specimen before rupture, viewed from the scala tympani. The indenter is positioned directly above the interscalar partition, which is supported by native bony attachments. The dashed line indicates the approximate round window (RW) region before removing the RW niche and the RW membrane.

The experimental apparatus, shown in Figure 4.2, consisted of a custom-built, rigid acrylic frame. A Nano-17 force sensor (ATI Industrial Automation, Apex, NC, USA), was mounted to the base of the frame, and a small stage was attached to the force sensor to support cochlear specimens. The force sensor had a resolution of 1/320 N and was factory calibrated immediately before the experiments. Each specimen was fixed with epoxy to a custom-built poseable mounting platform, which was placed on the stage. The platform was adjusted such that the surface of the interscalar partition that faces the ST was approximately orthogonal to the insertion axis, and then the mounting platform was locked

by application of cyanoacrylate adhesive. In the experimental position, ST was immediately below the puncture probe and oriented above the SV. An SL-2060 piezoelectric linear motor with a displacement resolution of 1 μm (SmarAct GmbH, Oldenberg, Germany) was attached to the frame and was used to advance a rigid probe with a 300 μm diameter coordinate measurement machine ruby ball probe (itpstyli, St. Louis, MO, USA), which was aligned with a single axis of the force sensor. With the aid of an operating microscope (Carl Zeiss AG, Oberkochen, Germany), the specimen was manually positioned directly underneath the tip of the probe, such that they were oriented orthogonal to the insertion axis. The probe was advanced until it was approximately 200 μm from the tissue surface, as shown in Figures 4.3 and 4.4. The probe was then advanced at a velocity of 1 mm/s from the ST to the SV while concurrently recording force from the load cell and videomicroscopy of the rupture, as shown in Figure 4.5.

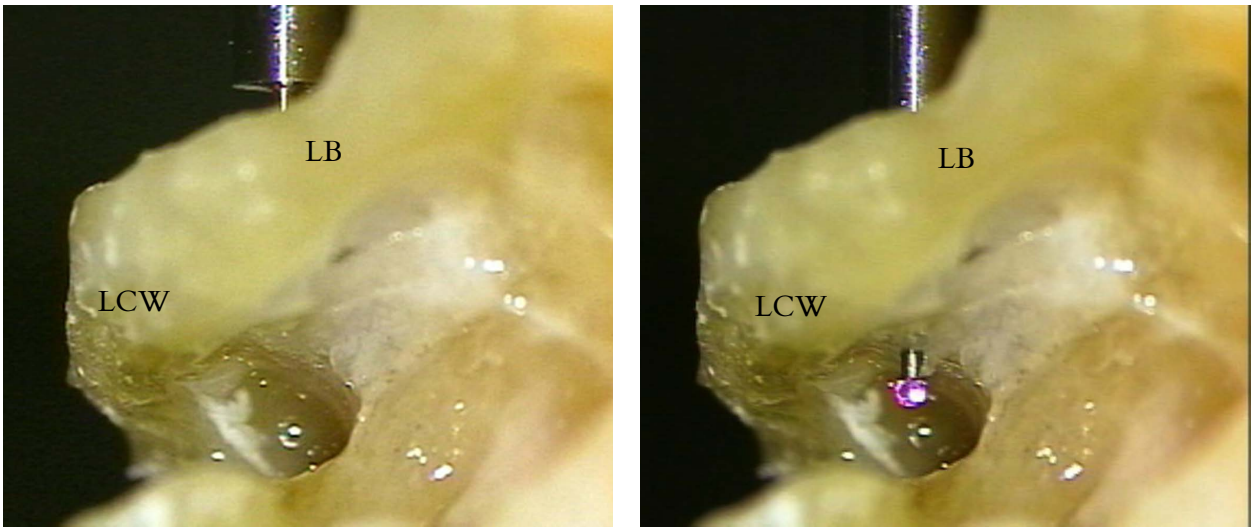

(A) (B)

Figure 4.5: Right fresh human interscalar partition before and after rupture, viewed from scala vestibuli. Prerupture (A) and postrupture (B) view of the specimen. The bony structural support can be seen on either side of the interscalar partition. LCW indicates lateral cochlear wall, and LB indicates labyrinthine bone between the round and oval windows. Note that the ruby ball punctures the interscalar partition without detaching it from the surrounding bone.

Custom software written in the C programming language was used to simultaneously control the motor and record data. The program was executed on a 2.66 GHz Intel Xeon processor running an Ubuntu 12.04 Linux operating system that was configured for real-time operation. The data were sampled at 5000 Hz and filtered using a fifth-order zero-phase Butterworth filter with a cutoff frequency of 25 Hz. The peak puncture forces were estimated by calculating the absolute maximum value in each filtered data set. In addition, each video was reviewed to determine the type of rupture that occurred. These were classified as either punctures or avulsions. A puncture was defined as the ruby ball penetrating from the ST to the SV without tissue detachment from the lateral or the medial support, whereas an avulsion was defined as a detachment from either the lateral or the medial bony attachments without puncturing.

4.3 Results

Twelve temporal bones were obtained and prepared. A total of ten bones were included in the final analysis. One of the excluded specimens was damaged during preparation and was not analyzed because of its lack of structural integrity at the time of testing. In the second excluded specimen, the probe was inadvertently advanced into the labyrinthine bone below the SV during experimentation, causing a very large spike in force measurements from which we were unable to isolate the rupture forces. Consequently, this specimen was excluded from the final analysis.

Force recordings for the ten analyzed bones are shown in Figure 4.6. Nine of the ten specimens demonstrated an approximately linear increase in force, followed by a rapid release of force noted immediately after puncture of an elastic surface. In one specimen, an avulsion from the medial wall occurred. The rupture forces ranged from a minimum of 42 mN to a maximum of 122 mN, with a mean of 88 mN and a sample standard deviation of 25 mN.

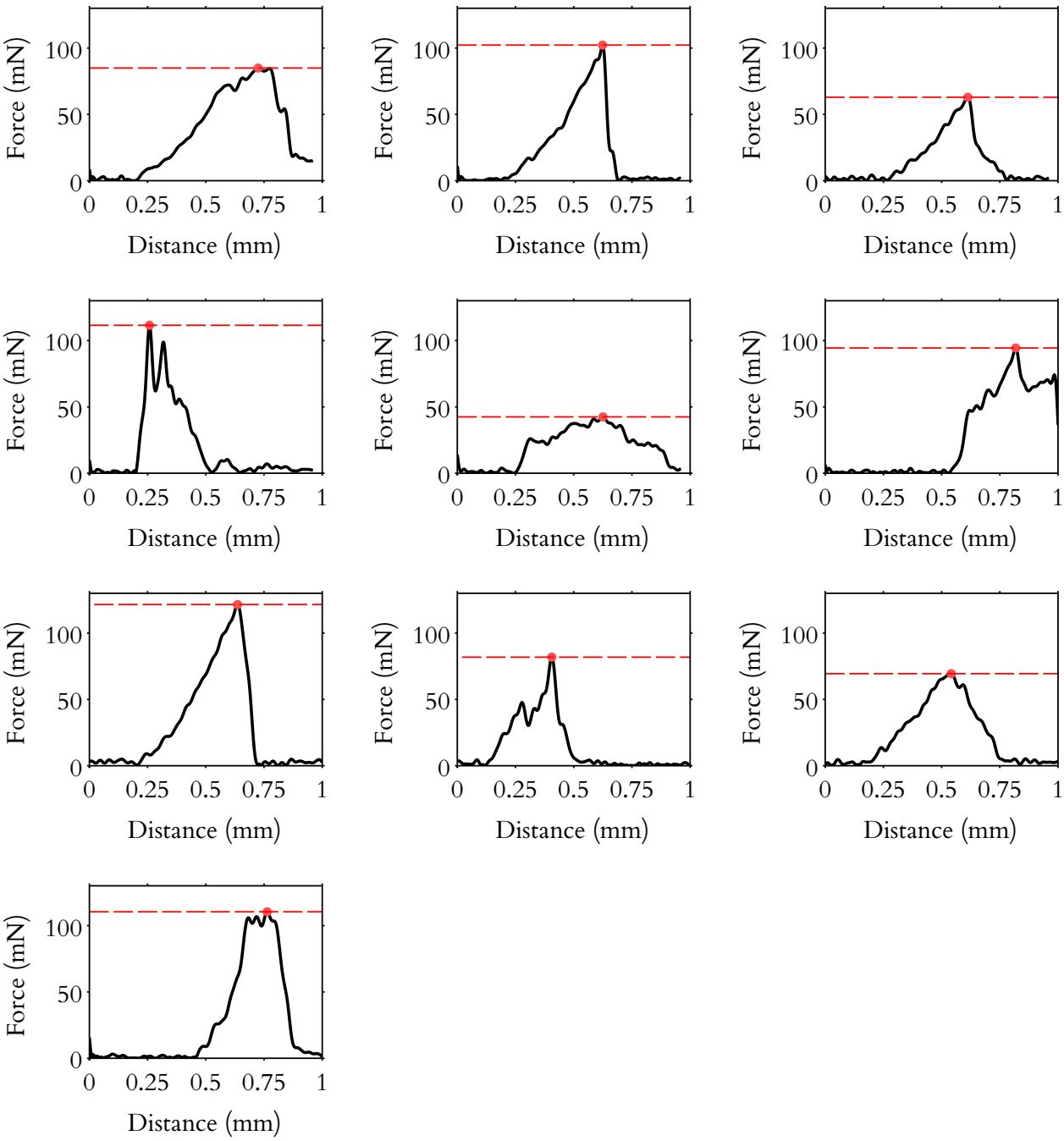

Figure 4.6: Forces recorded during translocation of test probe from scala tympani to scala vestibuli. Peak forces are identified by a dashed red line.

4.4 Discussion

Our measurements of the forces required to translocate a test probe from the ST to the SV have significant clinical implications regarding CI surgery. Our test probe results are comparable to translocation of electrode arrays. This represents perhaps the largest avoidable cause of failure to maintain residual hearing, which has been shown to impact audiologic outcomes even in patients with little to no serviceable preoperative hearing [68]. Before the work presented herein, there were few published results from which to estimate unsafe forces during CI electrode array insertion. This information is useful as systems and techniques for CI electrode array insertion are refined, including robotic systems that could be programmed to insert electrodes up to a given force level below which intracochlear trauma would be unlikely to occur.

To our knowledge, this is the first report of measured rupture forces associated with translocation from the ST to the SV in situ (i.e., tissues left attached to their native bony attachments). Whereas Ishii et al. [67] have previously performed experimentation to calculate the mechanical properties of isolated human BM tissue, these experiments evaluated a single fixed and explanted specimen, divided into three separate samples from different regions of the cochlea. This tissue lacked the in vivo support that would resist the forces applied by an electrode during CI surgery, as it was fixed and explanted. To overcome this limitation, we have developed a novel method of cochlear preparation in which the OSL, BM, and RM of the cochlea are exposed approximately 90 degrees along the basal turn while maintaining attachments to the medial and lateral cochlear walls. In addition, we performed the experiments on a larger sample size (n = 10). The mean rupture force was 88 mN, supporting our hypothesis that the OSL, BM, and RM complex, complete with native lateral and medial attachments, would have a larger rupture force than ex vivo BM as tested in the 1995 study [67].

The experimental setup was designed to replicate the conditions relevant to puncture of the interscalar partition. One aspect of this was the choice of the indenter used. The diameter of the ruby ball-tipped indenter was 300 μm, which is similar in size to that of a CI electrode array tip. In addition, its rounded shape eliminates the sharp edge used in prior work [67], which could cut tissue, potentially falsely reducing the forces necessary to rupture it. The hard spherical indenter also provides a well-defined contact condition for each trial. To mimic the in-vivo tissue as closely as possible, we used fresh, less than 120 hours postmortem, tissue that was not fixed and had never been frozen. In addition, we developed a method of exposing the OSL, BM, and RM complex approximately 90 degrees along the basal turn from both the ST and the SV without disrupting its native bony attachments, allowing us to closely simulate the clinical scenario of CI.

Although the work described here represents an important step in obtaining a better understanding of clinically relevant intracochlear trauma, more work is necessary to further characterize it. Our work investigated normal forces (i.e., those perpendicular to the interscalar partition) exclusively to faithfully replicate the rupture phenomenon and to characterize one fundamental type of loading. It is hypothesized that clinical damage often occurs when the electrode array is deflected off the walls of the ST in the basal turn, approximately 180 degrees from the insertion site, during which we believe normal forces predominate. However, over the full length of insertion, punctures may occur at various angles to the interscalar partition, and an understanding of the mechanisms of trauma may be improved by investigation of combined normal and tangential loading at different locations along the cochlea in the future.

As CI surgical techniques continue to improve, automated electrode insertion may hold the potential to minimize trauma by inserting at a slow regulated velocity and stopping or altering the insertion trajectory when real-time force feedback indicates forces high enough to cause trauma, for

example, translocation from the ST to the SV. Our group has studied robotic insertion and has shown that electrodes inserted robotically have significantly less variation in force than those inserted by human operators [69]. Furthermore, preliminary data on electrode insertion forces generated during robotic insertion demonstrate significant differences between standard insertion techniques and those guided by stylets to avoid collision with the cochlear walls [70]. Before the work described herein, the clinical significance of these findings was speculative at best. We conclude that minimizing insertion forces will reduce the risk of translocation of a CI electrode array and lead to improved audiologic outcomes. Our data suggest that an average of $88\,\mathrm{mN}$ is required for such translocation to occur, but they can occur with forces as low as $42\,\mathrm{mN}$. This leads to perhaps the most perplexing question generated by these data can human surgeons perceive such forces? This question will be addressed in the following section.

4.5 Measurement of surgeon force perception thresholds in cochlear implantation

Insertion forces are not recorded during cochlear implantation surgery. Rather, they may or may not be *perceived* by a surgeon, who alone decides whether or not corrective action should be taken to avoid damaging the cochlea. To date, no study has investigated surgeons' ability to perceive insertion forces during CI surgery. There is a fundamental difficulty in measuring perceptual thresholds: they relate to mental states which cannot be directly observed. In this section, we adapt methods from the field of psychophysics to the problem of measuring surgeons' tactile thresholds.

Psychophysics studies the relationship between stimuli and the perceptibility of those stimuli [71, 72]. The study of perceptual thresholds began with the work of Fechner and Weber in the 19^{th} century [73], and has evolved into the testing procedures that are routinely used in audiometry and optometry, for example.

In modern psychophysics, perception is viewed as a probabilistic process in which the ability to perceive a fixed stimulus intensity varies with repeated application of the stimulus. Perception is

understood to occur in the presence of noise, including both external noise and the intrinsic noise of the sensory system. As the intensity of a stimulus increases, the signal to noise ratio increases, and the probability of correctly identifying the stimulus gradually increases according to a relationship described by a *psychometric function*. Psychometric functions vary in shape according to the sensory modality and nature of the stimulus. A typical psychometric function in illustrated in Figure 4.7 with contrived data. A threshold can be chosen as a stimulus intensity (on the abscissa) corresponding to a certain percent correct level on the curve, such as the level at which 50 percent of the stimuli are correctly identified. Thus, a threshold is not a sudden step change from "not perceivable" to "fully perceivable", but is rather a quantity derived from the psychometric function.

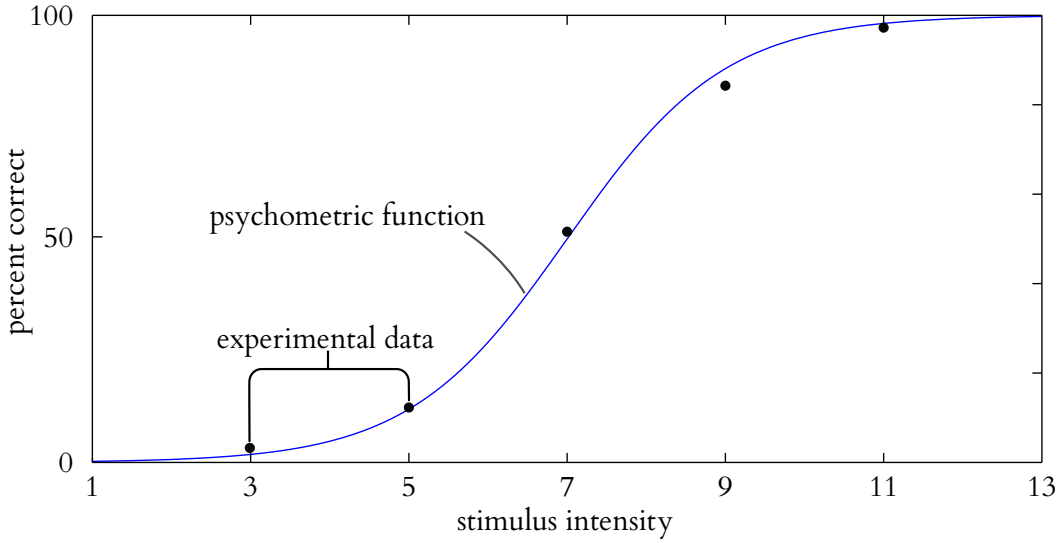

Figure 4.7: A psychometric function relates the intensity of stimuli to performance at a psychophysical task. The function can be estimated by fitting a curve to percent correct data at multiple stimuli level, but estimation of a single threshold stimulus is more efficiently estimated by an adaptive method. In the contrived example shown here, the 50 percent threshold corresponds to a stimulus intensity of 7.

A psychometric function can be approximated by fitting a curve to response data measured over a range of stimulus levels, but this approach requires a large number of trials and is inefficient and tedious if only a threshold value is desired. An alternative is to use one of several adaptive testing

procedures, which adjust stimulus intensities according to correct or incorrect responses in order to efficiently target the data needed for computation of a threshold. In this study, we will use a staircase adaptive procedure [74, 75]. Staircase trials begin with a large, easily perceivable stimulus intensity, which is reduced by fixed increments until a participant responds incorrectly. Following the incorrect response, the stimulus intensity is increased by graduated increments until the participant response correctly, at which point the direction of increment is again reversed. The threshold is estimated by averaging the reversal points. Often, an "n-down-1-up" rule is used in which n successive correct responses are required before the stimulus can be decreased. The convergence properties of staircase procedures depends on the stimulus intensities, step sizes, number of trials and other factors, and are rigorously examined by Garcia-Perez [76]. Generally, adaptive procedures do not target the 50 percent level on the psychometric curve. The three-down, one-up design that we will use in this study converges on the 79.4 percent correct level [77], for example.

Results from psychophysical experiments are prone to errors caused by several cognitive biases. For example, participants may affirm the presence of a stimulus even when it is absent or below the actual threshold from a desire to perform well. This bias is of particular concern in the present study, because success at the experimental task may be interpreted as an indicator of occupational skill. A standard method to eliminate bias in psychometric trials is the two-alternative forced choice (2AFC) method. Rather than replying "yes" or "no", a participant is forced to choose between randomly assigned noise and stimulus alternatives.

There is a large body of psychophysical research relating to the hand and fingertips [78, 79], but few studies have examined absolute force perception thresholds under conditions comparable to CI insertion. Force thresholds have been measured in the context of diabetic neuropathy testing [80, 81], but the point forces applied in neuropathy testing do not resemble the distribution of pressure across

a surgeon's gloved palm and fingertips. Loads distributed across one or more fingertips have been tested by developers of haptic devices. Dosher and Hannaford used a forced-choice, adaptive testing protocol to measure forces applied to the fingertip with a haptic device [82], and reported average detection thresholds ranging from 30.1 mN to 50.4 mN. Using a similar pyschophysical testing protocol, King, Donlin, and Hannaford [83] applied forces to multiple combinations of fingertips, and reported a threshold range of 27.8 mN to 34.0 mN. Baud-Bovy and Gatti transmitted force via a robot end effector to a spherical handle grasped by a subject, and reported a minimum threshold of 49 mN when subjects were allowed to move the handle to seek the direction of the force [84]. These studies advance our understanding of the hand's sensitivity, but the configurations of these devices did not resemble the grasp and motion used in CI surgery.

In this study, we will test the force perception thresholds of a group of surgeons using equipment designed to replicate the arm posture and forceps grasp used in CI surgery, using an adaptive staircase psychophysical testing procedure.

4.5.1 Methods

Twelve participants were recruited via email, phone, and personal communications. Inclusion criteria stipulated that all research participants must be otolaryngologists who actively perform CI surgery in their clinical practice, or otolaryngology residents at a residency training program approved by the Accreditation Council for Graduate Medical Education (ACGME). Postgraduate year 1 (PGY-1) residents were excluded, as they have little to no training or experience in otologic surgery at this stage of residency. Six participants were current residents or fellows at the time of testing, and four had completed training and were practicing surgeons. Additional demographic information is shown in Table 4.5.1. All participants signed informed consent after reviewing the risks and benefits of participation. This study was approved by the Vanderbilt University Institutional Review Board.

	Resident/Fellow	Attending
Gender		
Male	6	4
Female	0	0
Average Age (years)	29.67	55.0
Fellowship Training Completed		
Otology/Neurotology	n/a	3
Pediatrics	n/a	1
Performs CI in Clinical Practice	n/a	4
Mean Number of CI Surgeries per Month	n/a	5.25
Handedness		
Right	6	4
Left	0	0

Table 4.1: Demographics of participants included in analysis of force perception thresholds.

To apply forces reliably and with known intensities, we used Semmes-Weinstein Monofilaments (SWM). These devices consist of a handle with a nylon monofilament tip that is calibrated to buckle at a particular force. SWMs are a standard clinical tool for cutaneous sensory function, and are used regularly to evaluate diabetic peripheral neuropathy. They are recommended by the World Health Organization as devices that can be used by health professionals for repeatable testing and measuring of the threshold of cutaneous sensory perception [85], and their mechanical reliability has been rigorously evaluated [86].

In clinical usage, a physician grasps the SWM handle and presses the filament tip into a patient's skin until the filament buckles. To replicate electrode insertion in our experiments, participants held an SWM handle between the thumb and index finger to model the grasp of CI forceps. By buckling the filament, the calibrated force was applied to participants' hands in a way that resembles the transmission of force through CI forceps (we shall describe how the filaments were buckled shortly).

SWM filaments are manufactured in a standard set of buckling strengths. These buckling strengths increase on an approximately logarithmic scale [87]. A logarithmic scale is used because the perceived intensity is approximately linear with logarithmic increase of force. We selected a set of eight

SWM force intensities, listed in Table 4.2, to span the estimated perceptual range of participants.

Table 4.2: Semmes-Weinstein monofilaments were selected from the standard clinical set to span the expected range for the force threshold during CI surgery.

Force (g)	Force (mN)
0.4	3.9
0.6	5.9
1	9.8
1.4	13.7
2	19.6
4	39.2
6	58.8
8	78.5
10	98.1
15	147.1

We constructed a fixture, shown in Figure 4.8, to cause SWM filaments to buckle reliably over multiple trials and to reduce variability in the motion of the SWM handles among participants. In the intended clinical use of SWMs, a physician moves the handle and visualizes buckling of the filament as it is pressed into a patient's skin. The SWM is shielded from participants' view in our experiments, so the fixture constrains the handle to move between two fixed endpoints. Before commencing a trial, the SWM handle is placed in a starting fixture, shown in Figure 4.8(a), that suspends the filament tip above a target surface. The distance between the starting fixture and the target surface is fixed, but the mutual height of these components above the tabletop is adjustable. The experimenter adjusts this height, as shown in Figure 4.8(b), such that the SWM handle is approximately parallel to the tabletop when held in the starting fixture. Without a means to adjust the height of the starting fixture, the SWM handle would be initially inclined with respect to the target surface at an angle that is propotional to a participant's palm width. Such initial angulation of the handle is undesirable as it biases the filament to contact the target surface at a steep angle and possibly skid or bend rather than buckle. To commence a trial, the experimenter pulls a handle to release the SWM handle from the starting fixture, as shown

in Figure 4.8(c). The participant then lowers the handle until it contacts a stopping plate, in which position the filament is buckled, as shown in Figure 4.8(d). The height of the stopping plate was chosen to be slightly shorter than the average filament length amongst the SWM devices tested in order to stop advancement just after buckling, preventing extreme bending or slippage of the filament on the target surface.

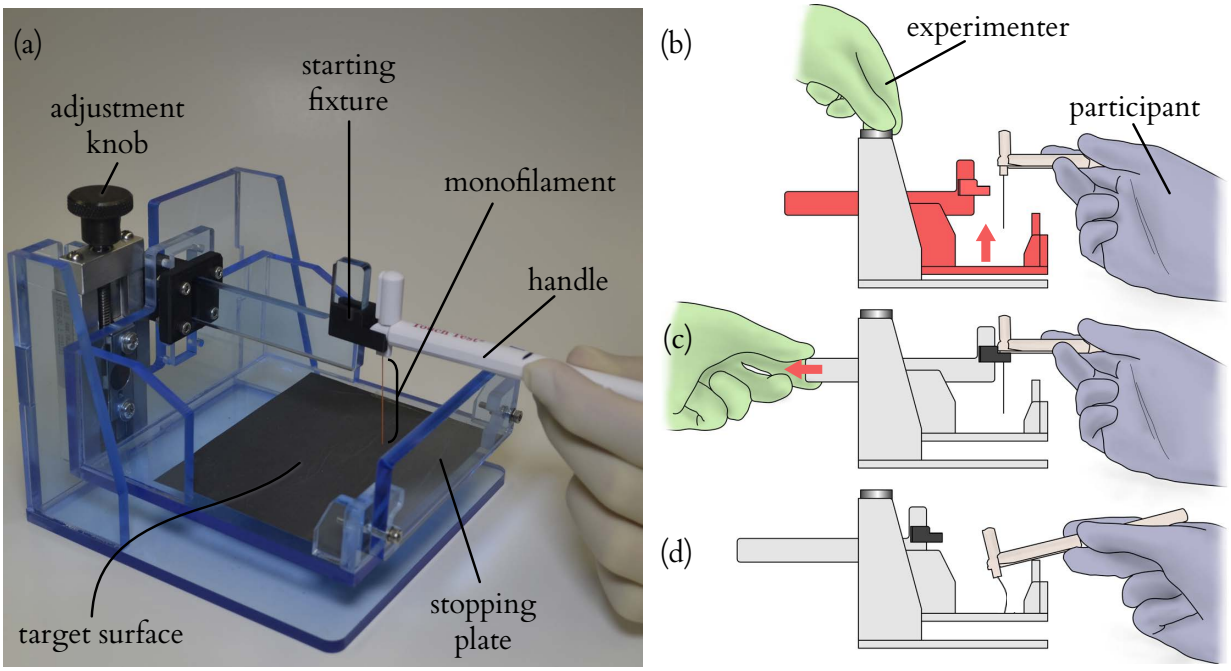

Figure 4.8: (a) A custom-built testing device used to model the advancement of forceps and transmission of electrode-basilar membrane contact forces during cochlear implantation surgery. In each trial, a participant lowers a Semmes-Weinstein Monofilament (SWM) handle from the starting fixture until it contacts the stopping plate. If a monofilament is attached to the SWM handle (control trials omit the monofilament), the monofilament will buckle against the target surface when the handle contacts the stopping plate, causing a calibrated force to be applied to the participant's hand. (b) Before testing, the device is adjusted to the height of each participants' hand, such that the initial orientation of the SWM handle is approximately parallel to the tabletop (c). To begin each trial, the experimenter places the SWM handle in the starting fixture, which is at a fixed height above the stopping plate and target surface. The experimenter then retracts the starting fixture and instructs the participant to lower the SWM handle. (d) The handle rests on the stopping plate at the end of each trial.

Tracey, Greene, and Doty performed experiments to evaluate the test-retest reliability of

two alternative forced-choice (2AFC) staircase procedures for SWM testing of tactile thresholds, and recommended a three-down, one-up (3D1U) rule for reversals [88]. The authors found that a test-retest reliability coefficient greater than 0.80 could be achieved with as few as two reversal pairs. Encouraged by these results, we adapt the 2AFC-3D1U psychophysical testing procedure recommended by Tracey et al. for our model of CI surgery.

Participants were seated behind an opaque curtain, shown in Figure 4.9, to prevent observation of the testing apparatus and of the experimenter. Each participant donned an appropriately sized surgical glove on the dominant hand and passed this hand through a slit in the curtain, which was covered by an additional flap of fabric to prevent observation through the slit.

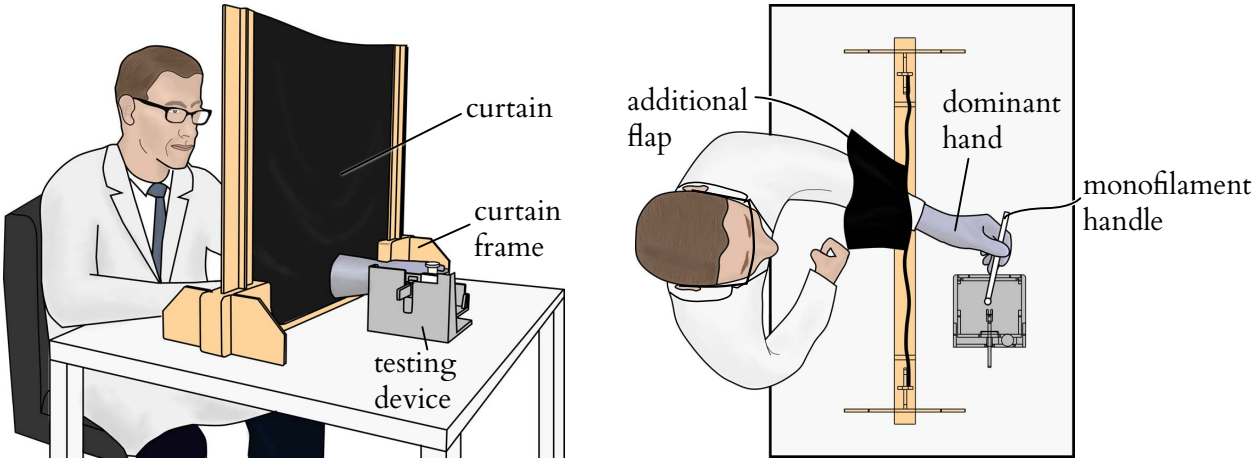

Figure 4.9: (a) An opaque curtain is placed between participants and the testing device to prevent visual observation of the experimental apparatus and experimenter during trials. The curtain ensures that participants experience only tactile feedback by avoiding visualization of either Semmes-Weinstein monofilament (SWM) buckling during experimental trials, and also obstructs visual observation of SWM handles without attached monofilaments during control trials. (b) A top view of a seated participant. The participants' dominant hand is inserted through a hole in the curtain, which is covered with an additional flap of curtain fabric to prevent visualization through the opening in the main curtain. The experimenter (not shown) sits opposite to the participant. The curtain prevents the participant from visually observing the experimenter, who reads instructions to the participants from a prepared script.

Before commencing trials, each participant was read instructions from a prepared script which

is included in the Appendix to this chapter. To implement paired 2AFC trials, one SWM device was modified by removing the filament entirely (a negative control). Each trial consisted of a pair of handles, one with a standard SWM and the other with the modified control handle, in a random order. The experimenter placed a SWM handle (either a filament or the negative control) in a participant's hand, and then guided the handle to rest in the starting fixture. Next, the experimenter retracted the starting fixture and read a scripted notice to the participant to begin lowering the SWM handle. The participant was then instructed to advance the SWM handle straight downward at a speed that he would normally use to insert a CI electrode array, until the SWM handle contacted the stopping plate. This sequence was then repeated with the second half of the pair (either a filament, or the negative control). Following a 2AFC trial, participants were instructed to report which device (the first or the second) contained the filament.

We implemented a 3D1U staircase testing procedure beginning with a filament buckling strength of $39.2\,\mathrm{mN}$ which we believed would be 100 percent perceivable by all participants. After three consecutive correct 2AFC trials, the filament strength was decreased by one increment in the series of filaments. Conversely, an incorrect response, implying an inability to perceive the present force, led to an increase in filament strength in the subsequent trial. All participants completed a total of 25 pair of filaments. A force perception threshold for each surgeon using the arithmetic mean of the log-transformed stimulus intensity values (thresholds are calculated in units in which the steps are constant [76]). We show one staircase plot in Figure 4.10.

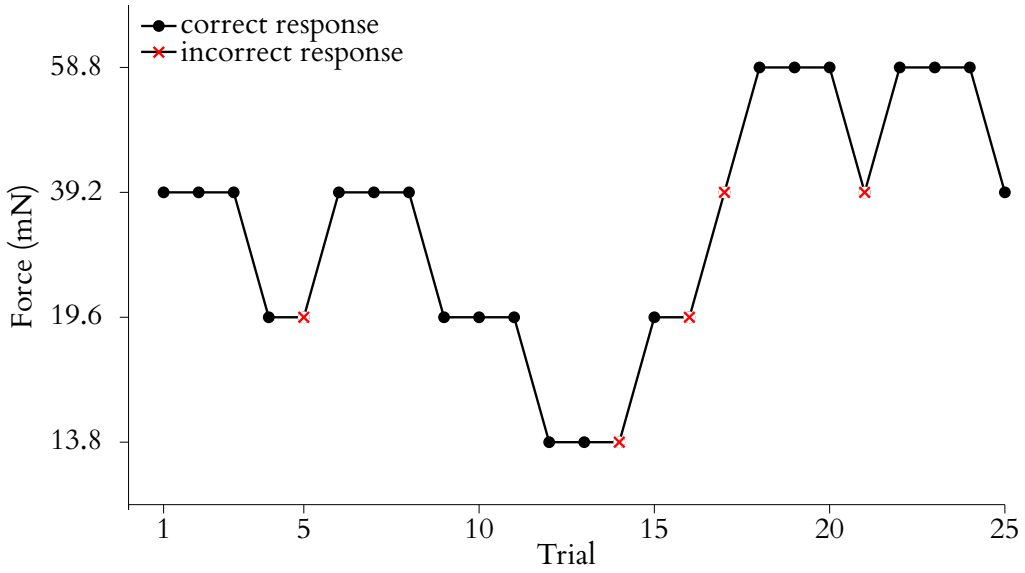

Figure 4.10: A plot generated from the responses of a single participant demonstrating correct (black) and incorrect (red) responses, and the resulting staircase. Three correct responses were required before decreasing the stimulus intensity. This plot shows three reversal pairs consisting of six reversal points. A reversal point is defined as a change in direction of the plot.

4.5.2 Results

All twelve participants completed testing, but two participants were excluded from the final analysis because their performance exceeded the range of SWM filaments given in Table 4.2 during staircase testing. One participant exceeded the maximum strength filament in our set, and the other exceeded the weakest filament. Thus, we were not able to compute thresholds for these two individuals. Threshold statistics for the remaining ten participants are summarized in Table 4.3.

Table 4.3: Force perception threshold statistics from ten otolaryngological surgeons.

	Resident/Fellow (n=6)	**Attending (n=4)**	**All (n=10)**
Mean (mN)	18.8	25.9	21.4
Median (mN)	20.4	26.6	22.3
Min (mN)	10.8	17.4	10.8
Max (mN)	33.6	36.4	36.4

4.5.3 Discussion

An understanding of force perception thresholds is essential for further development of CI techniques and devices. This study adapts well-established force threshold testing methods from the psychophysics literature to the particular physical environment of CI surgery. To date, no study has experimentally measured force perception thresholds using such a model of cochlear implantation. Force perception thresholds have been considered for other surgical tasks [89], but to our knowledge, the present study is the first to examine surgeon's force perception thresholds using a forced-choice, adaptive testing procedure.

Our model sacrificed some fidelity to the clinical environment of CI surgery in order to standardize the test environment and to control the magnitudes of the applied forces. Forces vary continuously during actual CI surgery, depend on the speed of insertion, and vary from surgery to surgery. Applying a time-dependent force would require several assumptions about the speed of insertion and shape of a representative curve. Furthermore, reliable haptic rendering of the small forces needed for threshold testing is a non-trivial task that requires specialized equipment [90]. Instead, the SWM devices we used applied an abrupt change in force magnitude. Rapidly changing forces may be easier to perceive than gradually rising forces [79], so our model represents a somewhat idealized, limiting case of rapid force onset.

Recently, force sensors have been used to continuously measure insertion forces in both cochlear phantoms and cadavers [34]. An alternative approach to measuring thresholds might record forces while performing an insertion with a standard clinical electrode, and rely on the tested surgeon to raise a signal at the first perceivable force. By comparing force recordings to the time index of the force recording, a threshold could, in principle, be established. However, the surgeon's signal would be delayed by a

variable reaction time delay of approximately 100-200 ms, making it difficult to distinguish the perceived force from adjacent values on a rapidly fluctuating recording of forces. Furthermore, this design would be susceptible to the false positives that our 2AFC design guards against.

The challenges involved in measuring forces with a clinical electrode and cadaveric specimen are perhaps surmountable. Our study provides a simple, easily replicable experimental model that could be used to enlarge the available data while more elaborate testing methods are developed.

4.6 Conclusion

The reduction of electrode insertion forces has been a recurrent goal in the development of CI surgery. Consideration of insertion forces has guided the design of electrodes, influenced surgical techniques, and spurred recent development of robotic tools for CI surgery. However, the effects of insertion forces on intracochlear tissue and the surgeon's experience of these forces have been neglected by researchers. We provided the first data on intracochlear puncture forces in fresh tissue, and the first measurements surgeons' ability to detect the small forces that occur during CI surgery.

We reported a minimum puncture force of 42 mN, which is larger than the maximum force perception threshold of 36.4 mN we measured among a group of surgeons. Our results suggest that surgeons can detect translocation of an electrode from the ST to the SV. However, during CI insertion, the force transmitted through the electrode and forceps is believed to have several causes, with frictional contact with the walls of the scala tympani predominating. The force required to cause puncture or other severe damage to the basilar membrane may be transmitted to the surgeon in addition to a range of forces of a relatively benign origin, i.e., it may be masked by noise, especially where the puncture occurs deep within the cochlea, where parts of the electrode are likely to be in contact with the walls of the scala tympani when the trauma occurs. Further work is needed to resolve the multiple causes of the total force transmitted to the surgeon's hand, and to relate these forces to trauma.

CHAPTER 5

GUIDING ELASTIC RODS WITH A PERMANENT MAGNET FOR MEDICAL APPLICATIONS

A magnetic field can be applied through a patient's body to steer a magnet-tipped rod such as a catheter, needle, or electrode array. Magnet-tipped rods can be made very thin because they are deflected without pull wires or other bulky internal mechanisms. Such rods could be beneficial for a range of medical procedures, but the magnetic field sources in current clinical use are large and expensive. Here, we describe use of a robot-manipulated permanent magnet to guide the tip of a rod. We solve for rod deflections by combining permanent-magnet models with a Kirchhoff elastic rod model, and use a resolved-rate approach to compute trajectories. Experiments demonstrate that three-dimensional trajectories can be executed accurately in an open-loop configuration, and that the system's redundancy can be exploited to avoid obstacles. The manuscript of this chapter has been submitted to the journal *IEEE Transactions on Robotics*.

5.1 Introduction

Catheters, needles, and other rod-shaped surgical instruments enable deep access to the interior of the body without invasive surgical exposure. Forcefully manipulating the exposed end of a rod may provide limited control over the tip, but fine control is often desirable to reach small targets, steer around sensitive tissues, or to perform more dexterous tasks. A range of mechanisms have been introduced to deflect surgical rods, including pull wires, shape-memory-alloy actuators, hydraulic actuators, and precurved concentric tubes [91, 92]. However, mechanisms that transmit force to the tip of a rod take up space that could otherwise be used for therapeutically useful components, or removed to make a rod thinner.

A magnet–tipped rod is deflected without any bulky internal mechanisms. Instead, a magnetic field that is passed through a patient's body supplies the energy to bend the rod. The current clinical use of magnet-tipped rods is mainly limited to cardiology, but these rods could be miniaturized for surgical tasks aimed at the many small cavities of the body such as found in the ear, lungs, sinuses, skull base, and heart. Applications could include ablation, sensing, endoscopy, targeted drug delivery, angioplasty, guided electrode implantation, and other diagnostic and interventional tasks.

Three commercially available systems now use magnetic fields to guide cardiac catheters. The *Niobe ES* system uses a pair of large, neodymium-iron-boron (NdFeB) magnets to create a magnetic field across an operating table [93]. The pair of magnets are robotically positioned to guide a magnet-tipped catheter within the heart using fluoroscopic visualization for real-time feedback. The *Catheter Guidance Control and Imaging* [94] system and the *Aeon Phocus* [95] both use solenoid arrays that surround the patient and create an adjustable field to guide cardiac catheters. Like the *Niobe ES* system, both systems are large and immobile, require dedicated floor space, and restrict access to a patient. The large scale of these systems is necessary for manipulating cardiac catheters, which have relatively wide diameters of 2 mm to 4 mm [94]. Ullrich et al. [96] proposed guiding a microcatheter within the eye using the compact OctoMag [97] system, which suggests that there are beneficial applications beyond cardiology that do not require very large equipment.

The strong magnetic field in a magnetic resonance imaging (MRI) scanner also has been considered for magnetic catheter guidance. Roberts et al. [98] placed orthogonal solenoids in the tip of a catheter and adjusted the solenoid currents to control deflection in a MRI scanner. Others, including Settecase et al. [99], Gudino et al. [100], Liu and Çavoşoglŭ [101], and Greigarn and Çavoşoglŭ [102] contributed models and control techniques for solenoid-tipped catheters. However, MRI scanner time is expensive, intraoperative MRI is practicable for only a narrow range of procedures, and many facilities

lack MRI scanners.

A single permanent magnet can serve as a compact and inexpensive magnetic field source. Clark et al. [103] proposed a system for cochlear implantation surgery using a robot-manipulated permanent magnet near a patient's head to deflect a magnet-tipped electrode through the cochlea. Planar bending was considered exclusively, which required only one rotation and one translation of the external magnet. Mahoney and Abbott [104] presented a control method for five degree of freedom steering of an untethered magnetic capsule by robotically manipulating a permanent magnet.

Tunay [105], [106] used Cosserat rod theory to model the three-dimensional static deflection of a magnet-tipped catheter and simulated rotations of a uniform magnetic field to guide a catheter around an obstacle, but tip trajectory control was not demonstrated in the simulation. Greigarn and Çavoşoglŭ [102] presented a motion planning algorithm for a solenoid-embedded catheter modeled as a chain of rigid links connected by springs, and showed with simulations that the method required feedback to compensate for drift.

In this paper we study the previously unsolved problem of guiding a magnet-tipped rod along arbitrary, three-dimensional trajectories. We propose a system in which an external robot manipulates a large permanent magnet to steer a magnet-tipped rod. The rod is deployed by an advancer, which can insert and possibly rotate it axially. We relate the motions of the advancer and robot to deflections of the rod tip using a Kirchhoff rod model, and invert this model using a resolved-rate approach to follow trajectories.

For conciseness, we will refer to the range of magnet-tipped elastic devices simply as "rods" in the remainder of this article, but our methods apply to narrow elastic rods with any cross-sectional profile, including solid rods and tubular cannulas.

5.2 Application : magnet-guided cochlear implantation surgery

To motivate the work that follows, this section will consider the problem of guiding a magnet-tipped electrode array to reduce insertion forces during cochlear implantation surgery, an application for which magnetic guidance is potentially beneficial.

Insertion of an electrode array causes trauma to several sensitive structures inside the cochlea, such as the basilar membrane, osseous spiral lamina, spiral ligament, and vasculature [107–114]. Frequently, this trauma is associated with translocation of the electrode from the scala tympani to the scala vestibuli, as discussed in Chapter 4. Reducing insertion trauma helps preserve residual low frequency hearing capability, which is important for electric-acoustic stimulation strategies which combine a cochlear implant with an acoustic hearing aid [115]. Carlson et al. found that minimizing insertion trauma improves perception of speech transmitted in a fully electric manner through a cochlear implant, suggesting that the benefit of trauma reduction is not limited to residual hearing preservation [68].

Surgical techniques and electrode array designs have been progressively refined to reduce intracochlear trauma, yet total preservation of residual hearing remains rare, especially for full-depth insertions [116]. Cochlear implant electrode arrays are inserted manually using simple hand tools, and surgeons lack the ability to visualize or directly control an electrode's shape as it is pushed into the cochlea. The velocity of insertion is believed to affect intracochlear forces [117], yet the extent to which surgeons can control velocity is unknown. Also, the position of the cochleostomy depends on the surgeon's visual assessment of landmarks, and misplacement of this opening causes trauma [118, 119].

Automating CI surgery using robotic insertion devices can potentially reduce trauma caused by electrode insertion. Hussong et al. [120] and Rau et al. [121] constructed a motorized insertion tool to insert a clinical, perimodiolar electrode array at a controlled speed using the advance off-stylet insertion

technique. Schurzig et al. modified the designs of Hussong et al. and Rau et al. to include a sensitive force-sensing apparatus to measure insertion forces intraoperatively [31]. This tool is designed to attach to the customized microstereotactic frame developed by Labadie et al [27], which is reviewed in Chapter 2. Insertion forces may be further reduced by using a robot with multiple degrees of freedom to perform implantation. Zhang et al. designed an electrode array containing a string which was tensioned by an actuator to control the electrode's curvature [122]. The electrode and string actuator were mounted to a three degree of freedom robot which controlled the electrode's angle of approach into the scala tympani and the depth of insertion. This arrangement was shown to reduce insertion forces in experiments performed on a cochlea phantom. Pile et al. developed a three degree-of-freedom robot to insert a standard perimodiolar electrode array using the advance off-stylet insertion technique, and demonstrated reduced insertion forces during experiments performed on a cochlea phantom [123, 124] .

In addition to the tensionable string described by Zhang et al., several other mechanisms have been proposed to actively control the shape of an electrode array within the scala tympani. Arcand et al. developed fluidic actuators to control the shape of an electrode [125]. Chen et al. embedded a nitinol shape memory alloy rod into a model electrode array to effect deployment at the basal turn [126]. Wu et al. introduced a polypyrrole actuator (a kind of electroactive polymer) to bend an array [127]. These actuation methods hold potential for controlling the shape of electrodes, but significant work remains to develop them into functioning electrode arrays, or to adapt them to existing clinical electrodes.

As mentioned in Section 5.1, Clark et al. proposed magnetic guidance to reduce trauma in CI surgery. Magnetic guidance is advantageous for guiding CI electrodes because it does not require mechanical alterations to the body of an electrode, only attachment of a magnet to the tip. Clinical CI electrodes are the outcome of many years of engineering development [128], and have electrical and mechanical properties that could be disturbed by introduction of mechanisms within the electrode body.

Currently, electrodes are embedded with up to 22 delicate platinum-iridium electrode lead wires.

Clark et al. performed experiments at 3:1 scale, but we believe that magnet-guided CI surgery is feasible at 1:1 scale with clinical electrodes. In Figure 5.1(a), a $0.5\,\mathrm{mm} \times 0.5\,\mathrm{mm} \times 1\,\mathrm{mm}$, a grade N52 NdFeB magnet is shown attached to the tip of a clinical electrode (Med-El Flex28). This electrode is shown with a slightly precurved initial shape, with no external magnetic field applied, and with a deflected shape caused by application of an external magnetic field. The external field was applied by a grade N52 NdFeB magnet, which is described in Section 5.6.2. The centroid of the external magnet was placed approximately $125\,\mathrm{mm}$ from the tip of the electrode, and rotated about an axis perpendicular to its moment vector to an angle that maximized deflection of the electrode.

The scala tympani is a three-dimensional, spiral-shaped cavity, as seen in Figure 5.1(b). There is considerable patient-to-patient variation in the shape of the scala tympani [129–133]. To guide an electrode through this structure with minimal contact force, we seek a mechanics-based model of three-dimensional electrode bending, and a method to plan an electrode trajectory for the specific scala tympany geometry of a patient.

Planning software previously developed by Noble et al. [29] for minimally invasive cochlear implantation surgery computes a segmented volume of the scala tympani and also its medial axis. The medial axis includes all points within a volume that each have at least two closest points on the boundary of the volume [134]. Informally, the medial axis traces a central line that may be considered the "skeleton" of an object. The medial axis is frequently used for robotic path planning, and several authors have used it for planning navigation within lumens of the human body, including the bronchi [135] and colon [136]. Verbist et al. used a related method to identify pressure points in the scala tympani during electrode array insertion [137], but the medial axis has not yet been applied for planning three-dimensional electrode trajectories for CI surgery. In Figure 5.1(b) and (c), we show a segmented scala tympani volume from a

Figure 5.1: (a) A cochlear implant electrode array (Med-El Flex28) with a small NdFeB magnet attached to its tip. A superimposed image shows the electrode as deflected by the field of an external magnet (not shown) (b),(c) Minimally-invasive electrode insertion avoids contact with the walls of the scala tympani. The medial-axis of the scala tympani can be obtained from a pre-operative CT scan and could be used as the basis for planning a trajectory for a magnet-guided insertion.

cadaveric specimen along with a trajectory constructed from the medial axis, which has been smoothed with a smoothing spline [138]. We consider the medial axis to be an optimal position for an electrode centerline in because the medial axis is as far as possible from the walls of the scala tympani.

We envision using the medial axis of the scala tympani as the basis for planning a three-dimensional trajectory for a magnet-tipped electrode array. Using only a tip magnet, it is not possible to fully control the shape of a deflected electrode to conform to medial axis, but by solving for a range of reachable electrode shapes, a sequence of such shapes could be planned to conform as close as possible to the medial axis curve. Previously, Zhang et al. [139] and Pile et al. [123, 124] found optimal insertion parameters for underactuated electrodes in a planar model of the scala tympani. We believe that a similar optimization approach may be useful to find optimal parameters for three-dimensional, magnetically

guided electrode insertion. It is unlikely that electrode motion could be controlled to avoid all contact with the walls of the scala tympani; a realistic model must also include the interaction forces between the electrode and part of the scala tympani.

In the following sections, we describe a robotic system for guiding a general, magnet-tipped rod. We begin by discussing magnetic field models and then introduce an elastic rod model. The models described in this chapter are first steps toward a model-based approach magnet-guided CI insertion, which we will not discuss further.

5.3 Permanent-Magnet Models

A permanent magnet sustains its own magnetic field $\mathbf{B}$ (in units T). The magnetic moment $\mathbf{m}$ (in units $\mathrm{A\,m^2}$) is a vector[1] that expresses a magnet's strength. The magnitude of the moment is equal to the torque on the magnet (in units $\mathrm{N\,m}$) when a unit external field $\mathbf{B}$ is applied orthogonally to $\mathbf{m}$. By convention, $\mathbf{m}$ points from the "south pole" to the "north pole" of the magnet [140]. Magnetization $\mathbf{M}$ (in units $\mathrm{A/m}$) is the magnetic moment per unit volume V. In general, magnetization is a vector field that varies over a magnet's volume. The total magnetic moment is given by

$$\mathbf{m} = \int_V \mathbf{M}\, dV \tag{5.1}$$

Magnetization is nearly uniform in most commercially available magnets, the moment of which can be approximated by $\mathbf{m} \approx \mathbf{M}V$.

5.3.1 Force and Torque on Tip Magnet

Figure 5.2 illustrates the arrangement of magnets that we will consider in this article, which includes an external, permanent magnet with field $\mathbf{B}$ and a small magnet at the tip of a rod with magnetic moment

[1] Boldface will be used to denote vectors. When the coordinate frame of a vector is important, it will be indicated by a superscript Roman letter.

$\mathbf{m}$. The force $\mathbf{F}$ and torque $\mathbf{T}$ applied by the external magnet to the tip magnet are given by

$$\mathbf{F} = (\mathbf{m} \cdot \nabla)\mathbf{B} \tag{5.2}$$

$$\mathbf{T} = \mathbf{m} \times \mathbf{B} \tag{5.3}$$

These equations model the tip magnet as a point magnetic dipole, which is accurate provided that the tip magnet is small enough that the field at its centroid accurately approximates the field over its entire volume. We consider a single, external magnet as the source of $\mathbf{B}$ in this article, but Equations 5.2 and 5.3 can be used with any combination of magnetic field sources.

5.3.2 External Magnet Field Models

We require a model of the external magnet's field $\mathbf{B}$ to calculate force and torque on the tip magnet. The point dipole model is the simplest field model, and it becomes increasingly accurate with distance from a magnet [141]. However, it may be necessary to place the external magnet as close as possible to the tip magnet because field strength decreases rapidly with distance. Exact field models of permanent magnets are accurate at both near and far distances, and have been derived in analytical form for simple magnet shapes such as cylinders [142] and cuboids [143]. Fields of complex magnet shapes or magnet assemblies can be numerically approximated using the finite-difference or finite-element methods, for example [144]. However, such methods have a high computational cost compared to analytical models. To keep our results in this paper as general as possible, and because we foresee applications in which the dipole model is no longer a good approximation, we used the exact field model for a cube-shaped magnet presented by Furlani [143] in the experiments described later in this paper. Both the point-dipole field model and cube field model are presented in the Appendix.

Field models are typically derived in a body-fixed coordinate frame at the centroid of a magnet.

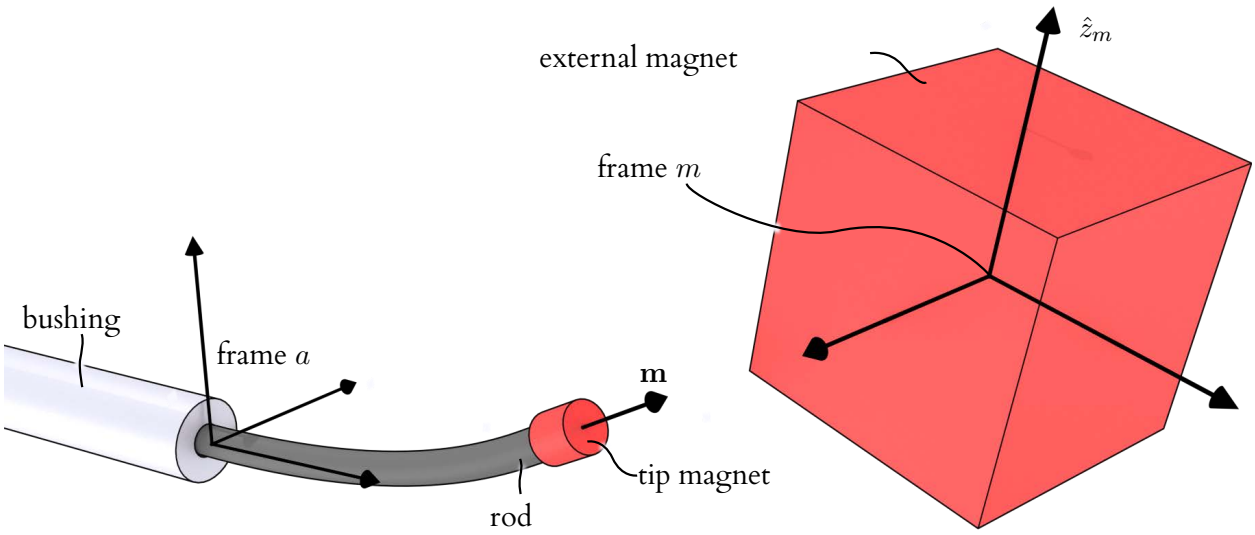

Figure 5.2: An external magnet with coordinate frame m attached to its centroid applies a force and torque to a magnet on the tip of an elastic rod. The advancer consists of a motor (not shown) that pushes, and possibly rotates, a rod into the operative region. A coordinate frame a is fixed to the advancer.

Here, the external magnet will be manipulated by a robot to an arbitrary pose (i.e., position and orientation) with respect to a frame where the position of the rod tip is expressed, which is shown as the frame a attached to the advancer in Figure 5.2. To calculate force and torque on the tip magnet, the field $\mathbf{B}$ must be found at arbitrary positions in frame a. Let R_a^m represent the rotation matrix that transforms coordinates from the frame a attached to the advancer to the body-fixed external magnet frame m, and let $\mathbf{d}_a^m$ denote the vector to the origin of frame a, expressed in frame m. For any field model, the field at any point $\mathbf{p}^a$ in frame a can be found by first transforming the point to the body-fixed magnet frame by

$$\mathbf{p}^m = R_a^m \mathbf{p}^a + \mathbf{d}_a^m \tag{5.4}$$

The magnetic field vector is found in frame m with a body-fixed model $\mathbf{B}^m(\mathbf{p}^m)$ and then rotated to frame a:

$$\mathbf{B}^a = R_m^a \mathbf{B}^m(\mathbf{p}^m) \tag{5.5}$$

5.4 Magnet-Tipped Rod Model

We use the Kirchhoff rod model [145–149] to solve for large, three-dimensional deflections of a magnet-tipped rod. This model represents a thin rod as a one-dimensional curve that can bend and twist under load, but is assumed to be inextensible and unshearable[2]. The static Kirchhoff rod problem culminates in a set of ordinary differential equations, which we will treat as a two-point boundary value problem (BVP). Our review of Kirchhoff's rod theory in this section is inspired by [150].

5.4.1 Kinematics

The centerline of an undeflected rod is represented by an arc-length parameterized space curve $\tilde{\mathbf{p}}(s) \in \mathbb{R}^3$, expressed in some fixed frame. An orthonormal frame is attached to each point on $\tilde{\mathbf{p}}(s)$, and is represented by a rotation matrix $\tilde{R}(s)$, where the tilde symbol denotes association with the undeflected curve. Each local coordinate frame represents the orientation of rod material at the point where it is attached. Under load, $\tilde{\mathbf{p}}(s)$ deflects to a curve $\mathbf{p}(s)$, and the $\tilde{R}(s)$ rotate to $R(s)$, in general. Figure 5.3 illustrates the deflection of a rod and the ensuing rotations of a few local frames.

We assign frames on the undeflected curve such that the z-axis of each frame is tangent to the curve. Frames constrained in this way are called adapted frames. An arc-length parameterized curve has a tangent vector of unit length [151, Ch. 2]. Using a prime symbol to denote differentiation with respect to s, the adapted frame constraint can be written as

$$\tilde{\mathbf{p}}'(s) = \tilde{R}(s)\hat{\mathbf{e}}_z \tag{5.6}$$

in which $\hat{\mathbf{e}}_z = \begin{bmatrix} 0 & 0 & 1 \end{bmatrix}^\mathsf{T}$.

[2] These are reasonable assumptions provided that the rod is neither bent into sharp corners nor subjected to extreme lateral loads [149, Ch. 3, Sec. 7].

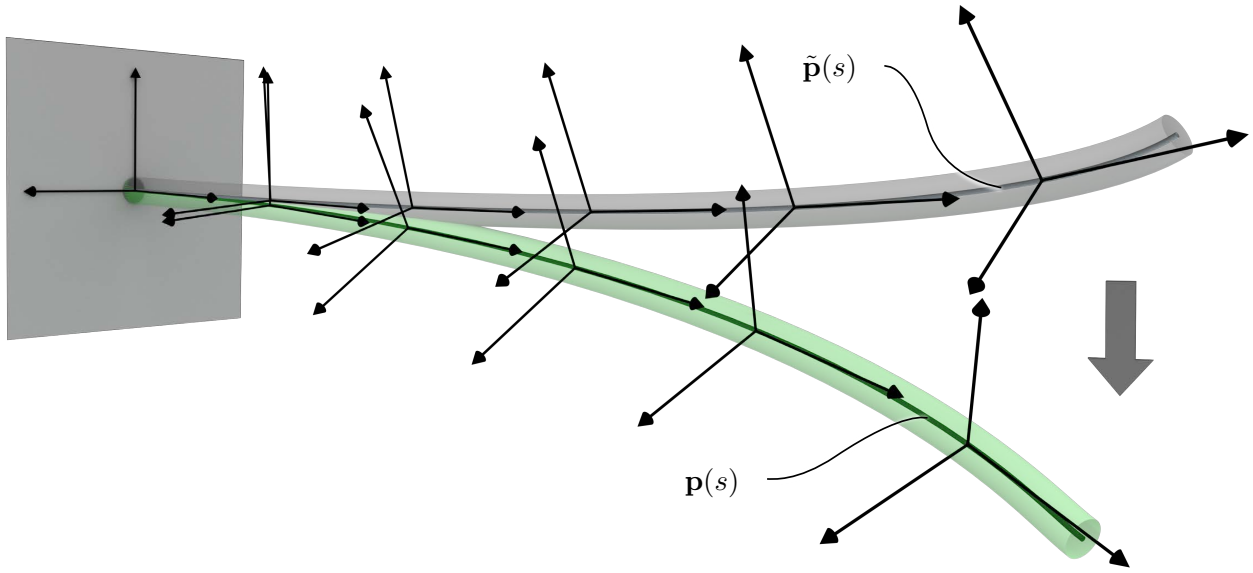

Figure 5.3: A rod is modeled in Kirchhoff's theory as a space curve with a local coordinate frame attached to each point. A few frames are shown at corresponding positions on an undeflected curve $\tilde{\mathbf{p}}(s)$ (which may be arbitrarily precurved), and on the deflected curve $\mathbf{p}(s)$ of the same rod.

The angle of rotation of each frame about a rod's centerline is not constrained by Equation 5.6, and must be chosen in some way. If the rod is initially straight and has a radially symmetric cross-section, choosing all $\tilde{R}(s)$ as identity matrices aligns them to the fixed frame. If the rod is precurved and has asymmetric cross-sections, the x and y axes of each frame can be aligned to the principle axes of each cross-section. If the rod is precurved and radially symmetric, any of several curve framing methods based on the differential geometry of the centerline can be used to assign adapted frames, such as the Frenet-Serret formulas [151, Ch. 2] or the parallel transport method [152, Ch. 20], [153].

5.4.2 Constitutive Relations

The derivative of $R(s)$ with respect to arc-length can be expressed as

$$R'(s) = R(s)U(s) \tag{5.7}$$

in which U is a skew-symmetric matrix. Omitting the argument s for brevity,

$$U = \begin{bmatrix} 0 & -u_z & u_y \\ u_z & 0 & -u_x \\ -u_y & u_x & 0 \end{bmatrix} \tag{5.8}$$

The elements u_x, u_y, and u_z can be seen as components of an axial vector $\mathbf{u}$. Curvatures about the x and y axes are given by u_x and u_y, respectively, and the torsional twist rate is denoted by u_z. A vector $\tilde{\mathbf{u}}$ is found in a similar fashion from $\tilde{R}(s)$. Vectors can also be mapped to skew-symmetric matrices, an operation we will denote by $[\cdot]_\times$.

The vector $\Delta\mathbf{u}(s) = \mathbf{u}(s) - \tilde{\mathbf{u}}(s)$ gives the strain at each material point s. The bending strains about the local x and y axes are given by $\Delta u_x(s)$ and $\Delta u_y(s)$, respectively, and the torsional strain is given by $\Delta u_z(s)$.

We will assume that the rod material is linear-elastic and denote the elastic modulus function by $E(s)$ and the shear modulus function by $G(s)$. The second moments of area about the principle axes of the rod cross-section are denoted by $I_x(s)$ and $I_y(s)$. The polar moment of inertia about the rod centerline, $J_z(s)$, is found by $J_z(s) = I_x(s) + I_y(s)$. Omitting the argument s for brevity, these variables can be arranged into a stiffness matrix

$$K = \begin{bmatrix} EI_x & 0 & 0 \\ 0 & EI_y & 0 \\ 0 & 0 & GJ_z \end{bmatrix} \tag{5.9}$$

The internal moment at any point is proportional to the internal strains. This constitutive

relationship can be written as

$$\boldsymbol{\tau} = RK\Delta\mathbf{u} \tag{5.10}$$

It will be useful to rearrange the above equation in the form

$$\mathbf{u} = K^{-1}R^{\mathsf{T}}\boldsymbol{\tau} + \tilde{\mathbf{u}} \tag{5.11}$$

5.4.3 Equilibrium Equations

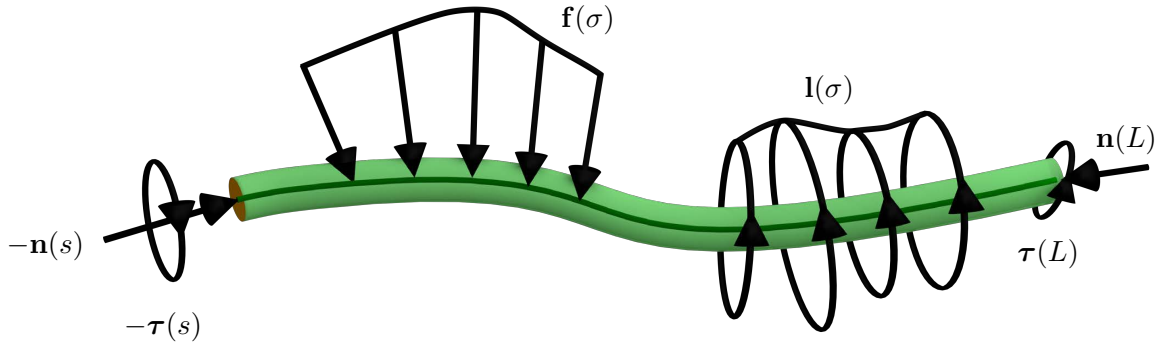

Figure 5.4: Equilibrium equations are found by cutting the rod at an arbitrary point $\mathbf{p}(s)$ and summing all loads from this point to the rod tip. All loads act on the rod's centerline, and include an internal force and torque at s ($\mathbf{n}(s)$, $\boldsymbol{\tau}(s)$), distributed forces and torques along the segment ($\mathbf{f}(\sigma)$, $\mathbf{l}(\sigma)$), and a force and torque at the tip ($\mathbf{n}(L)$, $\boldsymbol{\tau}(L)$).

We show the forces and torques acting on an isolated segment of a rod in Figure 5.4. The segment extends from an arbitrary point $\mathbf{p}(s)$ to the tip $\mathbf{p}(L)$. The internal force $\mathbf{n}(s)$ and internal torque $\boldsymbol{\tau}(s)$ act in a positive sense across the cut on the portion of rod that extends from the base of the rod to s.

Distributed forces and torques that act along the rod are denoted by $\mathbf{f}(\sigma)$ and $\mathbf{l}(\sigma)$ respectively, where σ is a dummy variable for integration. Such loads could be caused by tissue in contact with the

rod, for example. The sum of forces on the cut segment of rod is

$$-\mathbf{n}(s) + \int_s^L \mathbf{f}(\sigma)\, d\sigma + \mathbf{n}(L) = \mathbf{0} \tag{5.12}$$

The total moment on the segment, taken about the origin of the fixed frame, includes the internal torque at $\mathbf{p}(s)$, the moment of the internal force at $\mathbf{p}(s)$, the integral of the distributed torque, the integral of the moment of the distributed forces, the tip torque, and the moment of the tip force:

$$\begin{aligned} -\boldsymbol{\tau}(s) - \mathbf{p}(s) \times \mathbf{n}(s) + \int_s^L [\mathbf{l}(\sigma) + \mathbf{p}(\sigma) \times \mathbf{f}(\sigma)]\, d\sigma \\ +\boldsymbol{\tau}(L) + \mathbf{p}(L) \times \mathbf{n}(L) = \mathbf{0} \end{aligned} \tag{5.13}$$

Equilibrium differential equations are found by differentiating Equations 5.12 and 5.13 with respect to s to obtain

$$\mathbf{n}'(s) + \mathbf{f}(s) = \mathbf{0} \tag{5.14}$$

$$\boldsymbol{\tau}'(s) + \mathbf{p}'(s) \times \mathbf{n}(s) + \mathbf{l}(s) = \mathbf{0} \tag{5.15}$$

5.4.4 Boundary Conditions

Up to this point we have presented a general Kirchhoff rod model. Here, we will describe boundary conditions through which the advancer and robot enter the model. We will specify boundary conditions for a rod with and without a protective bushing, shown schematically in Figures 5.5 and 5.6. In both configurations, a rigid post connects the base of the rod to actuators inside the advancer, which are not shown.

The bushing is useful as a rigid conduit to guide a rod to an operative region. A fixed frame,

labelled a in Figure 5.5, is placed at the distal end of the bushing, oriented such that its z-axis is aligned with the bushing's centerline. The advancer translates the rod by a distance $\ell(t)$ along the z-axis and rotates it by an angle $\psi(t)$ about the same axis (such rotation may be useful with a precurved rod, or if the tip magnet axis is not aligned with the rod centerline). The time t is held constant when solving the BVP and will be omitted as an argument in the remainder of this subsection. We will view the advancer and robot joints as functions of time in Section 5.5, where the rod's motion is planned as a succession of equilibrium states.

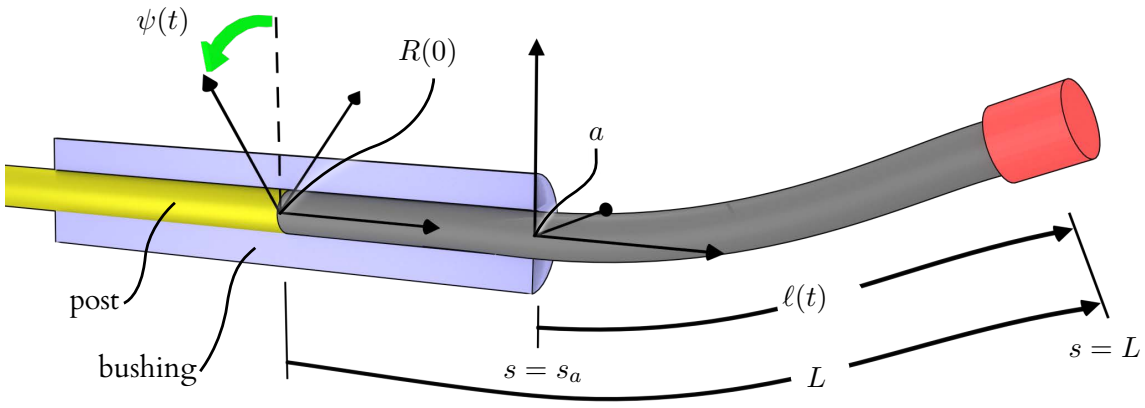

Figure 5.5: A bushing, shown in section view, guides the rod to the operative region. The base of the rod is actuated via a rigid post which translates the rod by a distance $\ell(t)$ and rotates it by an angle $\psi(t)$ relative to frame a. A two point boundary value problem is solved with endpoints at s_a and L.

The material point that coincides with the origin of frame a is denoted by $s_a = L - \ell$, where L is the total length of the rod. We will solve the BVP over the interval $[s_a, L]$, which spans the unconstrained part of the rod.

If the rod is radially symmetric, it may twist within the bushing. We assume that the bushing is frictionless and therefore cannot apply torque about the rod centerline. If the rod is precurved, the bushing exerts reaction forces to conform the rod to the bushing's centerline, but these transverse forces cannot cause torsional deformation because the shear center of a Kirchhoff rod coincides with its

centerline [154]. Thus, deformation in the bushing consists solely of twisting around the local z-axis, and is caused exclusively by $\tau_z(s_a)$, the z-component of the internal moment at the distal end of the bushing. The z-axes of the local frames are aligned within the bushing, thus the transposed rotation matrix in Equation 5.11 does not affect the z-component of $\mathbf{u}(s)$, which becomes

$$u_z(s) = \frac{\tau_z(s_a)}{G(s)J_z(s)} + \tilde{u}_z(s) \tag{5.16}$$

The bushing constrains the position and direction of the rod centerline at $\mathbf{p}(s_a)$, but the frame $R(s_a)$ is rotated about the z-axis by an angle

$$\phi = \psi + \int_0^{s_a} u_z(s)\, ds \tag{5.17}$$

Thus, the boundary conditions at s_a are

$$\mathbf{p}(s_a) = \mathbf{0} \tag{5.18}$$

$$R(s_a) = R_z(\phi) \tag{5.19}$$

where $R_z(\cdot)$ is a rotation about the fixed z-axis. Note that the angle ϕ depends on the constant $\tau_z(s_a)$, which is unknown at the outset of solving the BVP. In the next subsection we will discuss methods for finding $\tau_z(s_a)$ and other unknown constants using a numerical BVP solver.

If a non-radially symmetric rod is used, a bushing may be designed to prevent the rod from twisting or rotating (e.g., a "D"-shaped rod in a similarly shaped hole). For such a bushing, rotation by ψ could be implemented as rotation of the entire bushing about the fixed z-axis, whereby conditions 5.18 and 5.19 can be applied by setting $\phi = \psi$.

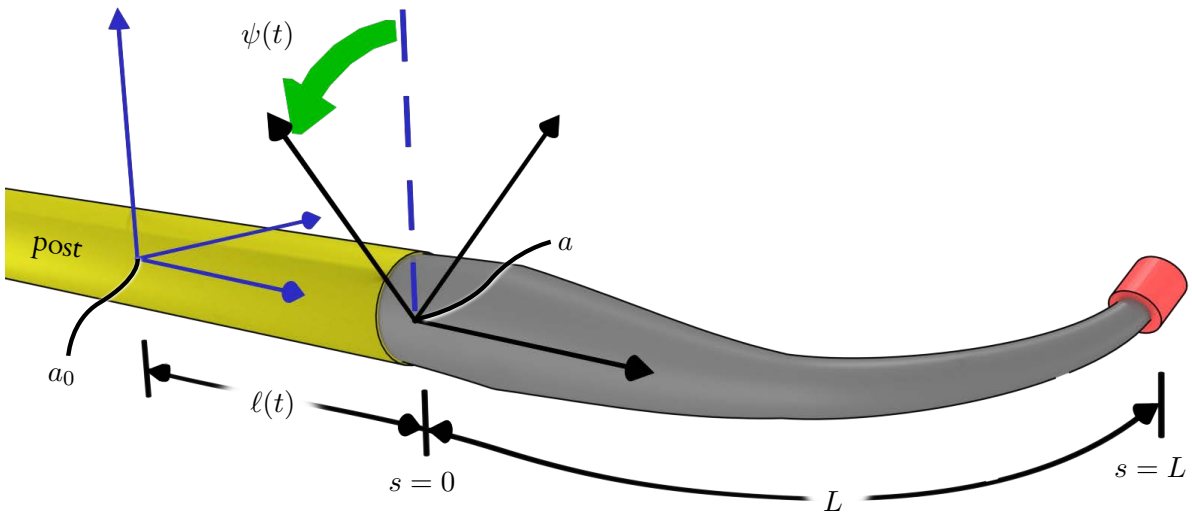

Figure 5.6: The bushing may be discarded to accommodate tapered or other unusual rod shapes. In this case, the BVP is solved over the fixed interval $[0, L]$, and the advancer displacements $\ell(t)$ and $\psi(t)$ are interpreted as parameters of a rigid transformation of frame a with respect to an initial pose a_0.

The pose of the external magnet (frame m) is known, in general, with respect to the robot base frame r from a forward kinematic function in the form

$$T_m^r = T_m^r(\boldsymbol{\theta}) \tag{5.20}$$

in which T is a 4×4 homogeneous transformation matrix, and $\boldsymbol{\theta}$ is a joint displacement vector. We assume that the pose of the advancer frame a is known relative to the robot base frame r as a transformation T_a^r. For a particular robot posture, the field $\mathbf{B}$ at position $\mathbf{p}(L)$ is found using Equations 5.4 and 5.5, obtaining R_a^m and $\mathbf{d}_a^m$ from $T_a^m = T_r^m T_a^r$. The tip position $\mathbf{p}(L)$ depends on the equilibrium configuration of the rod, and like $\tau_z(s_a)$, this constant is unknown when beginning to solve the BVP.

It may sometimes be desirable to dispose of the bushing, as shown in Figure 5.6. This configuration could be useful if the rod is tapered, for example. We embed frame a in the base of the rod in this case, and interpret ℓ and ψ as displacements of frame a relative to the pose a_0 at which T_a^r has been

measured. Thus, the pose of the advancer relative to the magnet now becomes

$$T_a^m = T_r^m T_a^r \begin{bmatrix} R_z(\psi) & \ell \hat{\mathbf{e}}_z \\ \mathbf{0} & 1 \end{bmatrix} \tag{5.21}$$

By setting $s_a = 0$, boundary conditions 5.18 and 5.19 hold as stated above.

Next, we consider loads on the tip. The tip magnet may be attached in any orientation with respect to the tip frame $R(L)$, though it may often be convenient to align its magnetization vector with the rod centerline. Let the unit vector $\hat{\mathbf{d}}$ in frame $R(L)$ denote the direction of the magnetization vector with respect to the rod tip. The magnetization vector $\mathbf{m}$ can be factored as $\|\mathbf{m}\|\,\hat{\mathbf{m}}$, where $\|\mathbf{m}\|$ may be approximated as suggested in Section 5.3, and $\hat{\mathbf{m}}$ is a unit vector expressed in the fixed frame as

$$\hat{\mathbf{m}} = R(L)\,\hat{\mathbf{d}} \tag{5.22}$$

The vector $\hat{\mathbf{m}}$ depends on the equilibrium tip frame orientation $R(L)$, and is thus an additional unknown.

The force and torque exerted by the external magnet on the tip magnet are found using Equations 5.2 and 5.3. We add a gravitational force $\mathbf{G}$ to prescribe the conditions

$$\mathbf{n}(L) = (\mathbf{m} \cdot \nabla)\,\mathbf{B} + \mathbf{G} \tag{5.23}$$

$$\boldsymbol{\tau}(L) = \mathbf{m} \times \mathbf{B} \tag{5.24}$$

5.4.5 Numerical Solutions

Analytic solutions have been found for a few special Kirchhoff rod problems, but solutions for three-dimensional deflection problems usually require numerical methods, such as the finite-difference or

finite-element methods.

The magnet-tipped rod BVP is given by Equations 5.6, 5.7, 5.14, and 5.15, together with the boundary conditions stated in Equations 5.18, 5.19, 5.23 and 5.24.

We use the `bvp5c` function in Matlab (The Mathworks, Natick, MA) by Kierzenka and Shampine [155] to solve the BVP. This solver implements a finite-difference method based on the four-stage Lobatto IIIA collocation formula, and can find unknown parameters that appear in a BVP. We use this capability to find the parameters

$$\mathbf{\Pi} = \begin{bmatrix} \tau_z(s_a) \\ \mathbf{p}(L) \\ \hat{\mathbf{m}} \end{bmatrix} \tag{5.25}$$

Many BVP solvers are not explicitly designed to solve for unknown constant parameters. However, by augmenting the state equations with the trivial equations

$$\mathbf{\Pi}' = \mathbf{0} \tag{5.26}$$

any BVP solver can be used to solve the problem (see [156, Ch. 1]). Additional boundary conditions follow from the definition of $\mathbf{\Pi}$. For example, $\Pi_1(s_a) = \tau_z(s_a)$, $\Pi_2(L) = p_x(L)$, etc.

Without a good initial guess, BVP solvers often fail to find a correct solution, or potentially any solution at all. In the next section we will describe a method to incrementally displace a rod to follow a trajectory, in which a solution obtained at step n furnishes a guess for the solution sought at step $n+1$. The `bvp5c` solver returns and accepts a set of data that includes optimal collocation mesh points, the state variables at those points, and the parameter values found at the end of an iteration. We pass all of this

data forward to the subsequent iteration as an initial guess.

5.5 Trajectory Following

5.5.1 Forward Kinematics

Each solution of the magnet-tipped rod BVP describes the full, deflected shape of the rod. To plan trajectories, we limit our attention to the rod tip, and introduce the variable $\mathbf{r}(t)$ to represent the tip position $\mathbf{p}(L)$ that is found by solving the BVP with the boundary conditions applied by the advancer and robot at time t.

We group the advancer and robot joint variables as

$$\mathbf{q}(t) = \begin{bmatrix} \psi(t) \\ \ell(t) \\ \boldsymbol{\theta}(t) \end{bmatrix} \tag{5.27}$$

Let p denote the advancer degrees of freedom, such that $p = 1$ if only $\ell(t)$ is actuated, and $p = 2$ if $\psi(t)$ is also actuated. Thus, if the robot has j joints, then $\mathbf{q}$ has dimension $p + j$.

With the variable $\mathbf{q}$, the forward kinematics of the cooperative advancer-robot system can be expressed as a function $\Omega : \mathbb{R}^{p+j} \to \mathbb{R}^3$

$$\mathbf{r} = \Omega(\mathbf{q}) \tag{5.28}$$

We wish to invert Ω to find a joint trajectory $\mathbf{q}(t)$ corresponding to some desired tip trajectory $\mathbf{r}(t)$. However, Ω is not amenable to direct inversion because $\mathbf{q}$ may not be unique and Ω is found as a solution of a differential equation. We will find solutions to the inverse problem that use the Jacobian matrix $J \in \mathbb{R}^{3\times(p+j)}$ of Ω. Using a raised dot symbol to denote differentiation with respect to time, the

Jacobian J maps the control vector velocity $\dot{\mathbf{q}}$ to the tip velocity $\dot{\mathbf{r}}$

$$J(\mathbf{q}) = \frac{\partial \Omega(\mathbf{q})}{\partial \mathbf{q}} \tag{5.29}$$

$$\dot{\mathbf{r}} = J(\mathbf{q})\,\dot{\mathbf{q}} \tag{5.30}$$

5.5.2 Inversion and Redundancy Resolution

If J is square and full rank, then it can be inverted to solve for a unique $\dot{\mathbf{q}}$. If either $p = 1$ and $j > 2$ or if $p = 2$ and $j > 1$, then the system is redundant to the tip control task, provided that J is full (row) rank. The advancer and robot form a cooperative system in which the rod tip position is the output, and the robot end-effector is analogous to an intermediate link in a more traditional robot structure. There are, in general, multiple solutions for the external magnet pose. The Jacobian that maps the spatial velocity of the external magnet to the force/torque wrench on the tip magnet is rank five for dipole magnets [104] (rotations about the dipole axis leave the field unchanged). Thus, perturbations of the external magnet pose alter the tip boundary conditions and change the shape of the rod.

Redundancy may be exploited to fulfill secondary goals. We will solve for $\dot{\mathbf{q}}$ in the redundant case using weighted generalized inverses [157] of the Jacobian, denoted by $J^{\#}$. A weighted norm of joint rates is given by

$$\|\dot{\mathbf{q}}\|_W = \left(\dot{\mathbf{q}}^{\mathsf{T}} W \dot{\mathbf{q}}\right)^{\frac{1}{2}} \tag{5.31}$$

in which $W \in \mathbb{R}^{(p+j)\times(p+j)}$ is a positive-definite weighting matrix. A vector $\dot{\mathbf{q}}$ that minimizes Equation 5.31 and satisfies $\dot{\mathbf{r}} = J\dot{\mathbf{q}}$ can be found by minimizing the cost function C

$$C(\dot{\mathbf{q}}, \lambda) = \left(\dot{\mathbf{q}}^{\mathsf{T}} W \dot{\mathbf{q}}\right)^{\frac{1}{2}} + \boldsymbol{\lambda}^{\mathsf{T}}(\dot{\mathbf{r}} - J\dot{\mathbf{q}}) \tag{5.32}$$

where $\boldsymbol{\lambda}$ is a vector of Lagrange multipliers. If J is full (row) rank, the weighted least norm solution to Equation 5.32 for $\dot{\mathbf{q}}$ is

$$\dot{\mathbf{q}} = W^{-1}J^{\mathsf{T}}\left(JW^{-1}J^{\mathsf{T}}\right)^{-1}\dot{\mathbf{r}} \tag{5.33}$$

The product $W^{-1}J^{\mathsf{T}}\left(JW^{-1}J^{\mathsf{T}}\right)^{-1}$ will hence be denoted by $J^{\#}$.

A robot's joints may include a combination of prismatic and revolute types, and may have different joint limits, torque limits, etc. The matrix W can be chosen to emphasize the contribution of certain joints to a weighted least norm solution. If the joint weight matrix W is diagonal, each entry w_i along the main diagonal independently weights one joint axis. Increasing a weight w_i *decreases* the contribution of the corresponding joint. If all joints are equally weighted ($W = I$), then $J^{\#}$ reduces to the Moore-Penrose pseudoinverse. We will denote an initial matrix of joint weights chosen for the above considerations by W_0, to distinguish it from a final matrix W, which we will describe shortly.

Joint weights can be varied during robot motion to fulfill secondary tasks with a redundant robot. Chan and Dubey [158] employed a penalty function that increased as joints approached their limits. Joint weights were calculated from the gradient of this function to push joints away from their limits. Park et al. [159] and Xiang et al. [160] both presented formulations based on the weighted generalized inverse for fulfilling multiple subtasks with a redundant robot.

5.5.3 Avoiding an Obstacle Using a Virtual Wall

We will adjust W to deflect the external magnet away from a virtual wall established between the external magnet and the patient or other forbidden region, such as that surrounding a surgical instrument. We represent the wall by an infinite plane, parameterized by a unit normal vector $\hat{\mathbf{n}}$ pointed away from the prohibited side of the wall, and by the shortest distance of the wall from the origin of the reference frame, denoted by D. The position of the centroid of the external magnet in frame a is found using

Equation 5.20 and is denoted here by $\mathbf{x}$. The shortest distance d from the center of the external magnet to the plane is given by

$$d = \hat{\mathbf{n}} \cdot \mathbf{x} + D \tag{5.34}$$

A function H is chosen to increase rapidly as the external magnet approaches the wall. We adapt the following artificial potential field function from Khatib [161]

$$H(d) = \begin{cases} \eta \left(\frac{1}{d} - \frac{1}{\epsilon}\right)^2, & \text{if } d \leq \epsilon \\ 0, & \text{if } d > \epsilon \end{cases} \tag{5.35}$$

The constant gain factor η scales the magnitude of H, and ϵ is an activation threshold distance.

Let $\mathbf{v}$ be a combination of the linear velocity of the advancer $\dot{\ell}$, the angular (roll) velocity of the rod $\dot{\psi}$, the translational components of the robot end-effector velocity $\dot{\mathbf{x}}$, and the angular velocity vector of the external magnet ω as

$$\mathbf{v} = \begin{bmatrix} \dot{\psi} \\ \dot{\ell} \\ \dot{\mathbf{x}} \\ \omega \end{bmatrix} \tag{5.36}$$

The Jacobian of the advancer is a trivial identity matrix, because $\dot{\ell} = \frac{dq_1}{dt}$ and $\dot{\psi} = \frac{dq_2}{dt}$. Using the robot's geometric Jacobian J_r, a combined advancer-robot Jacobian J_{ar} can be expressed as

$$J_{ar} = \begin{bmatrix} I_p & \mathbf{0} \\ \mathbf{0} & J_r \end{bmatrix} \tag{5.37}$$

such that

$$\mathbf{v} = J_{ar}\dot{\mathbf{q}} \tag{5.38}$$

Whitney [162] observed that a weighted norm can be defined for the spatial velocity of a redundant robot's end-effector and then transformed into a corresponding joint norm. A positive-definite weighting matrix $\bar{W}$ of dimension $n \times n$, in which n are the degrees of freedom of the robot end-effector, establishes the norm

$$\|\mathbf{v}\|_{\bar{W}} = \left(\mathbf{v}^{\mathsf{T}}\bar{W}\mathbf{v}\right)^{\frac{1}{2}} \tag{5.39}$$

Substituting Equation 5.38 into Equation 5.39 yields

$$\|\mathbf{v}\|_{\bar{W}} = \left(\dot{\mathbf{q}}^{\mathsf{T}}J_{ar}^{\mathsf{T}}\bar{W}J_{ar}\dot{\mathbf{q}}\right)^{\frac{1}{2}} \tag{5.40}$$

By comparing Equations 5.31 and 5.40, it is seen that W is obtainable from $\tilde{W}$ by a congruence transformation

$$W = J_{ar}^{\mathsf{T}}\bar{W}J_{ar} \tag{5.41}$$

in which it is assumed that J_{ar} is nonsingular. We will choose $\bar{W}$ to be a diagonal matrix and, numbering diagonal elements from the upper left corner, we will increase the elements $\bar{w}_{p+1}$ through $\bar{w}_{p+3}$ to suppress corresponding components of $\dot{\mathbf{x}}$ as the external magnet approaches the wall. Depending on the direction of $\dot{\mathbf{x}}$, some of its components $\dot{x}_i$ may cause H to increase at a faster rate than others and should be attenuated proportionally. Inspired by [158], we will use the absolute values of the components of ∇H to weight the components of $\bar{W}$ corresponding to $\dot{\mathbf{x}}$.

The weighted Jacobian solution does not distinguish among the directions of the weighted variables. No weighting should be used for components of $\dot{\mathbf{x}}$ headed away from the wall, otherwise the

external magnet will tend to become "trapped" near the wall. The wall normal vector has components $\hat{\mathbf{n}} = \begin{bmatrix} n_1 & n_2 & n_3 \end{bmatrix}^\mathsf{T}$. If any component of $\dot{\mathbf{x}}$ is directed away from the wall, its corresponding weight $\bar{w}_i$ is set to zero.

$$\bar{w}_{p+i} = \begin{cases} \left|\frac{\partial H(d)}{\partial x_i}\right|, & \text{if } \dot{x}_i n_i \leq 0 \\ 0, & \text{if } \dot{x}_i n_i > 0 \end{cases} \tag{5.42}$$

The joint weights required for Equation 5.33 are then found by

$$W = W_0 + J_{ar}^\mathsf{T} \bar{W} J_{ar} \tag{5.43}$$

Alternatively, an initial weight matrix $\bar{W}_0$ can be specified in the robot's task space, perhaps using an inertia tensor or other application-specific weighting. With this method, the joint weights are given by

$$W = J_{ar}^\mathsf{T} \left(\bar{W}_0 + \bar{W}\right) J_{ar} \tag{5.44}$$

5.6 Experimental Methods

We assembled a magnet-tipped rod guidance system to execute experimental trajectories while measuring the rod tip positions. The experimental apparatus was arranged on a benchtop as illustrated in Figure 5.7.

5.6.1 Advancer and Magnet-Tipped Rod

The rod was a straight, glass optical fiber (Item 57 062, Edmund Optics, NY, USA), $10\,\mathrm{cm}$ in length with a diameter of $0.24\,\mathrm{mm}$. Two NdFeB magnets (Cyl-0010, Engineered Concepts, Birmingham, AL, USA) were attached coaxially to the tip of the rod using cyanoacrylate adhesive (Loctite 4014 Prism Instant Adhesive, Henkel Corp., Rocky Hill, CT, USA). The magnets were cylinders, each $0.75\,\mathrm{mm}$ in diameter and $1\,\mathrm{mm}$ long. Each magnet was grade N50, and was magnetized along its cylindrical axis.

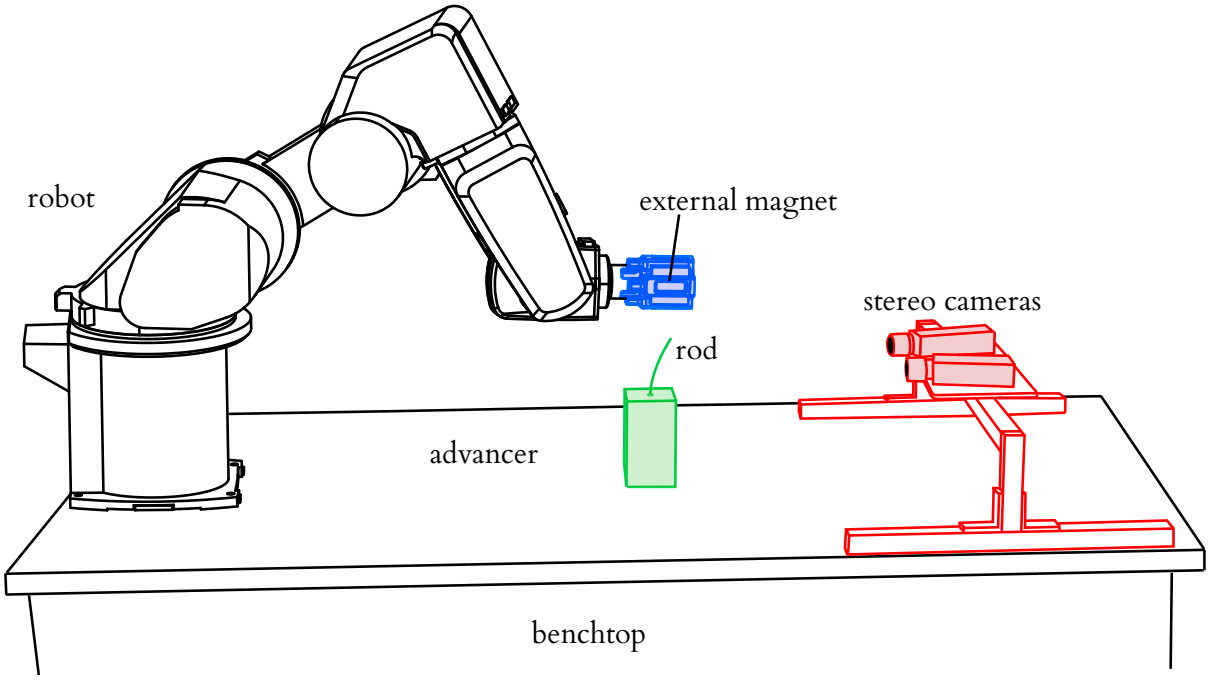

Figure 5.7: Experimental apparatus. A NdFeB magnet was mounted to a six-degree-of-freedom (6-DOF) serial robot to guide a magnet-tipped rod along trajectories. The length of rod was varied by a 1-DOF advancer. A stereo-camera pair was used to measure rod tip positions. The cameras were not used for feedback.

The advancer, shown in Figure 5.8, consisted of a rigid acrylic frame that housed a piezoelectric linear motor (SLC-1770, SmarAct GmbH, Oldenburg, Germany) which had an encoder resolution of 1 µm. The rod was attached to a vee-shaped clamp on the moving slide of the motor. This clamp applied the boundary conditions stated in Equations 5.18 and 5.19, with $\psi = 0$, as we did not rotate the rod. A low-friction bushing on the top surface of the acrylic was fabricated from a 3.2 mm thick sheet of acetal polymer using a CO_2 laser cutting machine.

5.6.2 Robot and External Magnet

A six-degree-of-freedom serial robot (Model RV-3S, Mitsubishi Electric US, Inc., Cypress, California) was used to manipulate the external magnet. The position repeatability of the robot was 0.02 mm, according to the manufacturer.

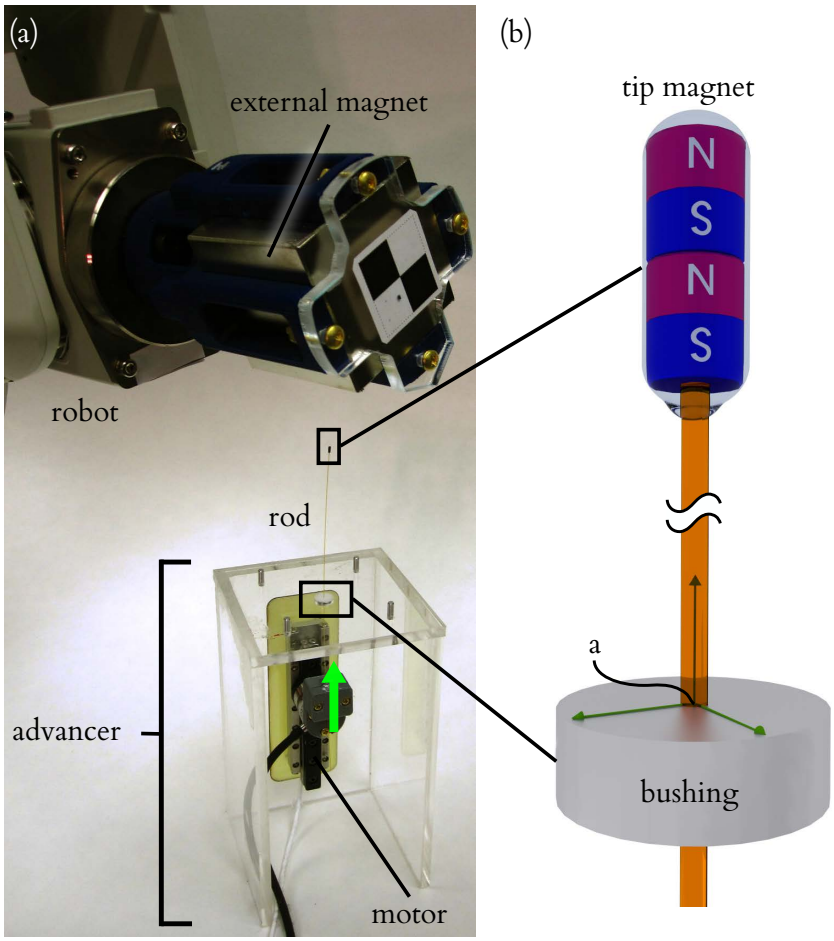

Figure 5.8: (a) A cube-shaped NdFeB magnet was held in a fixture attached to the robot. (b) The rod was an optical fiber, 0.24 mm in diameter, which had two small NdFeB magnets attached to its tip. The rod was pushed by a linear motor through a bushing that constrained the position and direction of the rod.

The external magnet was a cube-shaped, grade N52 NdFeB magnet (NB064-N52, Applied Magnets, Plano, TX, USA), with an edge length of 5.08 cm. The magnet was placed in a fixture attached to the robot end-effector, which is shown in Figure 5.8. The magnet was oriented in the fixture with its magnetization vector orthogonal to the robot's sixth joint axis.

In order to position the external magnet to desired poses with respect to the advancer frame (frame a in Figure 5.5 or frame a_0 in Figure 5.6), a registration procedure was required to determine the pose of the robot's base frame with respect to the advancer frame. The relationship between these frames

is described by transformation T_a^r in Section 5.5, and could be obtained in many ways. For example, in a clinical setting, one might attach optically tracked markers to both the robot and the advancer, to continuously observe the position of each in a common reference frame. In our benchtop experiments, neither the advancer nor robot base frame moved, so it was not necessary to continuously track their positions (T_a^r was constant). Thus, we obtained transformation T_a^r by placing the robot's end-effector at a known pose with respect to the advancer by fitting a feature on the external magnet fixture to a matching feature on the advancer housing.

5.6.3 Trajectory Computation and Control

We planned trajectories by numerically integrating Equation 5.33 using Matlab software. A central difference formula was used to approximate the Jacobian. The notation $[J(\mathbf{q})]_{\bullet,n}$ signifies all rows of the n^{th} column of J, which were obtained by

$$[J(\mathbf{q})]_{\bullet,n} \approx \frac{\Omega(\mathbf{q}+\mathbf{h}_n) - \Omega(\mathbf{q}-\mathbf{h}_n)}{2h} \tag{5.45}$$

in which $h \in \mathbb{R}$ is a small increment and $\mathbf{h}_n \in \mathbb{R}^{p+j}$ is a vector with h in the n^{th} row and zeros in all other rows. Small errors caused by discretization of the rate variables and numerical approximation of the Jacobian tend to accumulate during numerical integration. We found that drift is effectively reduced by a closed-loop inverse kinematics (CLIK) algorithm [163] of the form

$$\dot{\mathbf{q}} = J^{\#}(\mathbf{q})\,\dot{\mathbf{r}} + \Gamma\left(\mathbf{r} - \Omega(\mathbf{q})\right) \tag{5.46}$$

in which the scalar $\Gamma < 1$ is a closed-loop gain constant.

We wrote a program in the C language to control the serial robot and advancer, and to trigger

acquisition of stereo images. The program executed pre-planned trajectories on a desktop computer with a 2.67 GHz Intel Xeon processor, which ran a Linux Ubuntu 11.04 operating system.

5.6.4 Stereo Camera Measurements

Two digital cameras (XCD-X710, Sony Corporation, Japan) were mounted in a stereo configuration to a rigid aluminum frame attached to the benchtop, approximately $40\,\mathrm{cm}$ from the advancer. Prior to acquiring experimental images, we used the OpenCV library [164] to find stereo calibration parameters from images of a checkerboard pattern. During trajectory execution, the control software automatically triggered acquisition of image pairs. Each image measured 1024×768 pixels, and was processed to correct lens distortion using the OpenCV library.

To measure a three-dimensional point, image coordinates of the point were manually selected in corresponding images. The three-dimensional point was then triangulated using an iterative least-squares method that minimized the stereo reprojection error [165].

It was necessary to transform measured points, which were found in the camera frame c, to the advancer frame a for comparison with planned trajectory points. To find the origin of frame a relative to c, we measured the position of the advancer hole. The advancer frame was defined to be parallel to the robot base frame r. An optical target was attached to the robot end-effector and translated along each coordinate direction of frame r, and the endpoints of these translations were measured to find the axes of frame r within frame c. With the position and orientation of frame a relative to c, we constructed a transformation T_c^a to transform measured points to frame a.

5.6.5 Calibration

We calibrated our model by adjusting the small set of sensitive parameters listed in Table 5.1. Parameter EI_x is the bending stiffness of the rod. The rod had a circular cross-section, therefore $EI_y = EI_x$. The

torsional stiffness GJ_z was calculated to be $5.33 \times 10^{-6}\,\mathrm{N\,m^2}$ from the calibrated value of EI_x. The magnetizations of the external magnet $\mathbf{M}_{ext}$ and tip magnet $\mathbf{M}_{tip}$ have a large effect on accuracy because the calculated forces and torques on the tip magnet depend on the magnitudes of these two quantities. The mass of the tip magnet m_{tip} determines the gravitational force $\mathbf{G}$ in Equation 5.23. The total rod length L was initially measured to be $10\,\mathrm{cm}$, but the process of manually clamping the rod to the motor caused some uncertainty in this parameter. Parameters δx, δy, and δz are small corrections to the translational components of T_a^r. Rotational components of T_a^r were excluded because frame a was defined to be parallel to r in the registration process described above, and enabling rotation between these frames did not significantly improve calibration results during initial sensitivity tests.

A set of 60 randomized $\mathbf{q}$ vectors were used for parameter calibration. They prescribed poses for the robot and advancer at which images were acquired with the stereo cameras. The k^{th} rod tip position as measured from the stereo images is denoted by $\mathbf{r}_k$. The k^{th} rod tip position found by solving the BVP with controls $\mathbf{q}_k$ and parameter vector $\boldsymbol{\gamma}$ is denoted by $\Omega(\mathbf{q}_k, \boldsymbol{\gamma})$. An initial guess for $\boldsymbol{\gamma}$ was selected by coarse adjustment of nominal values. We used the `fmincon` function in Matlab to find the parameters $\boldsymbol{\gamma}_{cal}$ that minimize the objective function

$$\boldsymbol{\gamma}_{cal} = \arg\min_{\boldsymbol{\gamma}} \left(\sum_{k=1}^{60} \|\mathbf{r}_k - \Omega(\mathbf{q}_k; \boldsymbol{\gamma})\| \right) \tag{5.47}$$

This function computes the error between predicted and measured tip positions, summed over the calibration set. We define tip error as the Euclidean norm of the difference between a measured tip position and a modeled tip position. After finding optimal calibration parameters, the mean tip error for the calibration set was $0.62\,\mathrm{mm}$.

Table 5.1: Calibrated values of model parameters

Parameter	Value
EI_x	$6.17 \times 10^{-6}\,\mathrm{N\,m^2}$
$\|\mathbf{M}_{ext}\|$	$1.21 \times 10^{6}\,\mathrm{A/m}$
$\|\mathbf{M}_{tip}\|$	$1.24 \times 10^{6}\,\mathrm{A/m}$
m_{tip}	$3.65 \times 10^{-5}\,\mathrm{kg}$
L	$98.75\,\mathrm{mm}$
δx	$2.00\,\mathrm{mm}$
δy	$0.43\,\mathrm{mm}$
δz	$1 \times 10^{-5}\,\mathrm{mm}$

5.7 Experiments

We executed several three-dimensional, open-loop rod tip trajectories planned using the methods described in Section 5.5. The mean and standard deviation (SD) of tip error measurements for each trajectory are presented in Table 5.2, which also lists the number n of tip measurements for each trajectory. Advancer frame coordinate axes are shown in each figure below, where the positive x-axis points toward the midpoint of the stereo cameras. With the exception of the trefoil knot trajectory discussed below, we planned trajectories using all six joints of the robot. The pseudoinverse of J was used to plan all trajectories except the virtual wall trajectory, in which a weighted generalized inverse was used.

Table 5.2: Rod tip error

Trajectory	Mean (mm)	SD (mm)	n
Square, xy plane	0.98	0.22	199
Square, zx plane	0.83	0.07	199
Square, zy plane	0.96	0.25	199
Concho-spiral	1.02	0.32	249
Square, xy plane with obstacle	1.07	0.23	249
Trefoil knot, 2-DOF robot	1.52	0.48	249

Figure 5.9(a) shows tip measurements from three square-shaped tip trajectories within mutually orthogonal planes. This experiment tested the ability to track straight lines in various positions and

orientations. Each square had a planned edge length of 2 cm, and was executed with a tip velocity of 0.4 mm/s. The center of each square was located 6 cm above the origin of the advancer frame. The full rod shape found by solving the BVP (i.e., the planned shape) is shown at the starting point of each trajectory. A composite photograph of 40 sampled positions from a video recording of the zy-plane trajectory is shown in Figure 5.9(b).

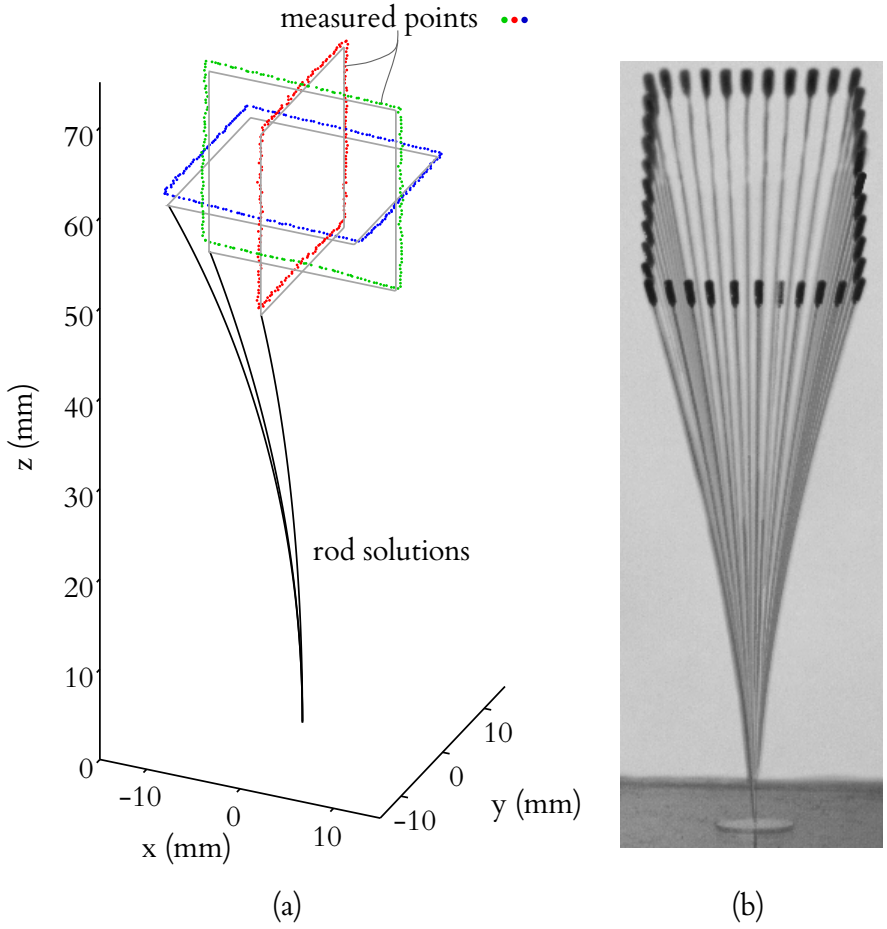

Figure 5.9: (a) The tip of the rod was guided along three square-shaped trajectories, each with an edge length of 2 cm. Measured tip positions are shown as dots, with the planned trajectories shown as solid lines next to the dots. Examples of rod solutions are shown at the starting point of each trajectory. (b) Composite photograph constructed from 40 sampled positions of the zy-plane square trajectory.

We next tested a curved trajectory, the concho-spiral, shown in Figure 5.10. The concho-spiral is a logarithmic spiral wound around a cone, with a curvature inversely proportional to arc-length [166].

This trajectory tested tip accuracy for both small rod deflections (toward the apex of the cone), and large deflections (toward the base). The trajectory is given in cylindrical coordinates by

$$r = \beta\,\varphi\mu^{\eta} \tag{5.48}$$

$$\theta = \beta\,\eta \tag{5.49}$$

$$z = z_0 + \beta\,\xi\,\mu^{\eta} \tag{5.50}$$

We solved for parameter η to plan a constant tip speed of $0.4\,\mathrm{mm/s}$. Parameters μ, φ, and ξ control the spiral's shape, which we chose as 1.04, 0.08, 0.05, respectively. The scaling factor $\beta = 0.0167$ was chosen to fit the shape into the rod tip workspace. The offset distance z_0 is places the apex of the spiral $6\,\mathrm{cm}$ above the origin of the advancer frame.

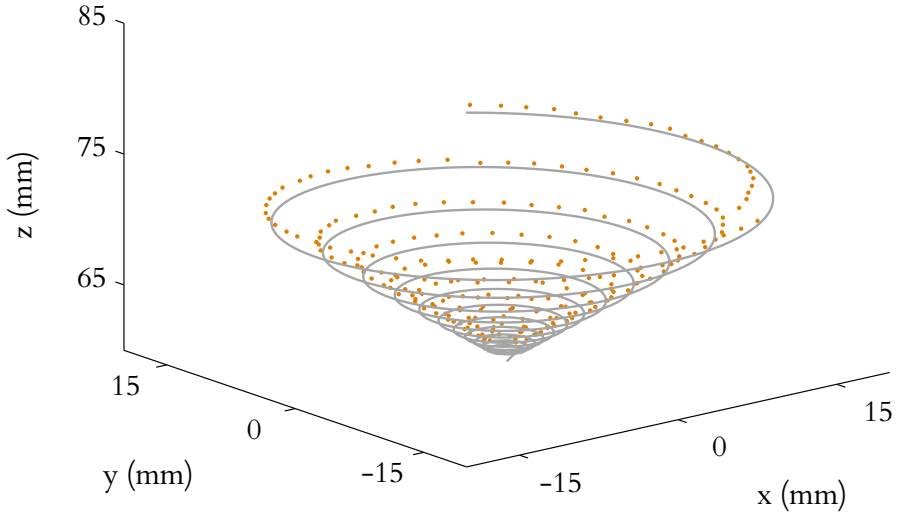

Figure 5.10: The concho-spiral trajectory tested accuracy over a range of rod deflections.

To test obstacle avoidance, we projected a virtual planar wall into the workspace of the external magnet. The planned tip trajectory was a square in the xy plane of frame a, identical to that shown in Figure 5.9, but now starting from the center of the square and following a diagonal line toward the first

corner. An initial weighting matrix $\bar{W}_0 = I_6$ was used with Equation 5.43, as this was found to result in smooth motion of the external magnet. Figure 5.11 shows both the rod tip measurements and the planned motion of the external magnet centroid, which begins by tracking the diagonal line of the rod tip but is deflected by the virtual wall. An external magnet trajectory planned without wall avoidance is also shown as a dashed line, and violates the wall (the rod tip measurements for this unweighted external magnet trajectory are those shown in Figure 5.9).

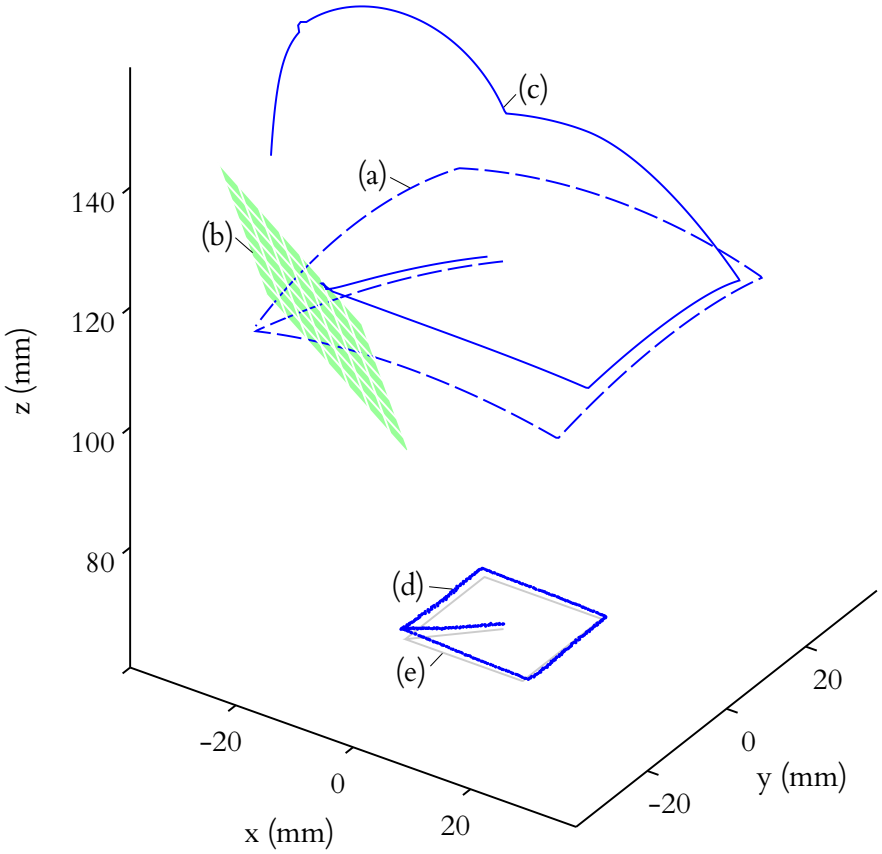

Figure 5.11: The external magnet trajectory (a) violates a virtual wall (b) when used to guide the rod tip along a square trajectory. By using an artificial potential function emanating from the wall to adjust a weighted Jacobian, the external magnet instead moved along trajectory (c). The measured tip positions (d) are shown for external magnet trajectory (c), with the planned trajectory shown as a solid line (e).

Although we believe that it will be useful to build some redundancy into a magnetic steering system like the one we describe in this paper, inspection of Equation 5.28 suggests that a simple, two-

degree-of-freedom robot can be used to manipulate the external magnet (the advancer provides a third DOF when enabled to translate). For example, the external magnet could be translated within a plane, or gimbaled to rotate about two orthogonal axes.

To explore this, we planned a trajectory for a 2-DOF virtual robot restricted to translate the external magnet in a plane parallel to the xy-plane of the advancer frame, at a height of $12\,\mathrm{cm}$ above the origin of the advancer frame. The trajectory was a trefoil knot space curve, given by the parametric equations

$$\begin{aligned} x &= \beta[\sin(t) + 2\sin(2t)] \\ y &= \beta[\cos(t) - 2\cos(2t)] \\ z &= z_0 - \beta\sin(3t) \end{aligned} \tag{5.51}$$

in which t ranged from 0 to 205 seconds, $\beta = 5 \times 10^{-3}$, and $z_0 = 6\,\mathrm{cm}$. The 2-DOF trajectory of the virtual robot was executed with our 6-DOF robot by solving the inverse kinematics of the 6-DOF robot for the planar external magnet trajectory. Both rod tip position measurements and the planned motion of the external magnet are shown in Figure 5.12.

5.8 Conclusion

Complex, three-dimensional tip trajectories of magnet-tipped rods are attainable by robotically manipulating a permanent magnet. Our approach combined the kinematics of the robot and advancer with a Kirchhoff rod model and a magnetic field model. We linearized the overall system model by computing its Jacobian, and demonstrated accurate trajectory following and obstacle avoidance using resolved-rate motion control.

Our experimental results suggest that open-loop trajectory following may provide sufficient

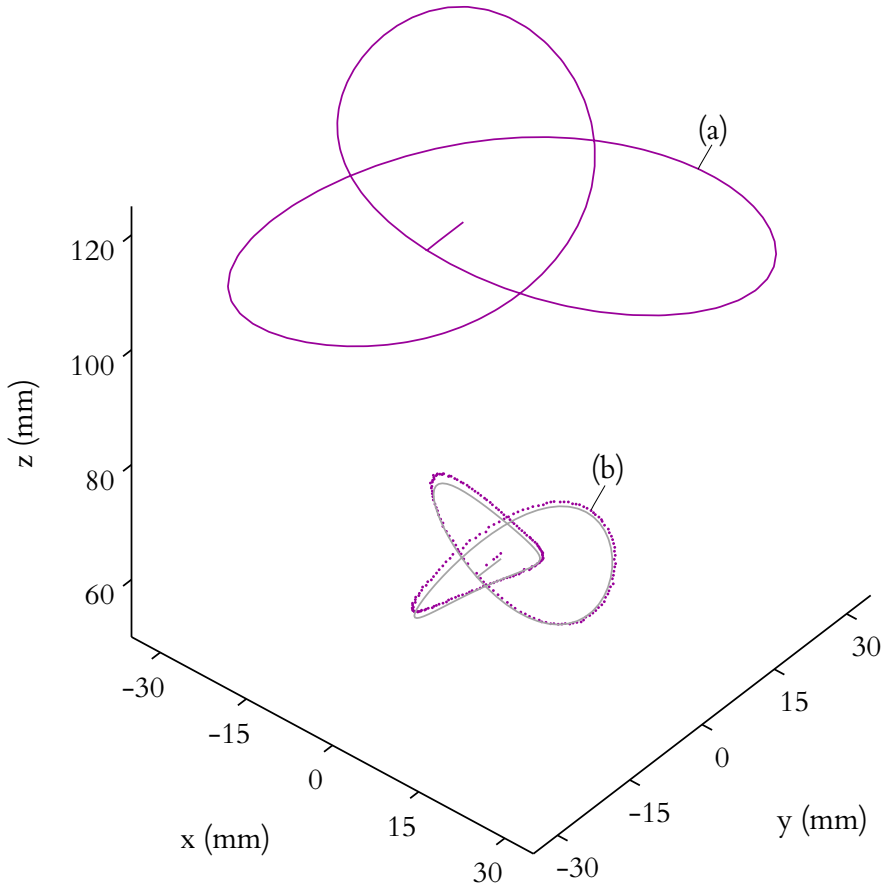

Figure 5.12: (a) To simulate a 2-DOF robot, the external magnet trajectory was restricted to translations within a plane. (b) The rod tip was guided along a trefoil knot trajectory, a three-dimensional space curve.

accuracy for clinical applications, though further analysis is necessary to establish accuracy requirements for specific procedures. Medical imaging, such as fluoroscopy or computed tomography (CT), could provide tip position feedback to improve accuracy using a closed-loop control scheme.

CHAPTER 6

CONCLUSIONS

This dissertation contributed methods, experimental results, and analysis to improve minimally invasive electrode implantation. In this section, we consider the implications of our results, and recommend directions for future work.

6.1 Improvements to Stereotactic Surgery Using Robots

Adjustment of a stereotactic device is a well-defined mechanical task that is suited to automation. The task entails transfer of measurements from software to a physical device, and in this sense resembles many other repetitive industrial tasks for which robots have supplanted human operators, with benefits to the cost, safety, and time required for manufacturing. To realize similar benefits in the operating room, we designed robotic stereotactic systems for the surgical workflows of minimally invasive cochlear implantation surgery and deep brain stimulation surgery. In particular, we designed systems for compatibility with existing trajectory planners and for the special implantation tools used in each surgery.

Prior to our work, miniature stereotactic devices were robotically manufactured by 3D printing and CNC milling. Our designs shifted the robotic task from additive or subtractive *manufacturing* to *automated adjustment-and-locking* of a kinematic structure. Both approaches result in what is essentially a custom-shaped structure, but *automated adjustment-and-locking* requires less time and equipment than manufacturing from bulk material.

In previous applications of robots to stereotactic surgery, the problem of relative motion between the robot and patient was solved by either actively repositioning the robot to compensate for patient motion or by securing the patient and robot to a common structure. We attach pre-adjusted

devices to the same fiducial markers that are used for registration. In this way, we obtain the accuracy advantages of robotic adjustment without the inherent risks of intraoperative robot motion or dangerous movements of the patient's head relative to a robot. For our designs, the surgeon may freely reposition the head as convenient.

The Stewart-Gough 6–6 robot architecture selected for the AIM Frame in Chapter 2 is a versatile design that was found to be suitable for minimally-invasive cochlear implantation, but other robot structures may be considered. A six degree of freedom (DOF) robot is useful for controlling the drill depth and guiding electrodes that have a required angle about the insertion axis, such as self-curling perimodiolar designs. However, it may be advantageous to use a robot structure with fewer DOF to reduce the cost and improve the reliability of the device. For example, with a five DOF robot, the angle of the electrode about the insertion axis could be adjusted manually. A four DOF robot could be used to align a the end effector to some position above the target along the trajectory line, and the drill depth or electrode roll angle could be controlled by setting mechanical stops on the attachable drill press or electrode insertion tool according to this position, respectively (the position along the trajectory is not controllable, but its value can be determined). However, setting adjustable scales is reminiscent of adjusting coordinates on a traditional stereotactic frame, and introduces workflow complexity and opportunity for human error.

The end-effector of the AIM Frame is elevated several centimeters above the surface of the skull. Thus, angular error at end effector is amplified over the trajectory length. This source of error (known as Abbe error or sine error, since it is proportional to the distance multiplied by the sine of the angular error) could be minimized by placing the robot end-effector as close as possible to surface of the skull, which would also be beneficial for minimizing tool deflection. For example, the Gough-Stewart design could be inverted, or a different robot structure could be used.

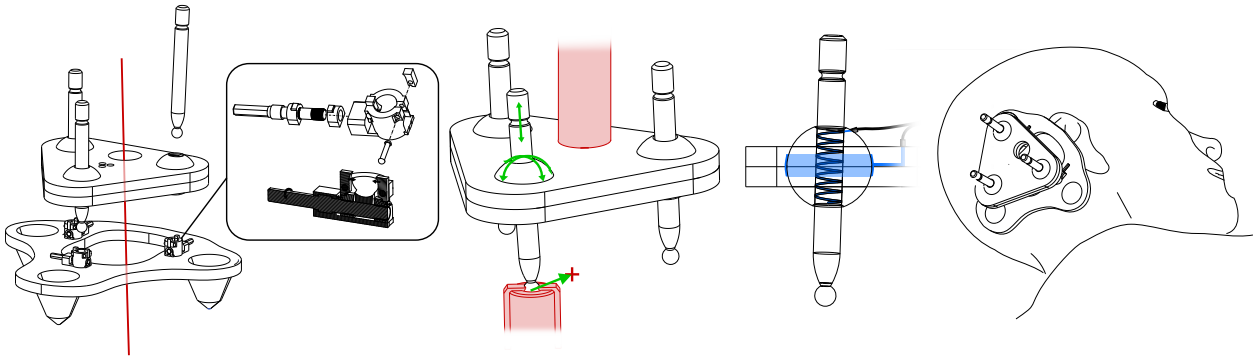

Figure 6.1: Miniature Freeze Frame concept, using pre-positioning frame (PPF) (a) Three captive spheres support sliding rods with spherical tips. The spherical tips lock into gripper mechanisms attached to fixed positions on the PPF. (b) The spherical rod tips are positioned to calculated points by an external robot to adjust the frame (c) Adhesive injection to lock ball and rod (d) Placement on patient for minimally invasive cochlear implantation surgery.

Reducing the size of the Freeze Frame could make it suitable for minimally invasive cochlear implantation surgery or bilateral deep brain stimulation surgery, which uses a separate trajectory for each brain hemisphere. The Freeze Frame was designed for attachment to anchors implanted for bilateral STarFix platforms. The clinical STarFix anchors were spread widely on the top of the head, and there is considerable variation in these anchor positions with respect to the trajectory, as described in the Appendix to Chapter 3. The STarFix anchors were used to ground the design in clinical data, but future iterations of the Freeze Frame concept could be attached to the patient using alternative mechanisms that facilitate a smaller overall design. For example, the conceptual miniature Freeze Frame shown in Figure 6.1 attached to a pre-positioning frame (PPF) similiar to that introduced in Chapter 2 for the AIM Frame. The adjustable "legs" of this device are rods with spherical tips, which slide within captive spheres that rotate within a platform. The spherical rod tips would be positioned by an external robot and then locked into radiolucent gripper mechanisms built into the PPF (metal fiducial spheres, not shown in Figure 6.1, would be embedded in the PPF for registration).

Adhesive locking was proposed for the Freeze Frame because mechanical locking devices,

such as the set screws found on a traditional stereotactic frame, are complicated to automate and rely on forces that may warp a frame. Equipment for automated cyanoacrylate dispensing is widely used in manufacturing, but assuring that the adhesive flows with clinically adequate reliability into joints of a Freeze Frame in an arbitrary configuration will be challenging. Several polymer joining methods may be adaptable to the Freeze Frame concept [167, 168], and could be more convenient. For example, in resistive implant welding [169], a conductive wire or mesh is trapped between two components to be joined. The conductive element is heated by running a current through it, which causes the parts to bond with the conductive mesh in place. Such meshes could be manufactured into the Freeze Frame joints. Other possible methods include laser welding, heated tool welding, and ultrasonic welding. However, several polymer joining methods create fumes and often require pressure to be applied between parts, which could distort the frame and reduce its accuracy.

6.2 Force thresholds in CI surgery

As robotic tools for CI insertion become more viable for clinical use, the data to specify the design and operation of these devices will grow in importance. The mechanical characteristics of intracochlear tissues are difficult to observe without altering supporting structures. We described a protocol for excising fresh cochlea and measuring the rupture force of the intact intracochlear partition. Our specimen preparation method could be extended to test other forms of mechanical trauma, which will be necessary to characterize the interaction of an electrode with intracochlear structures.

The biomechanics of the cochlea have been extensively studied prior to our work, but with an aim of understanding sound transduction and disease, rather than the failure analysis that was the focus of our work. Our empirical results could be given a broader interpretation by relating them to mechanical models of tissues in the intracochlear partition.

Our results suggest that surgeons can perceive intracochlear rupture forces, but further research

is needed to understand perception under the more complicated force loadings than the sudden onset of force applied by Semmes–Weinstein monofilaments in our experiments. Future experimental designs could use haptic devices to apply force profiles that closely resemble a full cochlear implant insertion, but the fatigue of participants should be considered. The staircase testing procedure we described required approximately 30 minutes per participant, and the surgeons who participated expressed relief at the conclusion of testing. A portable testing apparatus such as we have introduced will be useful for testing at a site chosen by participants or at a professional gathering.

6.3 Guiding magnet-tipped electrodes

We described methods for guiding electrodes and other rod-shaped instruments along three-dimensional trajectories using a robot-mounted external magnet as a field source. Our approach requires considerably less equipment and energy than the large field sources that are now used clinically to guide magnetic catheters. Furthermore, we have demonstrated the most accurate, open loop control of a magnet-tipped rod to date.

One notable advantage of magnet-tipped electrodes is that no mechanical components are required along the length of the electrode. Thus, existing electrodes can be adapted without modifying their internal structures; only one magnet needs to be attached to the tip. This aspect facilitates use of very thin rods, such as the 240 μm diameter optical fiber used in our experiments. Our approach could be used with considerably thinner rods to perform dexterous procedures in previously inaccessible, small cavities of the human body.

The Kirchhoff rod model we described could aid further design and analysis. This versatile rod model can be extended to include effects such as forces from fluids or contacting tissues, as would be useful to avoid trauma during electrode implantation, for example. In future work, our model may serve as a benchmark for low-order rod models which may be suited to real-time planning and control

algorithms.

We demonstrated tip guidance using both redundant and non-redundant external robots. Redundancy may be useful to fulfill several secondary goals. We focused on obstacle avoidance, but the technique could be expanded to avoid joint limits or singularities of the external robot, for example. Alternatively, we showed that a minimal, two-degree-of-freedom robot could be used, pointing the way to range of simple and compact robot designs for manipulating the external magnet. We anticipate that design choices such as we have noted here will be resolved by particular applications.

The glass optical fiber rod we used in experiments was chosen for its homogeneous material properties and constant second moment of area. A constant second moment of area made the rod easy to calibrate. Similar rods could be used for many magnetic guidance applications, such as biopsy needles or steerable endoscopes. It will be more challenging to calibrate existing devices such as cochlear implant electrode arrays, which are made of both silicone and a complicated structure of platinum-iridium wires and individual electrodes. These devices can also exhibit elastic-plastic bending, which is not considered in most expositions of Kirchhoff rod theory. Successful magnetic guidance of a cochlear implant electrode array may benefit from closed-loop control that relies on fusion of multiple sources of feedback, perhaps using a particle filter, unscented Kalman filter, or related probabilistic control method that can handle uncertainty in both the Kirchhoff rod model and sensing channels. The feedback sources could include intraoperative fluoroscopy, insertion force measurements, and intraoperative impedance.

6.4 Outlook

Our work extends the abilities of the surgeon, enabling greater control over the placement of an electrode and simplifying the surgical workflow for implantation. We have added to the understanding of surgical trauma, and taken first steps toward measuring and mitigating some of its causes. Work remains to transform the concepts present here into tangible benefits for patients.

APPENDICES

Appendix to Chapter 3: Analysis of a Large Clinical Anchor Dataset

In Section 3.2, we analyzed anchor positions from ten surgeries performed with the STarFix platform to choose design specifications for the Freeze Frame. After designing and testing the Freeze Frame, we obtained planning data from 1052 DBS surgeries performed with the STarFix microstereotactic frame. In this Appendix, we test if the Freeze Frame can be adjusted to fit the planning data in this set, and examine if the spherical pattern of fiducials described in Section 3.2 is evident in this large dataset.

Table 6.1: The dataset was divided into six subsets, and a sphere was fit to each subset using a least-squares (LS) method. The standard deviation (SD) of the residual distributions describes the variation in fiducial positions in the radial direction. All dimensions are in mm.

Frame Design	Side	n	Trajectory Length	LS sphere radius	SD of residuals	Freeze Frame % reached
a	Left	307	130	96.09	5.77	100.0
a	Right	307	130	95.94	5.80	99.7
b	Left	555	120	100.38	7.30	95.3
b	Right	555	120	97.44	6.87	93.7
b	Left	190	130	93.05	7.28	94.7
b	Right	190	130	93.05	7.26	97.5

The dataset was provided by FHC corporation, manufacturer of the STarFix frame. The basic element of the dataset was a frame, which included all of the de-identified information from the WayPoint Planner software that we analyzed in Section 3.2, namely anchor positions, the directions of the anchors, the ACPC line, the target, and the electrode trajectory. However, each frame in the dataset includes two trajectories and two targets, as these frames were designed for bilateral electrode insertion, with an attachment port for an electrode insertion device on both the left and right sides of the head. We are presently concerned with designing adjustable frames for unilateral electrode insertion, which is the predominate method in DBS surgery. To relate the data to unilateral frame design, we duplicated

the anchor positions for each frame, and assigned the left trajectory to one set of duplicated anchors, and the right to the other. Thus, we analyze the data as if 2104 unilateral surgeries were performed. We further subdivided the data according to the frame design and the electrode length used in the surgeries. The two frame designs included in the dataset are shown in Figure 6.2, and the six subsets we analyzed are listed in Table 6.1.

To prepare the data for analysis, we transformed all the patient data to the single coordinate system described in Section 3.2, and determined where the spherical fiducials that we described in Section 3.2 would be located with respect to the anchors. The Freeze Frame was then virtually adjusted to attach to each fiducial subset. We assumed that the cylindrical shaft component of the leg was 15 cm (5 cm longer than the Freeze Frame shown in Chapter 3). The percent of frames that were in reach of the Freeze Frame are also listed in Table 6.1.

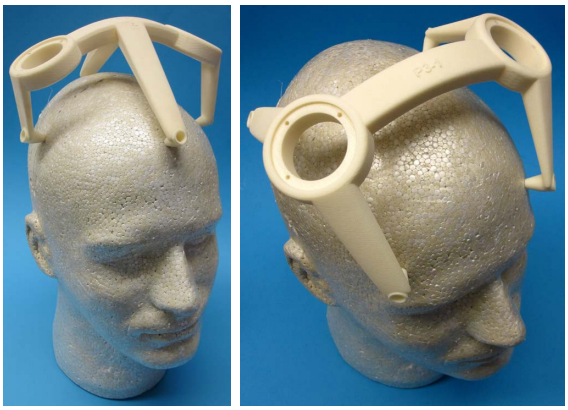

(a) (b)

Figure 6.2: Anchor positions in the dataset were recorded from surgeries performed with two different STarFix frame designs. Design (a): two anchors lie approximately on the sagittal plane, two on the coronal. Design (b): two anterior anchors are spread away from the sagittal plane, as are two posterior anchors.

We observed in Section 3.2 that fiducials appeared to lie close to a spherical surface when transformed to single coordinate system. To test if this pattern holds for the larger data set, we fit a sphere to all the fiducial positions in each subset, which are grouped into $\mathbf{x}_i \in \mathbb{R}^3$, where $i = 1 \ldots 4n$

(there are four implantation regions on the skull). Let $\mathbf{c} \in \mathbb{R}^3$ denote the position of the sphere center and $r \in \mathbb{R}$ denote the sphere's radius. The least-squares objective function [170]

$$\arg\min_{\mathbf{c},r} \left(\sum_{i=1}^{4n} \|\mathbf{x}_i - \mathbf{c}\| - r \right)^2 \tag{6.1}$$

was minimized to find $\mathbf{c}$ and r using the Matlab function `lsqnonlin` with a Levenberg-Marquardt algorithm. Results of this nonlinear least squares sphere fit are summarized in Table 6.1. The least squares sphere fits for all six subsets are shown in 6.3. The positions of the spherical fiducials are closely approximated by a spherical surface.

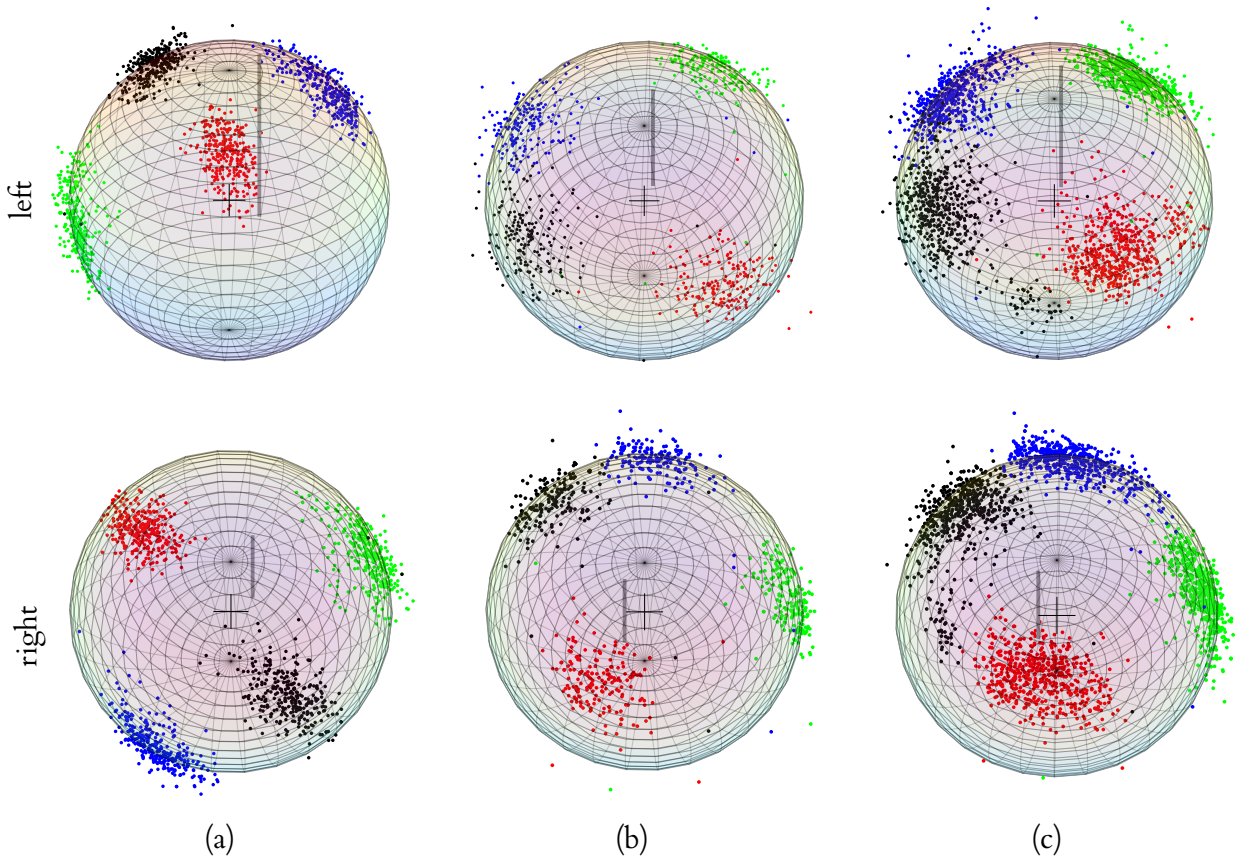

Figure 6.3: Fiducial positions from each subsect of the STarFix dataset all lie approximately on a sphere, which we fit to the data using a nonlinear least-squares method. (a) Least-squares sphere fits to the left and right trajectory interpretations of fiducials corresponding to frame design a. (b) sphere fits for frame design b, 120 mm trajectory subset. (c) Frame design b, 130 mm trajectory subset.

Chapter 4 Appendix: force threshold testing script

Thank you for participating.

This experiment will involve you placing your arm through this curtain to prevent you from being able to see what's on the other side. When it's time to start, you should rest your dominant arm in a comfortable position through the hole in the curtain.

You will be handed Monofilament devices. Each trial will consist of two devices (a pair). You will be handed these one at a time. I will hand you a device, and place the tip on a starting block at a

fixed height. This will ensure correct positioning and orientation. When you are ready, I will slide the starting block away so that you are holding the device without support. At this time, you should advance the filament straight down, at a speed that you would normally insert a cochlear implant into a cochleostomy. You should advance continuously downward, without stopping or backing up, until you reach a mechanical stop that prevents you from advancing any further. While you are advancing, you should make note of whether or not you feel the filament tip touch the surface prior to reaching the stop. You should not tell me whether or not you feel anything.

I will then take the first device from your hand, and hand you the second device of the trial. I will again place it on the starting block. You will perform the exact same task, moving downward at a continuous speed until hitting the mechanical stop, and take note of whether or not you feel a filament touch prior to stopping.

In each pair, one of the devices will contain a filament that does touch, and the other will have no filament, and therefore not make any contact at all. After you complete the pair, I will ask you,"which one did you feel, the first one, or the second one?". You must decide (even if it's a guess), which one you think you felt, and which one you didn't.

Do you have any questions about the experiment or what you'll be asked to do?

We will then repeat this with several other pairs of filaments. Each pair will be done in a random order. For example, sometimes the first device will have no filament, and sometimes the second device will have no filament.

Communication between us during the experiment will be limited. I will speak only to tell you information about the tasks being performed (i.e., "now I'm going to hand you the next filament"),

and to ask which filament you felt. You should only answer my questions. I will not be able to answer any additional questions for you during the experiment, so if you have any questions prior to starting, please let me know now.

Do you have any additional questions?

You'll now have 30 seconds to see one of the filaments and practice compressing it on a flat surface. This is so that you can have an idea of what you're feeling for.

If you don't have any further questions, we'll begin.

Chapter 5 Appendix: Permanent Magnet Field Models

A permanent magnet establishes a three-dimensional magnetic field $\mathbf{B}$. To approximate $\mathbf{B}$ with the point-dipole model, a coordinate frame is placed at the magnet center. Let $\mathbf{a}$ be a vector from the dipole to the point of observation, and $\hat{\mathbf{a}}$ a unit vector in the direction of $\mathbf{a}$, then

$$\mathbf{B}(\mathbf{a}) = \frac{\mu_0}{4\pi}\left(\frac{3\hat{\mathbf{a}}(\hat{\mathbf{a}}\cdot\mathbf{m}) - \mathbf{m}}{\|\mathbf{a}\|^3}\right) \tag{6.2}$$

in which $\mu_0 = 4\pi \times 10^{-7}$ H/m is the vacuum permeability constant, and $\mathbf{m}$ is the magnet's dipole moment. See [171, Ch. 5] for derivation.

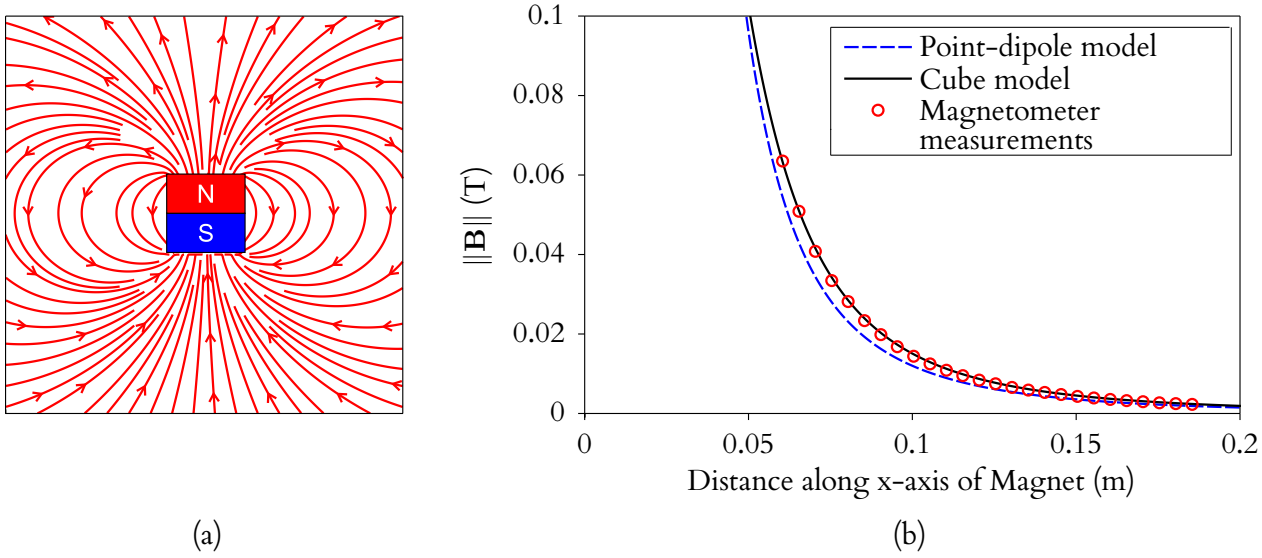

Figure 6.4: (a) A planar slice of the three-dimensional vector field of a cube magnet, shown as streamlines. (b) Measurements of the magnitude $\|\mathbf{B}_x\|$ of the cube magnet used in experiments, taken with a Hall-effect magnetometer, are shown with the field magnitude simulated using the point-dipole and cube models.

Furlani [143, Ch. 4] presented a closed-form solution for the magnetic field of a cuboid magnet. A Cartesian coordinate system is fixed at the centroid of the magnet volume, with the faces of the magnet orthogonal to the coordinate axes. The distances of the faces from the origin are given in

pairs, where subscript 1 denotes a negative distance and subscript 2 denotes a positive distance: (x_1, x_2), (y_1, y_2), (z_1, z_2). The volume is uniformly magnetized along the z-axis, and has a residual magnetization $M = \|\mathbf{M}\|$. At a point (x, y, z), the x component of the field is given by

$$B_x(x, y, z) = \sum_{k=1}^{2} \sum_{m=1}^{2} \frac{\mu_0 M}{4\pi} (-1)^{k+m} \ln(F) \tag{6.3}$$

in which

$$F(x, y, z, x_m, y_1, y_2, z_k) = \frac{(y - y_1) + [(x - x_m)^2 + (y - y_1)^2 + (z - z_k)^2]^{1/2}}{(y - y_2) + [(x - x_m)^2 + (y - y_2)^2 + (z - z_k)^2]^{1/2}} \tag{6.4}$$

The y component is given by

$$B_y(x, y, z) = \sum_{k=1}^{2} \sum_{m=1}^{2} \frac{\mu_0 M}{4\pi} (-1)^{k+m} \ln(H) \tag{6.5}$$

in which

$$H(x, y, z, x_1, x_2, y_m, z_k) = \frac{(x - x_1) + [(x - x_1)^2 + (y - y_m)^2 + (z - z_k)^2]^{1/2}}{(x - x_2) + [(x - x_2)^2 + (y - y_m)^2 + (z - z_k)^2]^{1/2}} \tag{6.6}$$

and the z component is given by

$$B_z(x, y, z) = \frac{\mu_0 M}{4\pi} \sum_{k=1}^{2} \sum_{n=1}^{2} \sum_{m=1}^{2} (-1)^{k+n+m} \times \tan^{-1}\Big[\frac{(x - x_n)(y - y_m)}{(z - z_k)} G\Big] \tag{6.7}$$

in which

$$G(x, y, z, x_n, y_m, z_k) = \frac{1}{[(x - x_n)^2 + (y - y_m)^2 + (z - z_k)^2]^{1/2}} \tag{6.8}$$

BIBLIOGRAPHY

[1] B. S. Wilson and M. F. Dorman, "Cochlear implants: current designs and future possibilities," *Journal of Rehabilitation Research & Development*, vol. 45, no. 5, pp. 695–730, 2008.

[2] B. K. Swenor, P. Y. Ramulu, J. R. Willis, D. Friedman, and F. R. Lin, "The prevalence of concurrent hearing and vision impairment in the united states," *JAMA internal medicine*, vol. 173, no. 4, pp. 312–313, 2013.

[3] P. Gildenberg, "General concepts of stereotactic surgery," in *Modern Stereotactic Neurosurgery* (L. Lunsford, ed.), vol. 1 of *Topics in neurological surgery*, pp. 3–11, Springer US, 1988.

[4] M. Rahman, G. J. Murad, and J. Mocco, "Early history of the stereotactic apparatus in neurosurgery," *Neurosurgical focus*, vol. 27, no. 3, p. E12, 2009.

[5] A. M. Lozano, P. L. Gildenberg, and R. R. Tasker, *Textbook of stereotactic and functional neurosurgery*, vol. 1. Springer Berlin, 2009.

[6] M. Schulder, *Handbook of stereotactic and functional neurosurgery*, vol. 58. Informa Healthcare, 2003.

[7] S. H. Greenblatt, *A history of neurosurgery: in its scientific and professional contexts*. Amer Assn of Neurological Surgeons, 1997.

[8] J. Flickinger, L. Lunsford, D. Kondziolka, and A. Maitz, "Potential human error in setting stereotactic coordinates for radiosurgery: implications for quality assurance," *International Journal of Radiation Oncology Biology Physics*, vol. 27, no. 2, pp. 397–401, 1993.

[9] G. Widmann, P. Schullian, M. Ortler, and R. Bale, "Frameless stereotactic targeting devices:

technical features, targeting errors and clinical results," *The International Journal of Medical Robotics and Computer Assisted Surgery*, vol. 8, no. 1, pp. 1–16, 2012.

[10] D. A. Orringer, A. Golby, and F. Jolesz, "Neuronavigation in the surgical management of brain tumors: current and future trends," *Expert Review of Medical Devices*, vol. 9, no. 5, pp. 491–500, 2012.

[11] Y. Kwoh, I. Reed, J. Chen, H. Shao, T. Truong, and E. Jonckheere, "A new computerized tomographic-aided robotic stereotaxis system," *Robotics Age*, vol. 7, no. 6, pp. 17–22, 1985.

[12] Y. S. Kwoh, J. Hou, E. A. Jonckheere, and S. Hayati, "A robot with improved absolute positioning accuracy for ct guided stereotactic brain surgery," *Biomedical Engineering, IEEE Transactions on*, vol. 35, no. 2, pp. 153–160, 1988.

[13] J. Troccaz, ed., *Medical Robotics*. John Wiley & Sons, 2012.

[14] R. A. Beasley, "Medical robots: Current systems and research directions," *Journal of Robotics*, vol. 2012, 2012.

[15] M. Shoham, M. Burman, E. Zehavi, L. Joskowicz, E. Batkilin, and Y. Kunicher, "Bone-mounted miniature robot for surgical procedures: concept and clinical applications," *IEEE Transactions on Robotics and Automation*, vol. 19, no. 5, pp. 893–901, 2003.

[16] J. M. Fitzpatrick, P. E. Konrad, C. Nickele, E. Cetinkaya, and C. Kao, "Accuracy of customized miniature stereotactic platforms," *Stereotactic and functional neurosurgery*, vol. 83, no. 1, pp. 25–31, 2005.

[17] R. J. Maciunas, R. L. J. Galloway, J. Latimer, C. Cobb, E. Zaccharias, A. Moore, and V. R. Mandava *Stereotactic Funct. Neurosurg.*, vol. 58, pp. 103–107, 1992.

[18] R. J. Maciunas, R. L. Galloway Jr, and J. W. Latimer, "The application accuracy of stereotactic frames," *Neurosurgery*, vol. 35, no. 4, pp. 682–695, 1994.

[19] T. Varma and P. Eldridge, "Use of the neuromate stereotactic robot in a frameless mode for functional neurosurgery," *The International Journal of Medical Robotics and Computer Assisted Surgery*, vol. 2, no. 2, pp. 107–113, 2006.

[20] S. Ferrand-Sorbets, M. Delphine Taussig, M. Fohlen, C. Bulteau, G. Dorfmuller, and O. Delalande, "Frameless stereotactic robot-guided placement of depth electrodes for stereo-electroencephalography in the presurgical evaluation of children with drug-resistant focal epilepsy," in *CNS Annual Meeting*, 2010.

[21] D. P. Devito, L. Kaplan, R. Dietl, M. Pfeiffer, D. Horne, B. Silberstein, M. Hardenbrook, G. Kiriyanthan, Y. Barzilay, A. Bruskin, *et al.*, "Clinical acceptance and accuracy assessment of spinal implants guided with spineassist surgical robot: retrospective study," *Spine*, vol. 35, no. 24, pp. 2109–2115, 2010.

[22] R. Balachandran, J. E. Mitchell, B. M. Dawant, and J. M. Fitzpatrick, "Accuracy evaluation of microTargeting platforms for deep-brain stimulation using virtual targets," *IEEE Transactions on Biomedical Engineering*, vol. 56, pp. 37–44, January 2009.

[23] L. B. Kratchman, G. S. Blachon, T. J. Withrow, R. Balachandran, R. F. Labadie, and R. J. Webster III, "Design of a bone-attached parallel robot for percutaneous cochlear implantation," *Biomedical Engineering, IEEE Transactions on*, vol. 58, no. 10, pp. 2904–2910, 2011.

[24] L. B. Kratchman and J. M. Fitzpatrick, "Robotically-adjustable microstereotactic frames for image-

guided neurosurgery," in *SPIE Medical Imaging*, pp. 86711U–86711U, International Society for Optics and Photonics, 2013.

[25] R. F. Labadie, R. Balchandran, J. E. Mitchell, J. H. Noble, O. Majdani, D. S. Haynes, M. L. Bennett, B. M. Dawant, and J. M. Fitzpatrick, "Clinical validation study of percutaneous cochlear access using patient-customized microstereotactic frames," *Otology & Neurotology*, vol. 31(1), no. 1, pp. 94–99, 2010.

[26] R. Balachandran, J. E. Mitchell, G. S. Blachon, J. H. Noble, B. M. Dawant, J. M. Fitzpatrick, and R. F. Labadie, "Percutaneous cochlear implant drilling via customized frames: An in vitro study," *Otolaryngology-Head and Neck Surgery*, vol. 142, no. 3, pp. 421–426, 2010.

[27] R. F. Labadie, J. E. Mitchell, R. Balachandran, and J. M. Fitzpatrick, "Customized, rapid-production microstereotactic table for surgical targeting: description of concept and in vitro validation," *International Journal of Computer Assisted Radiology and Surgery*, vol. 4, no. 3, pp. 273–280, 2009.

[28] J. H. Noble, B. M. Dawant, F. M. Warren, and R. F. Labadie, "Automatic identification and 3D rendering of temporal bone anatomy," *Otology & Neurotology*, vol. 30, no. 4, pp. 436–442, 2009.

[29] J. H. Noble, F. M. Warren, R. F. Labadie, and B. M. Dawant, "Automatic segmentation of the facial nerve and chorda tympani in ct images using spatially dependent feature values," *Medical Physics*, vol. 35, no. 12, pp. 5375–5384, 2008.

[30] J. H. Noble, F. M. Warren, R. F. Labadie, B. Dawant, and J. M. Fitzpatrick, "Determination of drill paths for percutaneous cochlear access accounting for target positioning error," in *Proceedings of SPIE*, vol. 6509, pp. 251–263, 2007.

[31] D. Schurzig, R. F. Labadie, A. Hussong, T. S. Rau, and R. J. Webster III, "Design of a Tool

Integrating Force Sensing with Automated Insertion in Cochlear Implantation," *IEEE/ASME Transactions on Mechatronics*, vol. 17, no. 2, pp. 381–389, 2012.

[32] L. B. Kratchman, D. Schurzig, T. R. McRackan, R. Balachandran, J. H. Noble, R. J. Webster III, and R. F. Labadie, "A Manually-Operated, Advance Off-Stylet Insertion Tool for Image-Guided, Minimally Invasive Cochlear Implantation Surgery," *IEEE Transactions on Biomedical Engineering*, vol. 59, no. 10, pp. 2792–2800, 2012.

[33] T. McRackan, R. Balachandran, J. H. Noble, D. Schurzig, G. S. Blachon, J. E. Mitchell, B. M. Dawant, J. M. Fitzpatrick, and R. F. Labadie, "In-vitro validation of percutaneous cochlear implantation," in *2011 Association for Research in Otolaryngology*, (Baltimore, MD), Feb. 2011.

[34] O. Majdani, T. A. Schuman, D. S. Haynes, M. S. Dietrich, M. Leinung, T. Lenarz, and R. F. Labadie, "Time of cochlear implant surgery in academic settings," *Otolaryngology - Head and Neck Surgery*, vol. 142, no. 2, pp. 254–259, 2010.

[35] W. Sukovich, S. Brink-Danan, and M. Hardenbrook, "Miniature robotic guidance for pedicle screw placement in posterior spinal fusion: early clinical experience with the SpineAssist®," *The International Journal of Medical Robotics and Computer Assisted Surgery*, vol. 2, no. 2, pp. 114–122, 2006.

[36] L. Joskowicz, R. Shamir, M. Freiman, M. Shoham, E. Zehavi, F. Umansky, and Y. Shoshan, "Image-guided system with miniature robot for precise positioning and targeting in keyhole neurosurgery," *Computer Aided Surgery*, vol. 11, no. 4, p. 181, 2006.

[37] R. Shamir, Z. Israel, M. Shoham, L. Joskowicz, and Y. Shohan, "Renaissance robotic system for

keyhole cranial neurosurgery: in vitro accuracy study," *International Journal of Computer Assisted Radiology and Surgery*, vol. 6, pp. 82–89, 2011.

[38] C. Plaskos, P. Cinquin, S. Lavallee, and A. J. Hodgson, "Praxiteles: a miniature bone-mounted robot for minimal access total knee arthroplasty," *International Journal of Medical Robotics and Computer Assisted Surgery*, vol. 1, no. 4, pp. 67–79, 2005.

[39] S. Song, A. Mor, and B. Jaramaz, "HyBAR: hybrid bone-attached robot for joint arthroplasty," *The International Journal of Medical Robotics and Computer Assisted Surgery*, vol. 5, no. 2, pp. 223–231, 2009.

[40] A. Wolf, B. Jaramaz, B. Lisien, and A. M. DiGioia, "MBARS: mini bone-attached robotic system for joint arthroplasty," *The International Journal of Medical Robotics and Computer Assisted Surgery*, vol. 1, no. 2, pp. 101–121, 2005.

[41] F. Maes, A. Collignon, D. Vandermeulen, G. Marchal, and P. Suetens, "Multimodality image registration by maximization of mutual information," *IEEE Transactions on Medical Imaging*, vol. 16, no. 2, pp. 187–198, 1997.

[42] D. Henderson, "Simple Ceramic Motor ... Inspiring Smaller Products," in *Actuator 2006: 10th International Conference on New Actuators*, (Bremen, Germany), pp. 1–4, 2006.

[43] J. Merlet, *Parallel robots*. Springer-Verlag New York Inc, 2006.

[44] J.-P. Merlet and D. Daney, "Legs interference checking of parallel robots over a given workspace or trajectory," in *Robotics and Automation, 2006. Proceedings 2006 IEEE International Conference on*, pp. 757–762, IEEE, 2006.

[45] L. Tsai, *Robot analysis: the mechanics of serial and parallel manipulators*. Wiley-Interscience, 1999.

[46] J. M. Fitzpatrick, D. L. G. Hill, and C. R. Maurer, "Image registration," in *Handbook of Medical Imaging* (M. Sonka and J. Fitzpatrick, eds.), vol. II, ch. 8, pp. 447–513, Bellingham, WA: SPIE, 2000.

[47] B. Bell, N. Gerber, T. Williamson, K. Gavaghan, W. Wimmer, M. Caversaccio, and S. Weber, "In vitro accuracy evaluation of image-guided robot system for direct cochlear access," *Otology & Neurotology*, vol. 34, no. 7, pp. 1284–1290, 2013.

[48] B. Schrader, W. Hamel, D. Weinert, and H. Mehdorn, "Documentation of electrode localization," *Movement disorders*, vol. 17, no. S3, pp. S167–S174, 2002.

[49] H. Bjartmarz and S. Rehncrona, "Comparison of accuracy and precision between frame-based and frameless stereotactic navigation for deep brain stimulation electrode implantation," *Stereotactic and functional neurosurgery*, vol. 85, no. 5, pp. 235–242, 2007.

[50] K. Holloway, S. Gaede, P. Starr, J. Rosenow, V. Ramakrishnan, and J. Henderson, "Frameless stereotaxy using bone fiducial markers for deep brain stimulation," *Journal of neurosurgery*, vol. 103, no. 3, pp. 404–413, 2005.

[51] D. Rajon, F. Bova, and W. Friedman, "Rapid fabrication of custom patient biopsy guides," *Journal of Applied Clinical Medical Physics*, vol. 10, no. 4, pp. 260–272, 2009.

[52] J. Kobler, J. Kotlarski, J. Öltjen, S. Baron, and T. Ortmaier, "Design and analysis of a head-mounted parallel kinematic device for skull surgery," *International journal of computer assisted radiology and surgery*, vol. 7, no. 1, pp. 137–149, 2012.

[53] J. P. Thiran, R. Charrier, and D. Haag, "The stereopod: an accurate guidance system for frameless stereotactic neurosurgery," in *CARS 2010*, 2010.

[54] A. Slocum, "Kinematic couplings for precision fixturing, part 1: Formulation of design parameters," *Precision Engineering*, vol. 10, no. 2, pp. 85–91, 1988.

[55] A. Slocum and A. Donmez, "Kinematic couplings for precision fixturing, part 2: Experimental determination of repeatability and stiffness," *Precision engineering*, vol. 10, no. 3, pp. 115–122, 1988.

[56] M. Sonka and J. M. Fitzpatrick, *Medical Image Processing and Analysis, Volume II of the Handbook of Medical Imaging*. SPIE Press, 2000.

[57] J. M. Fitzpatrick, R. Balachandran, and G. S. Blachon, "Accuracy validation of waypoint planner localization for microtable locator spheres," tech. rep., Vanderbilt University, Dec 2012.

[58] J. M. Fitzpatrick, J. B. West, and C. R. Maurer Jr., "Predicting error in rigid-body point-based registration," *Medical Imaging, IEEE Transactions on*, vol. 17, no. 5, pp. 694–702, 1998.

[59] K. Mardia and P. Jupp, *Directional statistics*, vol. 494. Wiley, 2009.

[60] B. Mangus, A. Rivas, B. S. Tsai, D. S. Haynes, and J. T. Roland Jr, "Surgical techniques in cochlear implants," *Otolaryngologic Clinics of North America*, vol. 45, no. 1, pp. 69–80, 2012.

[61] R. Brito, T. A. Monteiro, A. F. Leal, R. K. Tsuji, M. H. Pinna, and R. F. Bento, "Surgical complications in 550 consecutive cochlear implantation," *Brazilian journal of otorhinolaryngology*, vol. 78, no. 3, pp. 80–85, 2012.

[62] A. Aschendorff, J. Kromeier, T. Klenzner, and R. Laszig, "Quality control after insertion of the nucleus contour and contour advance electrode in adults," *Ear and Hearing*, vol. 28, no. 2, pp. 75S–79S, 2007.

[63] M. W. Skinner, T. A. Holden, B. R. Whiting, A. H. Voie, B. Brunsden, J. G. Neely, E. A. Saxon, T. E. Hullar, and C. C. Finley, "In vivo estimates of the position of advanced bionics electrode

arrays in the human cochlea.," *The Annals of otology, rhinology & laryngology. Supplement*, vol. 116(4), pp. 2–24, 2007.

[64] C. C. Finley, T. A. Holden, L. K. Holden, B. R. Whiting, R. A. Chole, G. J. Neely, T. E. Hullar, and M. W. Skinner, "Role of electrode placement as a contributor to variability in cochlear implant outcomes," *Otology & Neurotology*, vol. 29, no. 7, pp. 920–928, 2008.

[65] G. B. Wanna, J. H. Noble, M. L. Carlson, R. H. Gifford, M. S. Dietrich, D. S. Haynes, B. M. Dawant, and R. F. Labadie, "Impact of electrode design and surgical approach on scalar location and cochlear implant outcomes," *The Laryngoscope*, vol. 124, no. S6, pp. S1–S7, 2014.

[66] O. Adunka and J. Kiefer, "Impact of electrode insertion depth on intracochlear trauma," *Otolaryngology-Head and Neck Surgery*, vol. 135, no. 3, pp. 374–382, 2006.

[67] T. Ishii, M. Takayama, and Y. Takahashi, "Mechanical properties of human round window, basilar and reissner's membranes," *Acta Oto-Laryngologica*, vol. 115, no. S519, pp. 78–82, 1995.

[68] M. Carlson, C. Driscoll, R. Gifford, N. Tombers, B. Hughes-Borst, B. Neff, C. Beatty, *et al.*, "Implications of minimizing trauma during conventional cochlear implantation," *Otology & Neurotology*, vol. 32, no. 6, pp. 962–968, 2011.

[69] O. Majdani, D. Schurzig, A. Hussong, T. Rau, J. Wittkopf, T. Lenarz, and R. F. Labadie, "Force measurement of insertion of cochlear implant electrode arrays in vitro: comparison of surgeon to automated insertion tool," *Acta oto-laryngologica*, vol. 130, no. 1, pp. 31–36, 2010.

[70] D. Schurzig, R. J. Webster III, M. S. Dietrich, and R. F. Labadie, "Force of cochlear implant electrode insertion performed by a robotic insertion tool: comparison of traditional versus advance off-stylet techniques," *Otology & Neurotology*, vol. 31, no. 8, pp. 1207–1210, 2010.

[71] L. A. Jones and H. Z. Tan, "Application of psychophysical techniques to haptic research," *Haptics, IEEE Transactions on*, vol. 6, no. 3, pp. 268–284, 2013.

[72] F. Kingdom and N. Prins, "Psychophysics: a practical introduction," 2010.

[73] G. A. Gescheider, *Psychophysics: the fundamentals*. Psychology Press, 2013.

[74] N. Prins *et al.*, *Psychophysics: a practical introduction*. Academic Press, 2009.

[75] M. R. Leek, "Adaptive procedures in psychophysical research," *Perception & psychophysics*, vol. 63, no. 8, pp. 1279–1292, 2001.

[76] M. A. Garcia-Perez, "Forced-choice staircases with fixed step sizes: asymptotic and small-sample properties," *Vision research*, vol. 38, no. 12, pp. 1861–1881, 1998.

[77] H. Levitt, "Transformed up-down methods in psychoacoustics," *The Journal of the Acoustical society of America*, vol. 49, no. 2B, pp. 467–477, 2005.

[78] L. A. Jones, "Perception of force and weight: theory and research.," *Psychological bulletin*, vol. 100, no. 1, p. 29, 1986.

[79] L. A. Jones and S. J. Lederman, *Human hand function*. Oxford University Press, 2006.

[80] J. Bell-Krotoski and E. Tomancik, "The repeatability of testing with semmes-weinstein monofilaments," *The Journal of hand surgery*, vol. 12, no. 1, pp. 155–161, 1987.

[81] V. F. Voerman, J. van Egmond, and B. J. Crul, "Normal values for sensory thresholds in the cervical dermatomes: A critical note on the use of semmes-weinstein monofilaments," *American journal of physical medicine & rehabilitation*, vol. 78, no. 1, pp. 24–29, 1999.

[82] J. Dosher and B. Hannaford, "Human interaction with small haptic effects," *Presence: Teleoperators and Virtual Environments*, vol. 14, no. 3, pp. 329–344, 2005.

[83] H. H. King, R. Donlin, and B. Hannaford, "Perceptual thresholds for single vs. multi-finger haptic interaction," in *Haptics Symposium, 2010 IEEE*, pp. 95–99, IEEE, 2010.

[84] G. Baud-Bovy and E. Gatti, "Hand-held object force direction identification thresholds at rest and during movement," in *Haptics: Generating and Perceiving Tangible Sensations*, pp. 231–236, Springer, 2010.

[85] W. E. C. on Leprosy and W. H. Organization, *WHO Expert Committee on Leprosy: Seventh Report*, vol. 874. World Health Organization, 1998.

[86] M. H. Haloua, I. Sierevelt, and W. J. Theuvenet, "Semmes-weinstein monofilaments: influence of temperature, humidity, and age," *The Journal of hand surgery*, vol. 36, no. 7, pp. 1191–1196, 2011.

[87] M. J. Mueller, "Identifying patients with diabetes mellitus who are at risk for lower-extremity complications: use of semmes-weinstein monofilaments," *Physical Therapy*, vol. 76, no. 1, pp. 68–71, 1996.

[88] E. H. Tracey, A. J. Greene, and R. L. Doty, "Optimizing reliability and sensitivity of semmes–weinstein monofilaments for establishing point tactile thresholds," *Physiology & behavior*, vol. 105, no. 4, pp. 982–986, 2012.

[89] M. Zhou, J. Perreault, S. Schwaitzberg, and C. Cao, "Effects of experience on force perception threshold in minimally invasive surgery," *Surgical endoscopy*, vol. 22, no. 2, pp. 510–515, 2008.

[90] N. Gurari and G. Baud-Bovy, "Customization, control, and characterization of a commercial

haptic device for high-fidelity rendering of weak forces," *Journal of neuroscience methods*, vol. 235, pp. 169–180, 2014.

[91] N. van de Berg, D. van Gerwen, J. Dankelman, and J. van den Dobbelsteen, "Design choices in needle steering;a review," *IEEE/ASME Transactions on Mechatronics*, In Press.

[92] Y. Fu, H. Liu, W. Huang, S. Wang, and Z. Liang, "Steerable catheters in minimally invasive vascular surgery," *The International Journal of Medical Robotics and Computer Assisted Surgery*, vol. 5, no. 4, pp. 381–391, 2009.

[93] F. Carpi and C. Pappone, "Stereotaxis niobe magnetic navigation system for endocardial catheter ablation and gastrointestinal capsule endoscopy.," *Expert Review of Medical Devices*, vol. 6, no. 5, pp. 487–498, 2009.

[94] B. L. Nguyen, J. L. Merino, and E. S. Gang, "Remote navigation for ablation procedures – a new step forward in the treatment of cardiac arrhythmias," *European Cardiology*, vol. 6, no. 3, pp. 50–56, 2010.

[95] Aeon scientific. [Online]. March, 2015. URL: http://www.aeon-scientific.com

[96] F. Ullrich, S. Schuerle, R. Pieters, A. Dishy, S. Michels, and B. J. Nelson, "Automated capsulorhexis based on a hybrid magnetic-mechanical actuation system," in *Robotics and Automation (ICRA), 2014 IEEE International Conference on*, pp. 4387–4392, IEEE, 2014.

[97] M. P. Kummer, J. J. Abbott, B. E. Kratochvil, R. Borer, A. Sengul, and B. J. Nelson, "Octomag: An electromagnetic system for 5-DOF wireless micromanipulation," *Robotics, IEEE Transactions on*, vol. 26, no. 6, pp. 1006–1017, 2010.

[98] T. Roberts, W. Hassenzahl, S. Hetts, and R. Arenson, "Remote control of catheter tip deflection: An opportunity for interventional MRI," *Magnetic Resonance in Medicine*, vol. 48, no. 6, pp. 1091–1095, 2002.

[99] F. Settecase, M. S. Sussman, M. W. Wilson, S. Hetts, R. L. Arenson, V. Malba, A. F. Bernhardt, W. Kucharczyk, and T. P. Roberts, "Magnetically-assisted remote control (MARC) steering of endovascular catheters for interventional MRI: a model for deflection and design implications," *Medical physics*, vol. 34, no. 8, pp. 3135–3142, 2007.

[100] N. Gudino, J. Heilman, J. Derakhshan, J. Sunshine, J. Duerk, and M. Griswold, "Control of intravascular catheters using an array of active steering coils," *Medical physics*, vol. 38, no. 7, pp. 4215–4224, 2011.

[101] T. Liu and M. Çavoşoglŭ, "Three dimensional modeling of an MRI actuated steerable catheter system," in *2014 IEEE International Conference on Robotics and Automation (ICRA)*, pp. 4393–4398, May 2014.

[102] T. Greigarn and M. C. Çavoşoglŭ, "Task-space motion planning of MRI-actuated catheters for catheter ablation of atrial fibrillation," in *2014 IEEE/RSJ International Conference on Intelligent Robots and Systems*, pp. 3476–3482, IEEE, 2014.

[103] J. R. Clark, L. Leon, F. M. Warren, and J. J. Abbott, "Magnetic guidance of cochlear implants: Proof-of-concept and initial feasibility study," *Journal of Medical Devices*, vol. 6, pp. 035002–035002, Aug. 2012.

[104] A. W. Mahoney and J. J. Abbott, "5-DOF manipulation of an untethered magnetic device in fluid using a single permanent magnet," in *Proceedings of Robotics : Science and Systems*, July 2014.

[105] I. Tunay, "Distributed parameter statics of magnetic catheters," in *2011 Annual International Conference of the IEEE Engineering in Medicine and Biology Society*, pp. 8344–8347, Aug. 2011.

[106] I. Tunay, "Spatial continuum models of rods undergoing large deformation and inflation," *IEEE Transactions on Robotics*, vol. 29, no. 2, pp. 297–307, 2013.

[107] A. A. Eshraghi, N. W. Yang, and T. J. Balkany, "Comparative study of cochlear damage with three perimodiolar electrode designs," *The Laryngoscope*, vol. 113, no. 3, pp. 415–419, 2003.

[108] C. A. Buchman, J. Joy, A. Hodges, F. F. Telischi, and T. J. Balkany, "Vestibular effects of cochlear implantation," *The Laryngoscope*, vol. 114, no. S103, pp. 1–22, 2004.

[109] P. S. Roland, W. Gstöttner, and O. Adunka, "Method for hearing preservation in cochlear implant surgery," *Operative Techniques in Otolaryngology-Head and Neck Surgery*, vol. 16, no. 2, pp. 93–100, 2005.

[110] P. Roland and C. Wright, "Surgical aspects of cochlear implantation: mechanisms of insertional trauma," *Advances in Otorhinolaryngology*, vol. 64, no. R, p. 11, 2006.

[111] P. Wardrop, D. Whinney, S. J. Rebscher, J. T. Roland, W. Luxford, and P. A. Leake, "A temporal bone study of insertion trauma and intracochlear position of cochlear implant electrodes. i: Comparison of nucleus banded and nucleus contour electrodes," *Hearing research*, vol. 203, no. 1, pp. 54–67, 2005.

[112] P. Wardrop, D. Whinney, S. J. Rebscher, W. Luxford, and P. Leake, "A temporal bone study of insertion trauma and intracochlear position of cochlear implant electrodes. ii: comparison of spiral clarion and hifocus ii electrodes," *Hearing research*, vol. 203, no. 1, pp. 68–79, 2005.

[113] O. F. A. H. C. Pillsbury and C. A. Buchman, "Minimizing intracochlear trauma during cochlear implantation," *Cochlear Implants and Hearing Preservation*, vol. 67, pp. 96–107, 2009.

[114] C. G. Wright, P. S. Roland, *et al.*, "Vascular trauma during cochlear implantation: A contributor to residual hearing loss?," *Otology & neurotology: official publication of the American Otological Society, American Neurotology Society [and] European Academy of Otology and Neurotology*, 2012.

[115] C. A. von Ilberg, U. Baumann, J. Kiefer, J. Tillein, and O. F. Adunka, "Electric-acoustic stimulation of the auditory system: a review of the first decade," *Audiology and Neurotology*, vol. 16, no. supplement 2, pp. 1–30, 2011.

[116] O. Adunka, H. Pillsbury, and C. Buchman, "Minimizing intracochlear trauma during cochlear implantation," *Advances in Otorhinolaryngoly*, vol. 67, pp. 96–107, 2010.

[117] J. Zhang, J. T. Roland, S. Manolidis, and N. Simaan, "Optimal path planning for robotic insertion of steerable electrode arrays in cochlear implant surgery," *Journal of medical devices*, vol. 3, no. 1, 2009.

[118] X. Meshik, T. A. Holden, R. A. Chole, and T. E. Hullar, "Optimal cochlear implant insertion vectors," *Otology & neurotology: official publication of the American Otological Society, American Neurotology Society [and] European Academy of Otology and Neurotology*, vol. 31, no. 1, p. 58, 2010.

[119] M. Cosetti and J. T. Roland Jr, "Cochlear implant electrode insertion," *Operative Techniques in Otolaryngology-Head and Neck Surgery*, vol. 21, no. 4, pp. 223–232, 2010.

[120] A. Hussong, T. S. Rau, T. Ortmaier, B. Heimann, T. Lenarz, and O. Majdani, "An automated insertion tool for cochlear implants: another step towards atraumatic cochlear implant surgery," *International journal of computer assisted radiology and surgery*, vol. 5, no. 2, pp. 163–171, 2010.

[121] T. Rau, A. Hussong, M. Leinung, T. Lenarz, and O. Majdani, "Automated insertion of preformed cochlear implant electrodes: evaluation of curling behaviour and insertion forces on an artificial cochlear model," *International Journal of Computer Assisted Radiology and Surgery*, vol. 5, no. 2, pp. 173–181, 2010.

[122] J. Zhang, W. Wei, J. Ding, J. T. Roland Jr, S. Manolidis, and N. Simaan, "Inroads toward robot-assisted cochlear implant surgery using steerable electrode arrays," *Otology & Neurotology*, vol. 31, no. 8, pp. 1199–1206, 2010.

[123] J. Pile, M. Y. Cheung, J. Zhang, and N. Simaan, "Algorithms and design considerations for robot assisted insertion of perimodiolar electrode arrays," in *Robotics and Automation (ICRA), 2011 IEEE International Conference on*, pp. 2898–2904, IEEE, 2011.

[124] J. Pile and N. Simaan, "Modeling, design, and evaluation of a parallel robot for cochlear implant surgery (in press)," *IEEE Transactions on Mechatronics*.

[125] B. Arcand, P. Bhatti, N. Butala, J. Wang, C. Friedrich, and K. Wise, "Active positioning device for a perimodiolar cochlear electrode array," *Microsystem technologies*, vol. 10, no. 6-7, pp. 478–483, 2004.

[126] B. Chen, H. Kha, and G. Clark, "Development of a steerable cochlear implant electrode array," in *3rd Kuala Lumpur International Conference on Biomedical Engineering 2006*, pp. 607–610, Springer, 2007.

[127] J. Wu, L. Yan, H. Xu, W. C. Tang, and F.-G. Zeng, "A curvature-controlled 3d micro-electrode array for cochlear implants," in *Solid-State Sensors, Actuators and Microsystems, 2005. Digest of*

Technical Papers. TRANSDUCERS'05. The 13th International Conference on, vol. 2, pp. 1636–1639, IEEE, 2005.

[128] F. Zeng, S. Rebscher, W. Harrison, X. Sun, and H. Feng, "Cochlear implants: System design, integration, and evaluation," *IEEE Reviews in Biomedical Engineering*, vol. 1, pp. 115–142, 2008.

[129] E. Erixon, H. Högstorp, K. Wadin, and H. Rask-Andersen, "Variational anatomy of the human cochlea: implications for cochlear implantation," *Otology & Neurotology*, vol. 30, no. 1, pp. 14–22, 2009.

[130] J. H. Noble, R. B. Rutherford, R. F. Labadie, O. Majdani, and B. M. Dawant, "Modeling and segmentation of intra-cochlear anatomy in conventional ct," in *SPIE Medical Imaging*, pp. 762302–762302, International Society for Optics and Photonics, 2010.

[131] R. Martinez-Monedero, J. K. Niparko, and N. Aygun, "Cochlear coiling pattern and orientation differences in cochlear implant candidates," *Otology & Neurotology*, vol. 32, no. 7, pp. 1086–1093, 2011.

[132] E. Avci, T. Nauwelaers, T. Lenarz, V. Hamacher, and A. Kral, "Variations in microanatomy of the human cochlea," *Journal of Comparative Neurology*, vol. 522, no. 14, pp. 3245–3261, 2014.

[133] K. S. van der Marel, J. J. Briaire, R. Wolterbeek, J. Snel-Bongers, B. M. Verbist, and J. H. Frijns, "Diversity in cochlear morphology and its influence on cochlear implant electrode position," *Ear and hearing*, vol. 35, no. 1, pp. e9–e20, 2014.

[134] D. Attali, J.-D. Boissonnat, and H. Edelsbrunner, "Stability and computation of medial axes-a state-of-the-art report," in *Mathematical foundations of scientific visualization, computer graphics, and massive data exploration*, pp. 109–125, Springer, 2009.

[135] M. Negahdar, A. Ahmadian, N. Navab, and K. Firouznia, "Path planning for virtual bronchoscopy," in *Engineering in Medicine and Biology Society, 2006. EMBS'06. 28th Annual International Conference of the IEEE*, pp. 156–159, IEEE, 2006.

[136] D. S. Paik, C. F. Beaulieu, R. B. Jeffrey, G. D. Rubin, and S. Napel, "Automated flight path planning for virtual endoscopy," *Medical Physics*, vol. 25, p. 629, 1998.

[137] B. M. Verbist, L. Ferrarini, J. J. Briaire, A. Zarowski, F. Admiraal-Behloul, H. Olofsen, J. H. Reiber, and J. H. Frijns, "Anatomic considerations of cochlear morphology and its implications for insertion trauma in cochlear implant surgery," *Otology & Neurotology*, vol. 30, no. 4, pp. 471–477, 2009.

[138] C. H. Reinsch, "Smoothing by spline functions," *Numerische mathematik*, vol. 10, no. 3, pp. 177–183, 1967.

[139] J. Zhang and N. Simaan, "Design of underactuated steerable electrode arrays for optimal insertions," *Journal of Mechanisms and Robotics*, vol. 5(1), p. 011008, January 2013.

[140] D. C. Jiles, *Introduction to Magnetism and Magnetic Materials*. CRC Press, 1998.

[141] A. Petruska and J. Abbott, "Optimal permanent-magnet geometries for dipole field approximation," *Magnetics, IEEE Transactions on*, vol. 49, no. 2, pp. 811–819, 2013.

[142] N. Derby and S. Olbert, "Cylindrical magnets and ideal solenoids," *American Journal of Physics*, vol. 78, no. 3, pp. 229–235, 2010.

[143] E. P. Furlani, *Permanent Magnet and Electromechanical Devices: Materials, Analysis, and Applications*. Academic Press, 2001.

[144] H. E. Knoepfel, *Magnetic Fields: a Comprehensive Theoretical Treatise for Practical Use*. John Wiley & Sons, 2008.

[145] G. Kirchhoff, "Über das gleichgewicht und die bewegung eines unendlich dünnen elastischen stabes.," *Journal für die reine und angewandte Mathematik*, vol. 56, pp. 285–313, 1859.

[146] G. Kirchhoff, *Vorlesungen uber Mathematische Physik. Mechanik*, vol. 28. Druck und verlag von BG Teubner, 1876.

[147] E. H. Dill, "Kirchhoff's theory of rods," *Archive for History of Exact Sciences*, vol. 44, no. 1, pp. 1–23, 1992.

[148] S. S. Antman, *Nonlinear Problems of Elasticity*. Springer New York, 2 ed., 2005.

[149] B. Audoly and Y. Pomeau, *Elasticity and geometry: From Hair Curls to the Nonlinear Response of Shells*. Oxford Univ. Press, 2010.

[150] D. C. Rucker, B. A. Jones, and Robert J Webster III, "A geometrically exact model for externally loaded concentric-tube continuum robots," *IEEE Transactions on Robotics*, vol. 26, pp. 769–780, Oct. 2010.

[151] B. O'neill, *Elementary differential geometry*. Academic press, 2006.

[152] A. J. Hanson, *Visualizing Quaternions*. Morgan Kaufmann Series in Interactive 3D Technology, Morgan Kaufmann/Elsevier, 1 ed., 2005.

[153] W. Wang, B. Jüttler, D. Zheng, and Y. Liu, "Computation of rotation minimizing frames," *ACM Transactions on Graphics (TOG)*, vol. 27, no. 1, p. 2, 2008.

[154] E. H. Dill, "The shear center and kirchhoff's theory of rods," tech. rep., Rutgers University, Center for Computational Modeling of Aircraft Structures, December 1993.

[155] J. Kierzenka and L. F. Shampine, "A BVP solver that controls residual and error," *Journal of Numerical Analysis, Industrial and Applied Mathematics*, vol. 3, pp. 27–41, 2008.

[156] U. M. Ascher, R. M. Mattheij, and R. D. Russell, *Numerical solution of boundary value problems for ordinary differential equations*. Series in Computational Mathematics, Prentice-Hall, 1988.

[157] A. Ben-Israel and T. N. Greville, *Generalized Inverses*, vol. 13. Springer, 2003.

[158] T. F. Chan and R. V. Dubey, "A weighted least-norm solution based scheme for avoiding joint limits for redundant joint manipulators," *Robotics and Automation, IEEE Transactions on*, vol. 11, no. 2, pp. 286–292, 1995.

[159] J. Park, Y. Choi, W. K. Chung, and Y. Youm, "Multiple tasks kinematics using weighted pseudo-inverse for kinematically redundant manipulators," in *International Conference on Robotics and Automation*, pp. 4041–4047, 2001.

[160] J. Xiang, C. Zhong, and W. Wei, "A varied weights method for the kinematic control of redundant manipulators with multiple constraints," *Robotics, IEEE Transactions on*, vol. 28, no. 2, pp. 330–340, 2012.

[161] O. Khatib, "Real-time obstacle avoidance for manipulators and mobile robots," *The international journal of robotics research*, vol. 5, no. 1, pp. 90–98, 1986.

[162] D. E. Whitney, "Resolved motion rate control of manipulators and human prostheses.," *IEEE Transactions on man-machine systems*, 1969.

[163] P. Chiacchio, S. Chiaverini, L. Sciavicco, and B. Siciliano, "Closed-loop inverse kinematics schemes for constrained redundant manipulators with task space augmentation and task priority strategy," *The International Journal of Robotics Research*, vol. 10, no. 4, pp. 410–425, 1991.

[164] G. Bradski, "OpenCV," *Dr. Dobb's Journal of Software Tools*, 2000.

[165] R. I. Hartley and P. Sturm, "Triangulation," *Computer vision and image understanding*, vol. 68, no. 2, pp. 146–157, 1997.

[166] H. S. M. Coxeter, *Introduction to Geometry*. New York, London, 1961.

[167] M. J. Troughton, *Handbook of plastics joining: a practical guide*. William Andrew, 2008.

[168] R. J. Wise, *Thermal welding of polymers*. Woodhead Publishing, 1999.

[169] D. Stavrov and H. Bersee, "Resistance welding of thermoplastic composites-an overview," *Composites Part A: Applied Science and Manufacturing*, vol. 36, no. 1, pp. 39–54, 2005.

[170] C. M. Shakarji, "Least-squares fitting algorithms of the NIST algorithm testing system," *Journal of Research–National Institute of Standards and Technology*, vol. 103, pp. 633–641, 1998.

[171] J. D. Jackson, *Classical Electrodynamics*, vol. 3. Wiley New York etc., 1962.